2015-07-01

Development of a Simplified Performance-Based Procedure for Assessment of Liquefaction Triggering Using Liquefaction Loading Maps

Kristin Jane Ulmer
Brigham Young University - Provo

BYU ScholarsArchive Citation

Ulmer, Kristin Jane, "Development of a Simplified Performance-Based Procedure for Assessment of Liquefaction Triggering Using Liquefaction Loading Maps" (2015). *All Theses and Dissertations*. 5600.
https://scholarsarchive.byu.edu/etd/5600

Development of a Simplified Performance-Based Procedure for Assessment of Liquefaction Triggering Using Liquefaction Loading Maps

Kristin Jane Ulmer

A thesis submitted to the faculty of
Brigham Young University
in partial fulfillment of the requirements for the degree of

Master of Science

Kevin W. Franke, Chair
Kyle M. Rollins
W. Spencer Guthrie

Department of Civil and Environmental Engineering

Brigham Young University

July 2015

ABSTRACT

Development of a Simplified Performance-Based Procedure for Assessment of Liquefaction Triggering Using Liquefaction Loading Maps

Kristin Jane Ulmer
Department of Civil and Environmental Engineering, BYU
Master of Science

Seismically-induced liquefaction has been the cause of significant damage to infrastructure and is a serious concern in current civil engineering practice. Several methods are available for assessing the risk of liquefaction at a given site, each with its own strengths and limitations. One probabilistic method has been shown to provide more consistent estimates of liquefaction risk and can be tailored to the specific needs of a given project through hazard-targeted (i.e. based on return periods or likelihoods) results. This type of liquefaction assessment is typically called "performance-based," after the Pacific Earthquake Engineering Research (PEER) Center's performance-based earthquake engineering framework. Unfortunately, performance-based liquefaction assessment is not easily performed and can be difficult for practicing engineers to use on routine projects.

Previous research has shown that performance-based methods of liquefaction assessment can be simplified into an approximation procedure. This simplification has successfully been completed for the Cetin et al. (2004) empirical, probabilistic standard penetration test -based liquefaction triggering model. Until now, such a simplification has not been performed for another popular liquefaction triggering model developed by Boulanger and Idriss (2012). As some engineers either wish to use or are required to use the Boulanger and Idriss (2012) model in their liquefaction assessments, there is a need for a simplified performance-based method based on this model to supplement that based on the Cetin et al. (2004) model.

This thesis provides the derivation of a simplified performance-based procedure for the assessment of liquefaction triggering using the Boulanger and Idriss (2012) model. A validation study is performed in which 10 cities across the United States are analyzed using both the simplified procedure and the full performance-based procedure. A comparison of the results from these two analyses shows that the simplified procedure provides a reasonable approximation of the full performance-based procedure. This thesis also describes the development of liquefaction loading maps for six states and a spreadsheet that performs the necessary correction calculations for the simplified method.

Keywords: liquefaction, performance-based earthquake engineering, PBEE, probabilistic, standard penetration test, SPT, probability of liquefaction, map-based procedures

ACKNOWLEDGEMENTS

First, I thank my advisory committee for their tutoring and guidance throughout my graduate school journey. They have taught me well, both in and out of the classroom. I especially thank my advisor, Dr. Franke, for his counsel, direction, encouragement, and example throughout the research process. I will always be grateful for his mentoring during this challenging time.

The other graduate students who worked with me in the same little office connected to the soils laboratory provided much needed laughter, help, and perspective. Thank you, Levi Ekstrom, Brian Peterson, Lucy Astorga, and Jasmyn Harper. Special thanks are also due to Levi for his help in preparing reports, presentations, and journal papers. Thank you, Brian, for all your help with *PBLiquefY*. I also must thank Braden Error, who provided significant help with map-making, as well as Alex Arndt, Adam Rose, and Ethan Condiff.

Funding for this research was provided by a Federal Highway Administration Pooled Fund Study (Award No. TPF-5(296), with participation from Utah, Alaska, Connecticut, Idaho, Montana, and South Carolina State Departments of Transportation). I gratefully acknowledge this support. The conclusions and opinions expressed in this paper do not necessarily reflect those of the sponsors.

Finally, I thank my amazing husband, Austin. He was the one who always believed in me and convinced me that I could be a successful graduate student. Even while working on his own graduate research, he supported me on countless difficult days and even stayed up on a few late nights to help "babysit" computers with me. Thank you, Austin. We did it!

TABLE OF CONTENTS

LIST OF TABLES

LIST OF FIGURES

1. INTRODUCTION

Soil liquefaction is a significant concern in earthquake engineering. This seismic hazard can cause major damage to engineered structures and foundations, leading to loss of life and property as well as substantial recovery costs. Though the effects of soil liquefaction have been observed for many years, the scientific process of understanding soil liquefaction truly began with the Alaska (mean magnitude, $M_w = 9.2$) and Niigata ($M_w = 7.5$) earthquakes of 1964. Since that time, researchers have developed several techniques to determine causes, predict likelihoods, and mitigate hazards associated with liquefaction. In particular, probabilistic or performance-based methods of liquefaction assessment have gained popularity in recent years. These methods have been shown to provide many benefits over conventional methods of liquefaction assessment. However, performance-based methods are complex and require considerable training to properly perform the associated calculations. This complexity has caused practicing engineers to avoid using performance-based methods on routine projects, despite the proven benefits of these methods. In response to this problem, some researchers have developed simplified performance-based procedures for the Cetin et al. (2004) liquefaction triggering model, but none have yet developed a simplified procedure using the Boulanger and Idriss (2012) model.

The purpose of this thesis is to derive a simplified performance-based procedure based on the Boulanger and Idriss (2012) model for the assessment of liquefaction triggering potential. This simplified approach is intended to provide the benefits of performance-based methods in a userfriendly, streamlined manner that can be easily performed on routine projects. The key component of this simplified procedure is the development of contoured parameter maps, which are made using full performance-based calculations of reference parameters.

Though the simplified method presented in this thesis may seem simple from a user's standpoint, the method is far from being simplistic. Sophisticated performance-based computations are built into the development of the parameter maps and maintain the intended performance-based nature of this approach. Once the maps have been created, the hard work of a performance-based approach is essentially complete. Engineers would only need site-specific soil information (which they likely already have on hand) and the correction equations provided in this thesis. This new procedure allows engineers to easily compare simplified performance-based estimates of liquefaction triggering potential between the Boulanger and Idriss (2012) and Cetin et al. (2004) models, which to this point has not been possible. Such a comparison is outside the scope of this thesis, but would be beneficial for engineers making critical decisions in liquefaction mitigation projects.

This thesis outlines the derivation of the simplified procedure as well as describes the process for developing the parameter maps. Several sites across the United States are analyzed to validate the simplified procedure. A detailed outline of the simplified procedure is provided and explains how deterministic analyses may be used in conjunction with the simplified procedure.

2. LIQUEFACTION FUNDAMENTALS

Though the term liquefaction has been used to describe a wide variety of phenomena, the common characteristic of all these phenomena is the development of excess pore water pressure under undrained loading conditions (Kramer, 1996). During undrained loading, the tendency of a saturated soil to contract causes positive excess pore pressures to develop, which causes a decrease in effective stress. This decrease in effective stress can lead to several types of failures and deformations. These effects can generally be categorized into one of two types: flow liquefaction and cyclic mobility. Cyclic mobility occurs more frequently and typically causes less damage than flow liquefaction, but it can occur in many more soil types and site conditions. For the remainder of this paper, the term *liquefaction* is used to describe both flow liquefaction and cyclic mobility. The more precise terms of flow liquefaction and cyclic mobility are used when necessary.

Flow liquefaction is typically characterized by significant, sudden deformations affecting large areas (Kramer, 1996). This type of liquefaction develops when the static shear stress of a soil mass exceeds the liquefied soil's shear strength. This unstable state can lead to a sudden movement of the soil mass, which is called flow failure. Flow failures can develop statically, though cyclic stresses can decrease the soil's shear strength and lead to the unstable condition associated with flow failures.

Cyclic mobility, unlike flow liquefaction, occurs when static shear stress is less than a soil's shear strength (Kramer, 1996). Cyclic mobility failures produce incremental deformations as earthquake shaking drives lateral spread displacements and level-ground liquefaction. Lateral spread displacements involve a lurching movement of a surficial layer that deforms the soil layer in the lateral direction. This type of failure may occur on very gently sloping ground or on flat ground near bodies of water. Level-ground liquefaction develops as excess pore pressures in the soil cause water to flow upward through the soil profile. This upward seepage can lead to vertical settlements and sand boils.

To assess hazards associated with liquefaction, three topics must be addressed: susceptibility, initiation, and effects. A particular soil may not be susceptible to liquefaction to begin with. Even if a soil is susceptible, conditions may not be sufficient to initiate liquefaction in the soil. Finally, though liquefaction may initiate in a soil, damaging effects may not manifest themselves. Thus, a complete evaluation of liquefaction hazard requires the consideration of each of these topics.

2.1 **Liquefaction Susceptibility**

The question of whether a soil is susceptible to liquefaction is the first step to assessing liquefaction hazards. If the soil is not susceptible to liquefaction, there is no need to consider initiation or potential effects. Susceptibility of a soil to liquefaction can be determined using several different sets of criteria, including historical, geologic, compositional, and state criteria.

2.1.1 Historic, Geologic, and Compositional Criteria

Historical criteria is a simple consideration of whether or not the soil has liquefied in the past. This consideration is usually based on case histories and physical evidence of previous liquefaction phenomena. Youd (1984) discovered that liquefaction often recurs at the same location as long as soil and groundwater conditions remain generally unchanged. Ambraseys

(1988) found a correlation between moment magnitude and the epicentral distance from the earthquake to the farthest observed liquefaction event. With increasing moment magnitude, distance to the farthest observed liquefaction event increased. This relationship provides an initial estimate of regional liquefaction hazard scenarios.

Geologic criteria considers geologic setting in the assessment of a soil's susceptibility to liquefaction. Youd and House (1977) found that "shallow, saturated, Holocene fluvial, deltaic and aeolian deposits and poorly compacted artificial sand fills have highest susceptibilities to liquefaction and ground failure" according to the liquefaction case histories available at the time. They also found that Holocene deposits were somewhat susceptible, though to a lesser degree than other deposits previously listed. Pleistocene sand deposits in general were found to be even less susceptible. Glacial till, clay-rich and pre-Pleistocene deposits typically were not found to be susceptible to liquefaction. Traditionally, liquefaction was considered possible only in saturated soils (Kramer 1996), and therefore groundwater conditions also governed whether a soil layer may be susceptible to liquefaction. However, cyclic triaxial tests performed by Unno, Kazama et al. (2008) have shown that some unsaturated soils may lose effective stress due to cyclic shear and thereafter behave as liquids. They found this phenomenon to occur when the pore air and water pressures are equal to the initial mean total confining pressure. Other researchers have also observed liquefaction in unsaturated soils during cyclic laboratory testing (Liu and Xu, 2013; Tsukamoto et al., 2014). Therefore, unsaturated soils may not be immediately disregarded in liquefaction susceptibility assessment.

Compositional criteria for liquefaction susceptibility have changed significantly in recent years. For many years, practitioners relied on the so-called "Chinese criteria" (Wang 1979) which stated that fine-grained soils may be susceptible to liquefaction if they satisfy the following requirements:

Fraction finer than 0.005mm $\leq$ 15%

Liquid Limit, LL $\leq$ 35%

Natural Water Content, $w_c \geq 0.9$ LL

Liquidity Index ≤ 0.75

This simple set of criteria was widely used until several significant earthquake events (such as the 1994 Northridge, 1999 Kocaeli, and 1999 Chi-Chi earthquakes) caused soils to liquefy that were previously considered "safe" under the Chinese criteria. This led to several researchers reconsidering the conventional compositional criteria. Bray and Sancio (2006) performed cyclic testing on several soils found to liquefy in Adapazari during the Kocaeli earthquake and found that the Chinese criteria were not sufficient to distinguish between susceptible and non-susceptible soils. They concluded that the plasticity index (PI) is a better indicator of liquefaction susceptibility. and summarized their observations with the following statements:

1) Loose soils with PI<12 and w_c/LL > 0.85 were susceptible (where w_c is water content in percent and LL is liquid limit in percent)
2) Loose soils with 12<PI<18 and w_c/LL > 0.8 were more resistant to liquefaction
3) Soils with PI > 18 were not susceptible to liquefaction when tested at low effective confining stresses

Other researchers have also suggested compositional criteria, such as the suggestion from Idriss and Boulanger (2006) to only consider soils with fines that are of very low plasticity (PI<7) when using their liquefaction initiation model. Some researchers have observed liquefaction of gravelly soils in the field and in the laboratory. Cao et al. found during the 2008 Wenchuan Earthquake that gravelly soils did liquefy (Cao et al. 2011).

2.1.2 State Criteria

Though a soil may meet the historical, geologic, and compositional criteria, the soil is not necessarily susceptible to liquefaction because liquefaction is also dependent upon the initial state of the soil. This concept of a state criteria incorporates a soil's stress and density characteristics at the time of the earthquake into the assessment of whether or not a soil is susceptible to liquefaction. Casagrande (1936) developed early models of what the state criteria should be. He performed several drained, strain-controlled triaxial tests on initially loose and initially dense sands and found that all specimens tested at the same effective confining pressure approached the same density when sheared to large strains, despite their initial density. Loose specimens contracted to a denser state while dense specimens contracted initially and then dilated to a looser state. The void ratio to which all soils converged was then termed the *critical void ratio*, e_c, and the definition of e_c with varying confining stresses, σ'_{3c} was called the CVR line (Figure 2-1). Casagrande hypothesized that undrained testing of loose specimens would yield positive excess pore pressures and dense specimens would yield negative excess pore pressures until the specimens reached the critical void ratio. This line, he thought, would mark the boundary between susceptible and non-susceptible soils. Soils plotted above the CVR line would be considered prone to contraction (susceptible to liquefaction in undrained conditions) and soils plotted below the CVR line would be considered prone to dilation (gains strength in undrained conditions and is not susceptible to liquefaction).

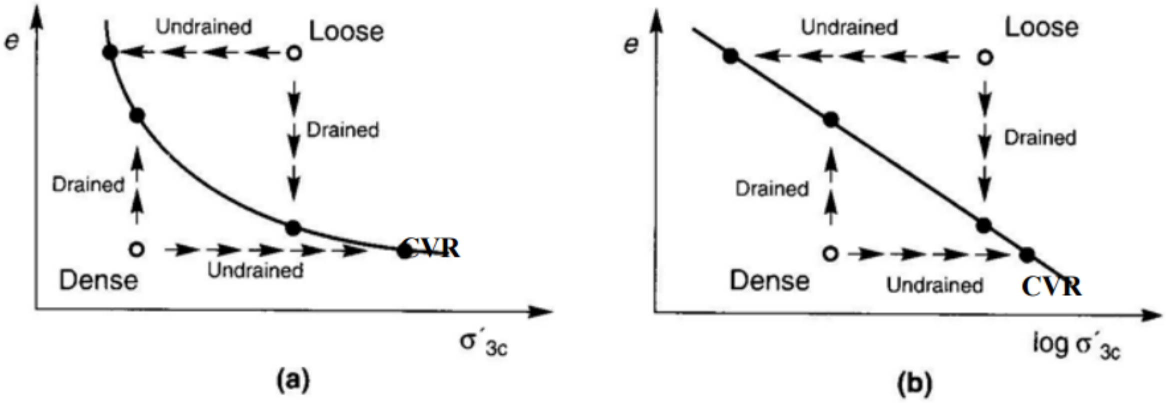

Figure 2-1: Illustration of Casagrande's CVR Line (after Kramer, 1996)

Casagrande's CVR explanation was generally considered sufficient until the failure of the Fort Peck Dam in 1938. The investigation of the failure revealed that the initial states of some liquefied soils were plotted below the CVR line. In response to this discrepancy, Casagrande's PhD student, Castro, performed several static and cyclic triaxial tests on isotropically consolidated soil specimens and went on to develop a slightly different concept of state criteria (Castro, 1969). He found that, in general, the specimens behaved in one of three ways. Very loose specimens (specimen A in Figure 2-2) would contract under monotonic loading and exhibit liquefaction. Very dense specimens (specimen B) would initially contract then dilate, gain strength, and show no signs of liquefaction. Specimens at intermediate densities (specimen C) would exceed an initial peak strength and enter a limited phase of strain-softening behavior before reaching a phase transformation where the soil dilates and gains strength. This type of behavior was termed *limited liquefaction*.

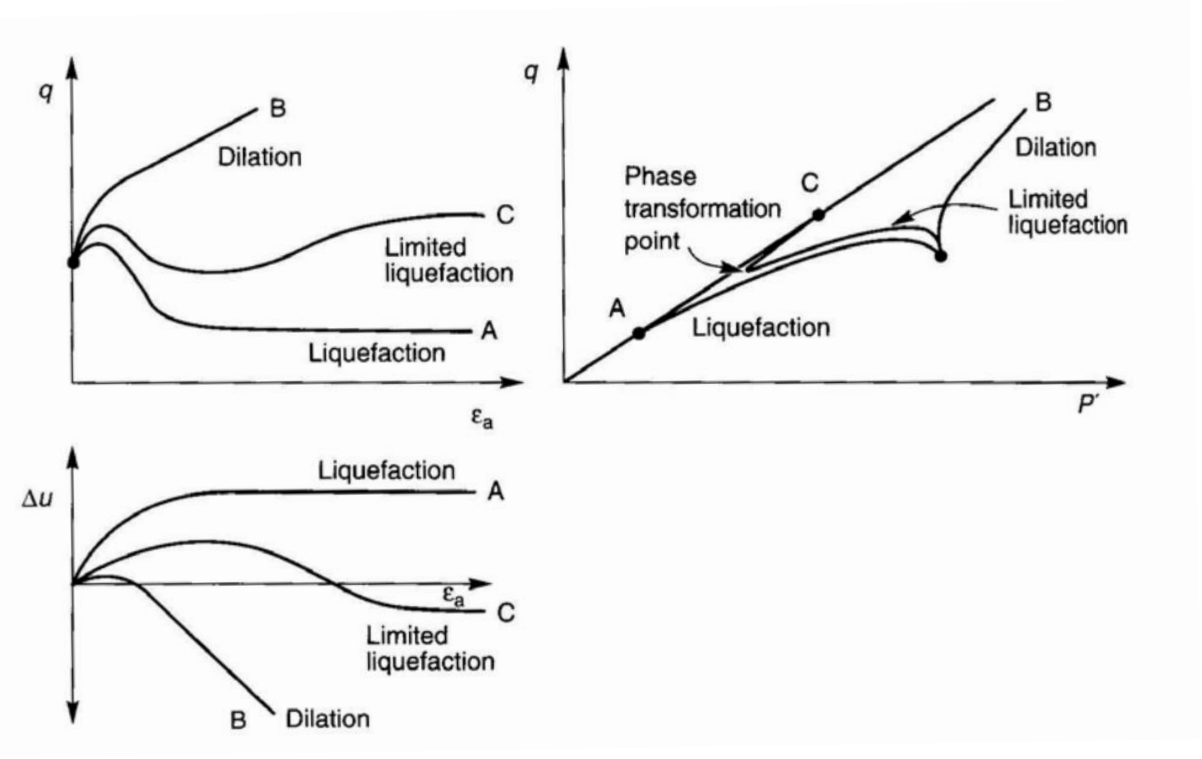

Figure 2-2: Illustration of Castro's Triaxial Tests (after Kramer, 1996)

Castro's research led to the definition of the *steady state of deformation* (Castro and Poulos, 1977; Poulos 1981), which is the state in which the soil deforms continuously under constant shear stress and effective confining pressure at constant volume and velocity. The strength of the soil in this state is called the steady state strength, S_{su}. The *steady-state line*, SSL graphically describes the relationship between void ratio and effective confining pressure in the steady state of deformation. The SSL line can be plotted in three-dimensional space (Figure 2-3) and may help in the evaluation of liquefaction susceptibility of a given soil. If the soil's initial state plots below the SSL in $e - \sigma$ space, then the soil is not susceptible to flow liquefaction. If the soil's initial state plots above the SSL, then the soil will liquefy only if the static shear stress exceeds S_{su}. Graphically, the SSL line plots below and approximately parallel to Casagrande's CVR line in e -

$\log(\sigma')$ space. The magnitude of the difference between the CVR and the SSL lines may depend on the soil's collapse potential (Alarcon-Guzman et al. 1988).

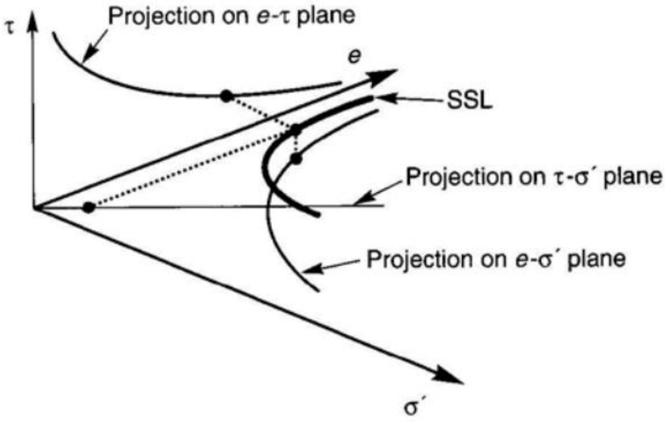

Figure 2-3: Steady-State Line (after Kramer, 1996)

Though the SSL concept generally described soil behavior, there was no singular parameter to describe soil behavior in undrained conditions. A soil with a given void ratio could be susceptible to liquefaction under high confining pressure but non-susceptible under low confining pressure. Been and Jeffries (1985) developed a single parameter measure of sand behavior called the *state parameter*. Their reasoning was that soils with the same distance vertically from the SSL would behave similarly. Thus, this state parameter is defined as

$$\psi = e - e_{ss} \tag{2-1}$$

where e_{ss} is the void ratio of the SSL at the effective confining pressure of interest. When ψ is positive, the soil behaves in a contractive manner. When ψ is negative, the soil behaves in a dilative manner and is not susceptible to flow liquefaction.

2.2 **Liquefaction Initiation**

Though a given soil is deemed "susceptible" to liquefaction, liquefaction will only occur under certain conditions. Liquefaction initiation will be discussed here in two categories: flow liquefaction and cyclic mobility. Cyclic mobility is an earthquake phenomenon while flow liquefaction may be initiated in many different ways, such as monotonic loading (e.g. man-made fills, mine tailings piles) and non-seismic vibration (e.g. pile driving, train traffic, blasting).

2.2.1 Flow Liquefaction

Hanzawa et al. (1979) showed that liquefaction initiation could be described using stress paths of loose, saturated sands. As shown in Figure 2-4, five specimens isotropically consolidated to the same void ratio will behave differently in undrained conditions under different initial confining pressures. Specimens A and B plot below the SSL and therefore exhibit dilative behaviors as their stress paths approach the steady state point. No liquefaction occurs in these specimens. Specimens C, D, and E plot above the SSL and therefore exhibit contractive behaviors. In an undrained loading scenario, the excess pore pressures in these specimens increase, thereby decreasing the effective stress on the specimens. This leads to the stress paths moving backwards toward the steady state point. Before reaching the steady state point, these specimens experience a peak shear strength (marked with an × on the stress paths) before rapidly losing shear strength on the approach to the steady state point. It is at the point of the peak shear strength that flow liquefaction is initiated in these samples. Vaid and Chern (1985) first proposed to draw a line through these peak strengths to develop a *flow liquefaction surface* (FLS), though the surface was called by a different name at the time. Note that the FLS truncates at the q corresponding with the steady state point because flow liquefaction cannot occur if the stress path is below the steady state point. This FLS delineates a region in *p'*-*q* space in which flow liquefaction would occur during undrained shear (see Figure 2-5). If a soil exists in this region and experiences an undrained disturbance that pushes it toward its steady state strength, then flow liquefaction will initiate.

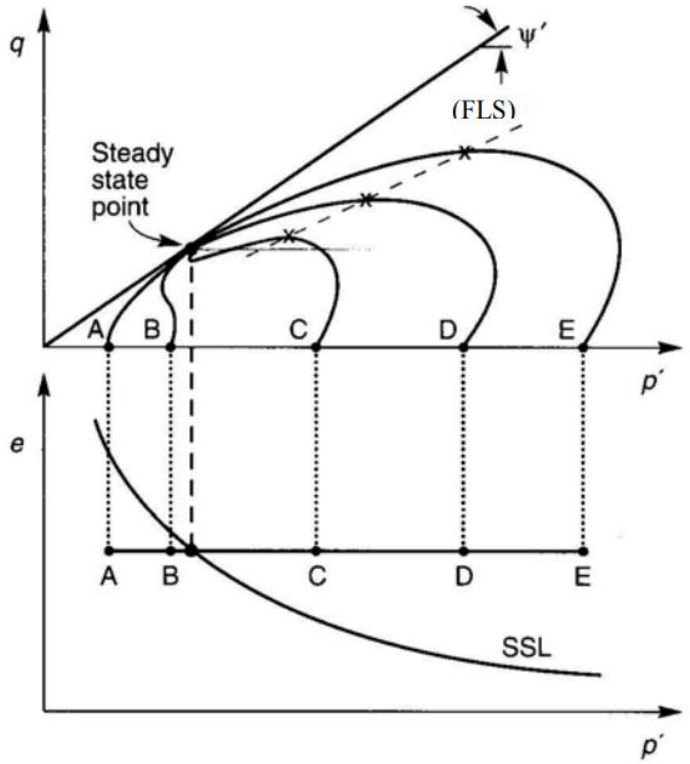

Figure 2-4: Flow Liquefaction Surface (after Kramer 1996)

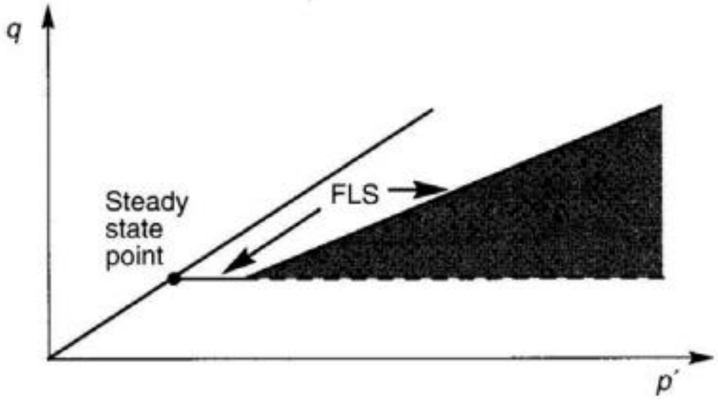

Figure 2-5: Region (in *p'* – *q* Space) Susceptible to Flow Liquefaction (Shown as Shaded, after Kramer 1996)

To evaluate whether or not a soil will reach the FLS, the soil's steady state strength must first be estimated. A soil's steady state strength can be estimated in several ways, including laboratory techniques (Poulos et al., 1985), in situ techniques (Seed and Harder, 1990), and normalized strength techniques (Olson and Stark, 2002; Idriss and Boulanger, 2007). For example, Seed and Harder (1990) developed a correlation with clean-sand equivalent Standard Penetration Test (SPT) blowcount ($N_{1,60-cs}$) to estimate steady-state (or residual) strengths of liquefied soils. This correlation is presented graphically in Figure 2-6. $N_{1,60-cs}$ was defined by Seed and Harder (1990) as

$$N_{1,60-cs} = \alpha + N_{1,60} \tag{2-2}$$

where α is given in Table 2-1and $N_{1,60}$ is the SPT blow count corrected to 1 atmosphere of pressure and 60% hammer efficiency.

Table 2-1: Correction Factors for Computing Clean Sand Corrected SPT Blowcount for Correlation with Residual Shear Strength of Liquefied Soil (after Seed and Harder, 1990)

Fines Content, FC	α
FC ≥ 75%	5
75% > FC ≥ 50%	4
50% > FC ≥ 35%	3
35% > FC ≥ 25%	2
25% > FC ≥ 10%	1
FC < 10%	0

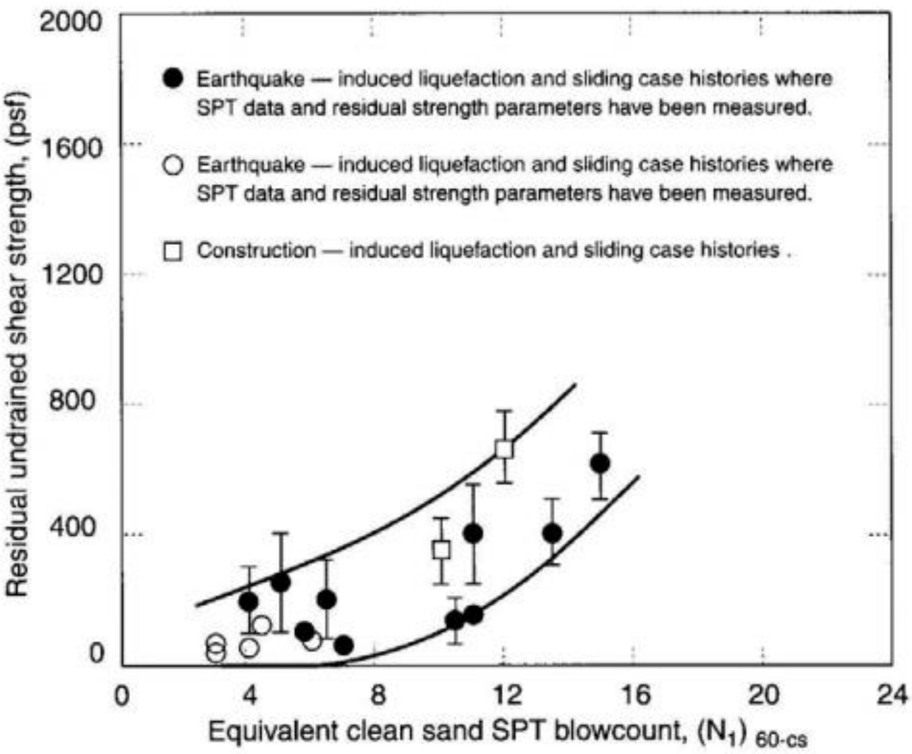

Figure 2-6: Correlation between Residual Shear Strength and Clean-Sand Equivalent SPT Resistance (after Seed and Harder, 1990)

2.2.2 Cyclic Mobility

Cyclic mobility is the gradual loss of strength in a soil due to incremental buildup of pore water pressures induced by cyclic loading under undrained conditions. This phenomenon occurs when the static shear stress is less than the steady state strength of a soil. Cyclic mobility can occur in a wide range of soils from very loose to very dense. The region susceptible to cyclic mobility is shaded in Figure 2-7.

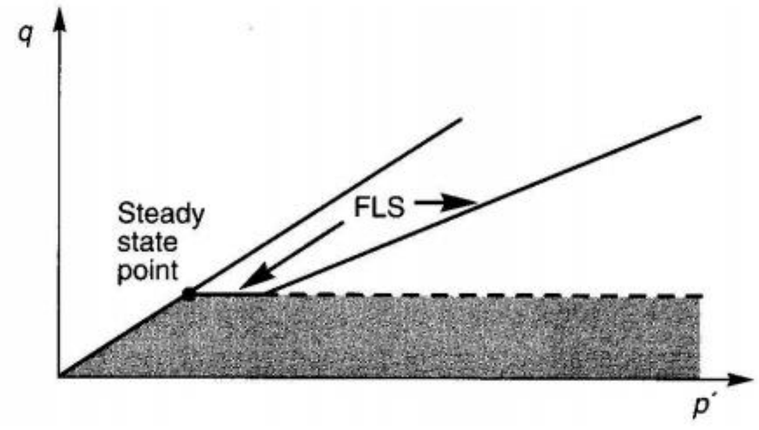

Figure 2-7: Region (in p'-q space) Susceptible to Cyclic Mobility (Shown as Shaded; after Kramer 1996)

Generally, cyclic mobility may initiate through one of three combinations of initial confining pressures and cyclic loading conditions (Kramer, 1996). The first is illustrated in Figure 2-8(a). In this case, the sum of the cyclic shear stress, τ_{cyc} and the initial static shear stress, τ_{static} does not exceed the steady state strength. In this case, the soil's stiffness and strength slowly decrease until the stress path reaches the failure envelope. The second case (b) occurs when the sum of τ_{cyc} and τ_{static} remains positive and greater than the steady state strength. Here, the soil experiences limited instances of flow liquefaction each time the stress path reaches the FLS. During these instances, large strains occur and may lead to larger strains than in the first case (a). In the third case (c), the sum of τ_{cyc} and τ_{static} is less than the steady state strength and $\tau_{static} - \tau_{cyc} < 0$. In this case, the specimen experiences both compressional and extensional forces and moves quickly to the left. Eventually, the stress path oscillates between the compression and extension portions of the drained failure envelope.

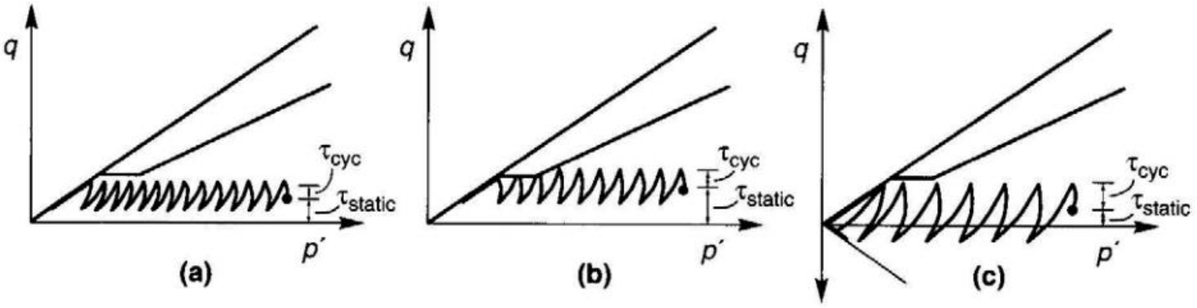

Figure 2-8: Three General Scenarios of Cyclic Mobility (after Kramer, 1996)

2.2.3 Evaluation of Initiation of Liquefaction

After establishing that a soil meets the criteria for liquefaction susceptibility and the conditions are such that liquefaction initiation may occur, practicing engineers must somehow evaluate and quantify a site's liquefaction vulnerability. This is no easy task, and can be performed using a variety of techniques. Because this topic is a key feature of this thesis, it will be discussed in greater detail in a later chapter.

2.3 **Liquefaction Effects**

If an evaluation of liquefaction susceptibility and initiation reveals that a soil is likely to liquefy, then the potential effects of liquefaction should be investigated. Many liquefaction effects have been shown to cause severe damage to infrastructure. The effects outlined here describe some of the more significant effects of liquefaction.

2.3.1 Settlement

Sands tend to densify from rearrangement of soil particles when subjected to earthquake shaking, which manifests at the ground surface as liquefaction-induced settlement. Liquefaction-induced settlement can cause damage to infrastructure in many ways. Utilities buried at shallows depths may become nonfunctional after soils settle around or underneath them. Differential settlement of buildings may cause cracking and distortion that render the building uninhabitable, as was the case for the building depicted in Figure 2-9 after the Christchurch, 2011 earthquake (M_w = 6.2).

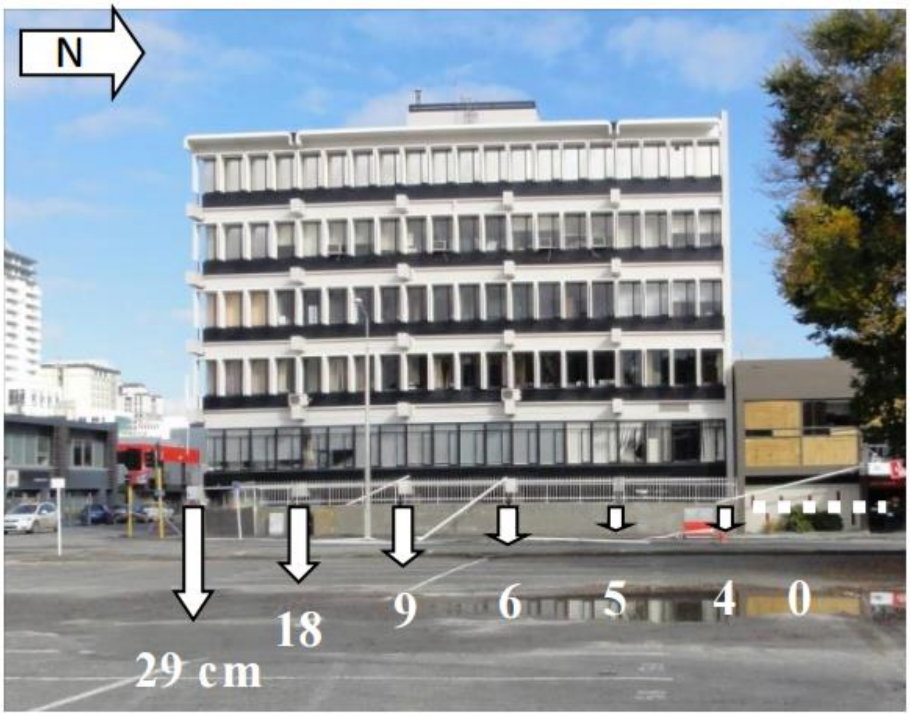

Figure 2-9: Building with Significant Liquefaction-Induced Differential Settlement after the Christchurch, 2011 Event (after GEER, 2011)

Settlement from dry sands and settlement from saturated sands are each evaluated differently. Densification of dry sands is typically dependent on initial density, the amplitude of the cyclic shear strain induced in the sand, and the number of cycles of shear strain applied during the earthquake (Kramer, 1996). Settlement of saturated sands is dependent on initial density, the maximum shear strain induced in the sand, and the excess pore pressure generated during the earthquake. Several researchers have contributed to improved methods of assessing liquefaction-induced settlement (Tokimatsu and Seed, 1987; Ishihara and Yoshimine, 1992; Stewart and Whang, 2003; Cetin et al. 2009).

2.3.2 Lateral Spread

Lateral spread is often caused by lateral movement of liquefied soil overlain with a non-liquefied crust. This crust is incrementally broken up into segments and displaced. Typically, these segments are moved toward the toe of the slope or toward the free face. Often this free face is adjacent to a body of water such as a river, lake, or ocean. Fissures and scarps may appear at the head of the lateral spread while compressed or buckled soil may be seen at the toe. Infrastructure that may be particularly susceptible to damage caused by lateral spread include bridges, railroad tracks, ports, unreinforced pavements, and poorly reinforced building foundations. Figure 2-10 shows an example of lateral spreading along the Avon River after the Christchurch, 2011 earthquake event and Figure 2-11 shows lateral displacement near the end of the Molo Pier after the Iquique (Chile), 2014 earthquake.

Several empirical models have been developed from case history databases to estimate lateral spread displacement (Bardet et al., 1999; Youd et al., 2002; Baska, 2002). These empirical models take a deterministic, single scenario (i.e. one combination of magnitude, M and distance, R) approach to estimating lateral spread displacements and incorporate soil parameters and site geometry. Semi-empirical (Faris 2004), performance-based (Franke and Kramer 2014), and simplified performance-based (Ekstrom and Franke, 2015) methods have also been developed.

Figure 2-10: Example of Lateral Spreading along the Avon River after the Christchurch, 2011 Event (after GEER, 2011)

Figure 2-11: Lateral Displacement Near the End of the Molo Pier after the Iquique (Chile), 2014 Earthquake (after GEER, 2014)

2.3.3 Flow Failure

As previously discussed, flow failures occur when the steady-state strength of the soil is less than the initial static shear stress imposed on the soil and some additional force drives the stress path of the soil to the FLS, thus triggering liquefaction. Because the soil's strength quickly declines after the FLS is reached, flow liquefaction can produce sudden, large mass movements that can cause catastrophic damage. For example, the Lower San Fernando Dam experienced flow liquefaction during the M6.7 San Fernando Earthquake in 1971. Figure 2-12 shows an image of the dam after the soil liquefied. Approximately 800,000 cubic yards of embankment slid into the reservoir and nearly caused the height of the embankment to sink below the water level of the reservoir (NOAA). If the dam had failed, the reservoir would have rushed into the densely populated valley below, endangering more than 80,000 people.

Figure 2-12: Flow Liquefaction of the Lower San Fernando Dam, 1971 (courtesy of NOAA/NGDC, E.V. Leyendecker, U.S. Geological Survey)

2.3.4 Loss of Bearing Capacity

A loss of bearing capacity occurs if the steady state strength of the liquefied soil is much less than the initial strength of the soil. This failure can cause building foundations to rotate or punch through the soil. For example, Figure 2-13 shows residential structures that were situated on liquefied soil in the 1964 Niigata earthquake in Japan. A loss of bearing capacity can also negatively affect buried structures such as gasoline storage tanks, sewer or stormwater pipes, and other significant lifelines. These buried structures may float to the ground surface because they are more buoyant than the liquefied soil surrounding them.

Figure 2-13: Bearing Capacity Failure from Soil Liquefaction During the Niigata, Japan (1964) Earthquake (courtesy of NOAA/NGDC – National Geophysical Data Center)

2.3.5 Other Effects

Other effects of soil liquefaction include increased lateral earth pressures on retaining walls, sand boils, and alteration of ground motions.

Increased lateral earth pressures on retaining walls develop as increased pore pressures in the liquefied soil lead to greater hydrostatic forces on the wall. This additional applied force can cause walls to rotate or collapse. If the soil at the toe of a retaining wall liquefies, then the wall may slide or overturn because of decreased support from passive forces in the soil.

Sand boils appear where excess pore pressures in liquefied soils find a weak seam or path of least resistance to the ground surface. To relieve the pressure, water rapidly moves to the ground surface and, in the process, carries sand particles to the ground surface. The pile of sand that accumulates is what is typically called a sand boil. An example of a sand boil is provided in Figure 2-14.

Ground motions are altered when liquefaction occurs because liquefied soil tends to be less stiff. Materials that are less stiff tend to filter out the high frequency ground motions, allowing only the low frequency motions to reach the ground surface. These low frequency motions can cause large deformations and major damage to structures with low natural frequencies.

Figure 2-14: Large Sand Boil after the Darfield, 2010 Event (courtesy of GEER, 2010)

2.4 **Chapter Summary**

This chapter outlines some of the fundamental concepts of soil liquefaction. Soil liquefaction is typically considered in two categories: flow liquefaction and cyclic mobility. A soil is considered “liquefiable” if it meets susceptibility criteria and conditions are such that liquefaction is allowed to initiate. Susceptibility criteria include geologic, historical, compositional, and state components. Liquefaction initiation and mode (i.e. cyclic mobility or flow liquefaction) are highly dependent on the soil’s steady state strength. Once a soil is determined to be susceptible to liquefaction and initiation is deemed likely, then several types of effects may result. Effects of liquefaction include settlement, lateral spread, flow liquefaction, loss of bearing capacity, sand boils, increased lateral earth pressures, and alteration of ground motions.

3. CHARACTERIZATION OF SEISMIC LOADING

For assessment of seismically-induced liquefaction, a representative characterization of seismic loading is key. All models that estimate seismically-induced liquefaction contain some component of seismic loading. This seismic loading component can be presented in many different ways. This chapter discusses fundamental concepts behind seismic loading as it pertains to liquefaction. Although detailed discussion of the geology of earthquakes (i.e. plate tectonics, fault geometry, elastic rebound theory, etc.) is beyond the scope of this thesis, some background on this topic is helpful for fully understanding the seismic component of the seismic loading portion of liquefaction initiation models. The following discussion is provided to address topics specific to this research.

3.1 **Earthquakes**

As previously stated, the purpose of this chapter is to describe the characterization of seismic loading that affects liquefaction initiation. Earthquakes can be characterized in many ways, and often are described in terms of intensity, magnitude, or energy.

Earthquake intensity refers to a qualitative assessment of an earthquake's effects. Generally this is a subjective assessment on a scale of 1 to 10 or 12. Some intensity scales developed in the past include Rossi-Forel (RF), Modified Mercalli Index (MMI), Medvedev-Spoonheuer-Karnik (MSK), and the Japanese Meterological Agency (JMA) scales. The most commonly used scale worldwide (excluding Japan and Eastern Europe) is the MMI. For example, on the MMI scale, an earthquake intensity rank of 4 would mean “dishes, windows, doors disturbed; walls make cracking sound;… standing motor cars rocked noticeably” while a rank of 8 would mean “considerable damage in ordinary substantial buildings with partial collapse; fall of chimneys…; heavy furniture overturned” (USGS, 1989).

Earthquake magnitude is an objective description of earthquake size and is typically measured by instrumentation. Several definitions of magnitude exist, including Richter local magnitude (M_L), surface wave magnitude (M_s), body wave magnitude (m_b), and moment magnitude (M_w). The Richter local magnitude scale is commonly known as the “Richter Scale” and was based specifically on southern California earthquakes. Because of limitations in the measuring device that produces M_L values, the Richter scale saturates at values of 6.5 to 7.0. Values of M_s and m_b specifically target specific types of waves. The most commonly used magnitude today is M_w, which is based on the seismic moment of the earthquake. M_w is not associated with any single instrument and does not saturate at a maximum M_w value.

Earthquake energy is a measurement of the amount of energy released during the earthquake. Energy is difficult to measure, and therefore is often estimated based on earthquake magnitude.

3.2 Ground Motion Parameters (GMPs)

Ground motions produced by earthquakes are normally recorded using seismographs or accelerographs. These recording instruments create time histories, which are records of acceleration, velocity, or displacement over time. These records are used to estimate ground motion parameters (GMPs) that characterize an earthquake that has already occurred. Most GMPs fall into one of three categories: amplitude, frequency content, or duration.

Amplitude can be described by several GMPs, such as peak ground acceleration or peak acceleration (*PGA* or a_{max}), peak ground velocity or peak velocity (*PGV* or V_{max}), and peak ground displacement (*PGD*). Note that the amplitude GMPs are associated with peak or maximum values. Measurements of maximum values can be useful, but may not be sufficient to completely describe the earthquake ground motions. For example, consider the two time histories in Figure 3-1. The two time histories have approximately the same *PGA* and last about the same amount of time, but the earthquake associated with time history (b) likely would release more energy than the earthquake associated with time history (a). Thus, amplitude GMPs are useful, but they do not tell the whole story.

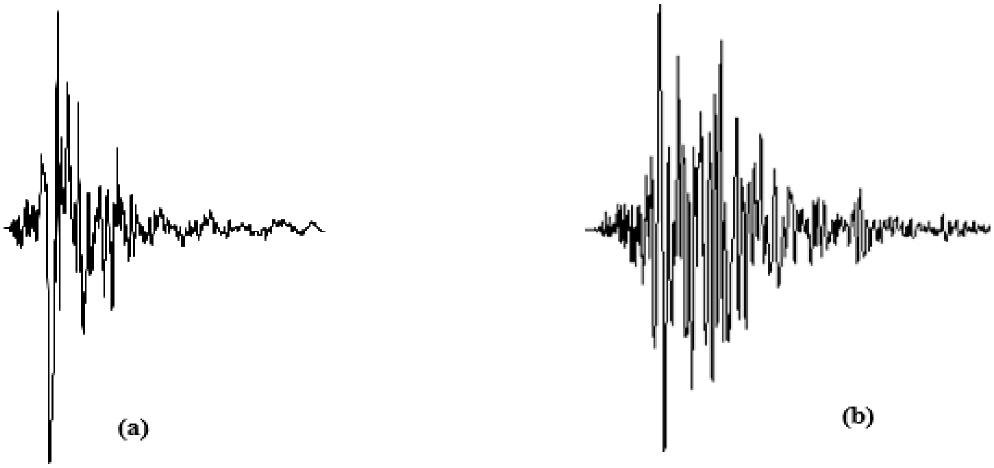

Figure 3-1: Comparison of Two Hypothetical Time Histories with Similar PGA Values

Other GMPs describe frequency content, which defines how amplitude is distributed across a range of frequencies (or periods). Frequency content is most often displayed as a Fourier spectrum, which breaks up the ground motion into individual frequencies and plots the amplitude associated with each frequency. Another common way to display frequency content is through a response spectrum. A response spectrum plots the structural response of a series of single degree of freedom oscillators instead of the raw amplitude. The structural response is typically represented as the spectral acceleration.

Engineers use duration GMPs to give a temporal aspect to earthquake characterization. The longer the strong ground motions last, the more energy is released. The most common duration GMP is bracketed duration, which is the length of time between the first and last occurrence of a pre-defined threshold acceleration (e.g. 0.05g).

Some GMPs such as Arias intensity (I_a) and cumulative absolute velocity (CAV) consider amplitude, frequency content, and duration. I_a is calculated by integrating the square of the acceleration time history according to the following equation:

$$I_a = \frac{\pi}{2g} \int_0^\infty \left[a(t) \right]^2 dt \tag{3-1}$$

where $a(t)$is the acceleration function with time and g is the acceleration of gravity. CAV is calculated by integrating the absolute value of the acceleration time history as follows:

$$CAV = \int_0^{T_d} \left| a(t) \right| dt \tag{3-2}$$

Some engineers prefer I_a or CAV to the other GMPs because they contain more than just amplitude or just duration information. However, it is best practice to use a combination of GMPs to characterize an earthquake so that a fuller and more detailed understanding of complex ground motions may be reached. As will be discussed in the next chapter, many of the popular liquefaction evaluation methods are based on a_{max} and M_w, but some researchers have developed evaluation methods based on I_a (Running, 1996; Kayen and Mitchell, 1997) and CAV (Mayfield, 2007). A comparison of energy-based methods and traditional a_{max}- and M_w -based methods has been performed by Green, 2001. Energy-based methods will not be discussed in this thesis, as the a_{max}-

and M_w -based procedures provide the basis for the derived simplified performance-based method presented later in this paper.

3.3 Ground Motion Prediction Equations (GMPEs)

If an engineer desires to predict what the GMPs will be from an earthquake that has not yet occurred, he or she may require empirical correlations to estimate these values. Using a database of earthquake time histories, researchers have developed empirical predictive equations to estimate GMPs from other earthquake-related variables (i.e. distance from fault, surface rupture length, etc.). These correlations are often called attenuation relationships or ground motion prediction equations (GMPEs). In some cases, GMPEs are based on limited data in a particular geographic area. An engineer using such limited GMPEs may need to rely on the ergodic assumption, which assumes that ground motions in two different geographic regions should be similar (all other variables held constant) despite the differences in their locations. Without this assumption, unique GMPEs would need to be developed for each geographic location, and there would be too little information for a robust correlation due to the general infrequency of earthquakes.

GMPEs have been modified and adjusted throughout the past decades as more earthquake data has become available. Each GMPE is based on different inputs and may provide estimates for a number of different GMPs. For example, Travasarou et al. (2003) developed an attenuation relationship for I_a based on magnitude, distance, fault mechanism, and site category. Boore et al. developed an early attenuation relationship for peak horizontal acceleration based on M_w, distance, and shear wave velocity of the soil (Boore et al. 1993). As more data from earthquake events accumulated, an update of these attenuation relationships was required. Five research teams were assigned to develop new GMPEs called the New Generation Attenuation (NGA) relationships (Abrahamson and Silva, 2008; Boore and Atkinson, 2008; Chiou and Youngs, 2008; Campbell and Bozorgnia, 2008; and Idriss, 2008). Each team received the same set of ground motion data and were required to develop unique GMPEs. These equations estimate *PGA*, *PGV*, and spectral acceleration based on a wide range of earthquake-related parameters. An even more recent update of the NGA relationships was completed in 2013 called NGA West 2 (Ancheta et al, 2014).

Though the NGA relationships were a significant step in the right direction, they were specifically designed for the western United States and areas of high seismicity from crustal sources. In addition, the NGA relationships were not designed for use in subduction zone events. Therefore, regions of low seismicity, near subduction zones, or in the eastern United States would need to consider alternative solutions. For example, some researchers have developed predictive relationships that are applicable in subduction zones (Youngs et al, 1997; Atkinson and Boore, 2003; and Zhao et al., 2006).

3.4 **Modifying Effects**

Several factors can modify or amplify ground motions at a given site. Though two different sites may experience earthquakes of the same M_w and distance from the respective sites, the two sites may observe very different ground motions. Some of the modifying effects discussed here include near source, basin, topographic, and site amplification effects. In areas where these effects may be encountered, engineers should carefully consider how the traditional GMPEs may need to be altered to account for greater ground motions than expected.

Near source effects include hanging wall and directivity effects. The hanging wall side of a fault is the side that is directly above or adjacent to the ground projection of the fault surface. This side of the fault typically experiences larger ground motions than the footwall side (i.e. opposite side of the fault from the hanging wall side). Donahue and Abrahamson (2014) observed that the “hanging wall effect” can increase ground motions at short distances from the fault.

Directivity is often identified by a "pulse" in the ground motions in a certain direction away from the location of fault rupture initiation. Researchers have found that ground motions resulting from forward-directivity are significantly different than other ground motions (Somerville et al., 1997; Bray and Rodriguez-Marek, 2004).

Basin and topographic effects may amplify the ground motions from a given seismic source. Using 3-D modeling of the Santiago Chile basin, Pilz et al (2011) found that basin effects could amplify ground motions to be significantly higher than the NGA relationships predict. Other researchers have also shown that basin effects may cause distortions in the ground motions (Graves et al., 1998; Gao et al., 2012). Assimaki and Jeong (2013) observed that ground motions during the M7.0 Haiti earthquake in 2010 were greatly amplified because of topographic relief.

Finally, site amplification effects alter ground motions in a high percentage of cases. Site amplification is an alteration of ground motions due to the reduced stiffness of surface soils. As the waves from the seismic source propagate through the bedrock and then through the soil layers on the way to the ground surface, the reduction in stiffness between the bedrock and the surface soil layers causes waves to change. Site amplifications are normally handled by multiplying the *PGA* by some amplification factor, F_a (Stewart et al., 2003). Some codes such as the AASHTO 2014 LRFD bridge code require amplification factors, F_{PGA}, based on site class. Site class is defined on a letter scale from A to F and is based on soil characteristics such as SPT blowcount (N) and average shear wave velocity in the upper 30m ($V_{s,30}$). If the site is especially sensitive, the amplification factor may be obtained from a site response analysis. Further discussion of site response analyses is beyond the scope of this thesis.

3.5 **Seismic Hazard Analysis**

Seismic hazard analyses are quantitative estimates of the ground shaking hazard at a given site caused by nearby seismic sources (e.g. faults, volcanoes, gridded sources, etc.). Seismic hazard analyses may be performed deterministically (i.e. one seismic scenario is considered) or probabilistically (i.e. uncertainties in the size, location and timing of the seismic source are explicitly considered). These analyses are typically performed when a structure is proposed to be built in a region where seismic ground shaking must be considered.

3.5.1 Deterministic Seismic Hazard Analysis

A deterministic seismic hazard analysis (DSHA) considers a single seismic scenario. This process begins with identifying and characterizing all seismic sources that could produce significant ground motions at the site of interest (Kramer, 1996). Each seismic source is then assigned a source-to-site distance parameter, which typically is the shortest distance to any portion of the source (i.e. closest point on the fault line or closest point of the gridded source). Using these source-to-site distances and specific characteristics of the seismic sources, GMPs are approximated using applicable attenuation relationships, such as the NGA relationships discussed previously. The controlling earthquake is identified as the seismic source that produces the worst case GMPs. The GMPs from the controlling earthquake can then be used to define the design ground motions that govern the design of structures at the site of interest.

Perhaps the least favorable aspect of a DSHA is the subjectivity of selecting a single seismic scenario to represent a site's seismic hazard. What if a different fault ruptures? What if the ground motions associated with the fault are much larger than anticipated by the controlling GMPs? What if the location of the rupture on the controlling fault is much farther away or much closer? There are many uncertainties associated with potential earthquake shaking, and these uncertainties are not explicitly captured in a DSHA. This is not to say that a DSHA is undesirable. A DSHA is appropriate as one method of seismic hazard analysis, but it should be carefully considered along with its limitations.

3.5.2 Probabilistic Seismic Hazard Analysis

Unlike a DSHA, a probabilistic seismic hazard analysis (PSHA) directly accounts for uncertainties associated with earthquake shaking. Before discussing the process involved in a PSHA, a brief summary of some uncertainties associated with earthquakes is presented.

Spatial Uncertainty

The actual location of a future seismic source is not known. Though a fault may be carefully identified and mapped, the initiation of the ground shaking may occur at any point along the fault. Some seismic sources are not well characterized, and are simply represented as gridded sources where ground shaking could initiate anywhere in that region. Spatial uncertainty is handled in a PSHA using multiple source-to-site distances for each possible seismic scenario.

Size Uncertainty

The size (e.g. M_w or PGA) of future ground motions is also unknown. Although many GMPEs have been developed to predict ground motions associated with a given source, the correlations are not perfect. There is significant scatter associated with these correlations. Two faults may have roughly the same features but produce markedly different ground motions at a given site. There is also natural uncertainty associated with random events (i.e. aleatory uncertainty). Uncertainty in the GMPEs is handled using standard deviations or other estimates of variability while aleatory uncertainty is handled by considering all possible seismic scenarios in the PSHA.

There is also the question of "Which GMPE should be used?", since there are several to choose from. This uncertainty (i.e. epistemic uncertainty) can be accounted for by using logic trees, which assign individual "weights" to each GMPE to be considered. This process essentially provides an average estimate of ground motions based on several GMPEs rather than just one.

Temporal Uncertainty

The timing of earthquake shaking is generally difficult to predict. Some faults characteristically rupture at a given recurrence rate, but still there is often some scatter associated with this rate. The temporal aspect of earthquake shaking is particularly important when asking the question "Will this structure experience this level of earthquake shaking during its design life?". Earthquakes are typically modeled as random events, despite evidence that earthquakes may be more time-dependent than originally assumed (Parsons, 2008; Fitzenz and Nyst, 2015). In a PSHA, the Poisson model is most commonly used to describe the temporal aspect of earthquakes. The model is modified to predict the probability of at least one exceedance of a given ground shaking level in a period of *t* years by the following expression:

$$P\left[N \geq 1\right] = 1 - e^{-\lambda_m t} \tag{3-3}$$

where λ_m is the average annual rate of occurrence of the event.

The first step in a PSHA is similar to the first step in a DSHA, which is to identify and characterize potential earthquake sources (Kramer, 1996). The difference is that in a PSHA, the probability distribution of potential rupture locations is required. The second step is to develop a recurrence relationship that gives the average rate at which an earthquake of a certain size or greater will occur. The third step is to estimate GMPs for each possible earthquake location and size using GMPEs and the associated probability density functions. Finally, the uncertainties in each of the first three steps are incorporated to obtain the probability that the GMP will be exceeded during a particular time period. One of the common ways to display the results of a PSHA is to plot the results together as a seismic hazard curve. Seismic hazard curves are plotted with the average annual exceedance rate (λ_{y*}) on the ordinate and the GMP of interest on the abscissa. Points on a seismic hazard curve are estimated using the following equation:

$$\lambda_{y*} = \sum_{i=1}^{N_s} \sum_{j=1}^{N_M} \sum_{k=1}^{N_R} v_i P\left[Y > y^* \mid m_j, r_k\right] P\left[M = m_j\right] P\left[R = r_k\right] \tag{3-4}$$

where N_s, N_M and N_R are the number of increments considered for sources, magnitudes, and distances, respectively; Y is the GMP of interest; y^* is a given threshold GMP value; υ_i is the average rate of threshold magnitude exceedance; $P[Y<y^*| m_j, r_k]$ is the probability of the value of Y exceeding y^* given a combination of magnitude and distance; and $P[M = m_j]$ and $P[R = r_k]$ are the probabilities of the magnitude being equal to the m_j value and the distance being equal to r_k, respectively. Essentially this summation equation systematically considers each possible source, magnitude, and distance scenario and multiplies by the associated probabilities of the scenario (and the GMPE) and sums all the possible scenarios into one λ_{y*} value. This process is repeated for each value of y^* to create the seismic hazard curve. A sample seismic hazard curve is provided below as Figure 3-2. Notice that as *PGA* increases, the mean annual rate of exceedance decreases. This is a typical relationship between GMPs and λ. Earthquakes that produce larger GMPs are typically less frequent while earthquakes that produce smaller GMPs may be more frequent and therefore have a higher mean annual rate of exceedance.

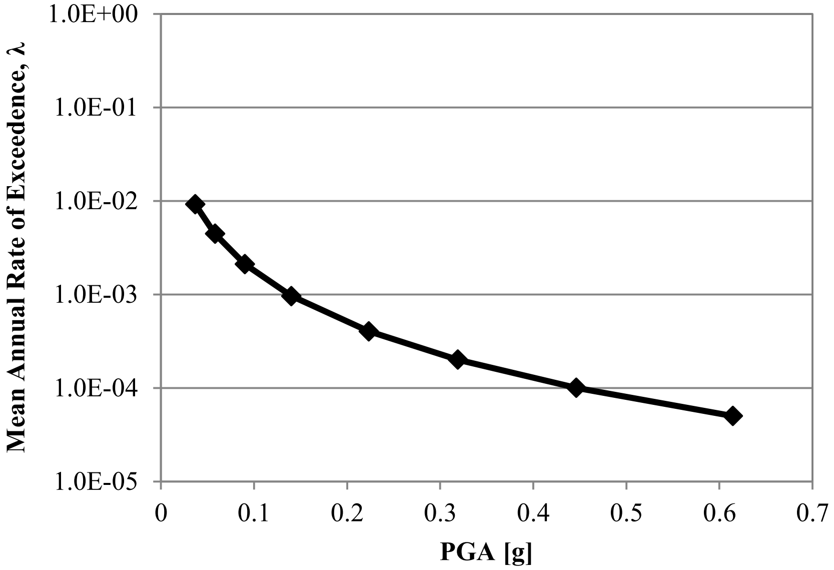

Figure 3-2: Sample Seismic Hazard Curve for PGA

3.6 Chapter Summary

A representative characterization of seismic loading is key to an accurate liquefaction triggering analysis. This chapter identifies some of the common parameters (GMPs) used in characterization of seismic loading and describes some of the predictive equations (GMPEs) used to estimate GMPs associated with earthquakes that have not yet occurred. Some modifying effects such as basin, topographic, and near source are also briefly discussed. Seismic hazard analyses provide site-specific estimates of earthquake hazard and are typically performed deterministically (DSHA) or probabilistically (PSHA). A PSHA accounts for uncertainties associated with ground motions such as timing, size, and location. The steps involved in a DSHA and in a PSHA are outlined, and seismic hazard curves are introduced.

4. EVALUATION OF LIQUEFACTION INITIATION POTENTIAL

After establishing a soil's liquefaction susceptibility and characterizing the seismic loading at a given site through a PSHA or DSHA, practicing engineers must somehow evaluate and quantify a site's liquefaction initiation potential using common tools and tests at their disposal. This chapter provides an overview of some common evaluation methods.

Most evaluation methods used in practice today are divided into two categories: cyclic strain-based and cyclic stress-based. Cyclic strain methods are not commonly used because it is often difficult to measure the strain in a soil subjected to earthquake loading (Seed, 1980). Though it is difficult to measure strain, the cyclic strain approach is appealing because pore pressures have been shown to be strongly correlated with strain amplitude. The cyclic strain approach is not discussed further in this thesis because it is less common than cyclic stress-based approaches. More information on cyclic strain approaches can be found in these references: Dobry and Ladd (1980), Dobry et al. (1982), Dobry et al (1984), and Vasquez-Herrara and Dobry (1988).

The more commonly-used cyclic stress approach is based on two components: cyclic resistance ratio (*CRR*) and cyclic stress ratio (*CSR*). The *CRR* is a measure of the soil's ability to resist liquefaction, and the *CSR* is a measure of the seismic loading placed on the soil. The factor of safety against liquefaction, FS_L is equal to:

$$FS_L = \frac{CRR}{CSR} \tag{4-1}$$

If the FS_L is less than 1.0, the resistance (*CRR*) is less than the loading (*CSR*), which indicates that liquefaction of a susceptible soil may occur. Seed et al. (1975) proposed a way to calculate *CSR* by converting irregular earthquake time histories of shear stress to equivalent number of uniform cycles in the laboratory and then using a weighting procedure to estimate the number of equivalent cycles (N_{eq}) that would produce the same increase in pore pressure as in the seismic time history. This weighting scheme stated that cyclic shear stress was 65% of the maximum shear stress from the time history. Time histories of shear stress may not always be available for every site, so Idriss and Seed (1971) provided a simplified way to estimate shear stress at a site with level or gently sloping ground:

$$\tau_{cyc} = 0.65 \frac{a_{\max}}{g} \sigma_v r_d \tag{4-2}$$

where σ_v is the vertical stress acting on the soil layer of interest and r_d is a stress reduction factor. This reduced shear stress would be applied N_{eq} times to produce the same increase in pore pressures as a representative earthquake would. *CSR* can then be calculated by normalizing τ_{cyc} by the effective vertical stress, σ'_v acting on the soil layer of interest as shown in the following equation:

$$CSR = \frac{\tau_{cyc}}{\sigma'_v} = 0.65 \frac{a_{\max}}{g} \frac{\sigma_v}{\sigma'_v} r_d \tag{4-3}$$

Equation (4-3) is commonly accepted in many evaluation methods as a valid way to calculate *CSR*. The major difference between the common evaluation methods of today is the way in which *CRR* is determined. Two common ways of characterizing *CRR* include laboratory testing and in situ tests coupled with relationships developed from observed liquefaction events. Several laboratory tests have been used to estimate the resistance of soil to liquefaction, including cyclic triaxial test, resonant column test, cyclic direct simple shear test, and cyclic torsional shear test.

For several years, laboratory tests were used extensively to estimate *CRR*. However, it was soon discovered that liquefaction initiation was not dependent on initial density and stress conditions alone, as many researchers previously thought (Kramer 1996). Other factors (specimen preparation technique, strain history, overconsolidation, length of time under confining pressure, etc.) also affect liquefaction potential (Pyke et al., 1975; Ladd, 1974; Finn et al., 1970; Seed and Peacock, 1971; Ohsaki, 1969). Thus, determination of resistance using laboratory testing is rarely performed. The remainder of this section focuses on common in situ methods.

4.1 **Empirical, In Situ Deterministic Methods**

Deterministic in situ methods for estimating *CRR* include cone penetrometer test (CPT) methods (Douglas et al., 1981; Robertson and Campanella, 1985; Seed and De Alba, 1986; Mitchell and Tseng, 1990; Kayen et al., 1992; Kayen and Mitchell, 1997; Suzuki et al., 2003; Carraro et al., 2003; Baziar and Nilipour, 2003; Ku et al., 2004; Andrus et al., 2004; Moss et al., 2006; Boulanger and Idriss, 2014), shear wave velocity (V_s) methods (Stokoe, et al., 1988; Finn, 1991; Tokimatsu, et al., 1991; Kayen et al., 1992; Andrus, et al., 2004; Kayen et al., 2013), dilatometer methods (Marchetti, 1982; Robertson and Camponella, 1986; Reyna and Chameau, 1991), and SPT methods. SPT methods will be discussed in greater detail in this chapter because these are the most commonly used methods and the simplified performance-based method developed in this thesis is dependent upon these SPT-based methods.

SPT-based methods of liquefaction evaluation have been shown to be reasonable because some of the same factors that affect SPT resistance also affect liquefaction resistance (i.e. density, overconsolidation, non-uniformity, angularity, fines content). Seed and Idriss (1971) provided the first chart that showed *CSR* and *SPT* resistance for sites that did liquefy and sites that did not liquefy under $M_w = 7.5$. This chart was used to identify the “line” between soils that liquefy and soils that do not liquefy. Ever since this first chart was made, researchers have attempted to recreate similar plots that redefine the distinction between soils that liquefy and soils that do not liquefy. Three such revised models have become popular in practice: Youd et al. (2001), Cetin et al (2004), and Idriss and Boulanger (2008, 2010). There has been much confusion and disagreement over which method is appropriate to use in practice. In light of this current confusion, this thesis will use both the Cetin et al. (2004) and the Idriss and Boulanger (2008) models without choosing one over the other (the Youd et al., 2001 model is somewhat similar to the Idriss and Boulanger, 2008 model, so it is not a focus in this thesis).

4.1.1 Cetin et al. (2004) Deterministic Model

The Cetin et al. (2004) deterministic model uses Equation (4-3) to calculate *CSR* with the specification that r_d is calculated as:

$$d \geq 20m:$$

$$r_d = \frac{\left[1 + \dfrac{-23.013 - 2.949 \cdot a_{\max} + 0.999 \cdot M_w + 0.0525 \cdot V^*_{s,12m}}{16.258 + 0.201 \cdot e^{0.341\left(-d + 0.0785 \cdot V^*_{s,12m} + 7.586\right)}}\right]}{\left[1 + \dfrac{-23.013 - 2.949 \cdot a_{\max} + 0.999 \cdot M_w + 0.0525 \cdot V^*_{s,12m}}{16.258 + 0.201 \cdot e^{0.341 \cdot \left(0.0785 \cdot V^*_{s,12m} + 7.586\right)}}\right]}$$

(4-4)

$$d < 20m:$$

$$r_d = \frac{\left[1 + \dfrac{-23.013 - 2.949 \cdot a_{\max} + 0.999 \cdot M_w + 0.0525 \cdot V^*_{s,12m}}{16.258 + 0.201 \cdot e^{0.341\left(-20 + 0.0785 \cdot V^*_{s,12m} + 7.586\right)}}\right]}{\left[1 + \dfrac{-23.013 - 2.949 \cdot a_{\max} + 0.999 \cdot M_w + 0.0525 \cdot V^*_{s,12m}}{16.258 + 0.201 \cdot e^{0.341 \cdot \left(0.0785 \cdot V^*_{s,12m} + 7.586\right)}}\right]} - 0.0046 \cdot \left(d - 20\right)$$

where $V^*_{s,12m}$ is the average shear wave velocity in the upper 12 m of the soil profile (in m/s) and d is the depth from the ground surface to the soil layer of interest (in meters). The *CRR* curve they regressed is defined by the following equation:

$$CRR = \exp\left[\frac{N_{1,60}\cdot\left(1+0.004FC\right)-29.53\cdot\ln\left(M_w\right)-3.70\cdot\ln\left(\frac{\sigma_v'}{P_a}\right)+0.05FC+16.85}{13.32}\right] \tag{4-5}$$

where P_a is atmospheric pressure and *FC* is fines content expressed as an integer.

4.1.2 Idriss and Boulanger (2008, 2010) Deterministic Model

The Idriss and Boulanger (2008, 2010) deterministic model uses a slight modification of Equation (4-3) to calculate *CSR*. Their equation is:

$$CSR = 0.65\frac{a_{\max}}{g}\frac{\sigma_v}{\sigma_v'}\left(r_d\right)\frac{1}{MSF\cdot K_\sigma} \tag{4-6}$$

where r_d is the stress reduction factor specified by Idriss and Boulanger (2008), *MSF* is the magnitude scaling factor, and K_σ is the depth correction factor as calculated according to Idriss and Boulanger (2008). The *CRR* curve they regressed is defined as:

$$CRR_{P_L=50\%} = \exp\left[\left(\frac{\left(N_1\right)_{60,cs}}{14.1}\right)+\left(\frac{\left(N_1\right)_{60,cs}}{126}\right)^2-\left(\frac{\left(N_1\right)_{60,cs}}{23.6}\right)^3+\left(\frac{\left(N_1\right)_{60,cs}}{25.4}\right)^4-2.8\right] \tag{4-7}$$

A plot of this *CRR* curve is provided as Figure 4-1. Note that most of the cases marked as “liquefaction” are above the *CRR* line and most of the cases marked as “no liquefaction” are below the *CRR* line. However, there are some cases that do not follow this convention. These cases indicate that the *CRR* curve is not perfect in distinguishing between liquefying and non-liquefying soils. The same is also true of the Cetin et al. (2004) deterministic model. To address some of this associated scatter in the data, researchers developed probabilistic empirical models.

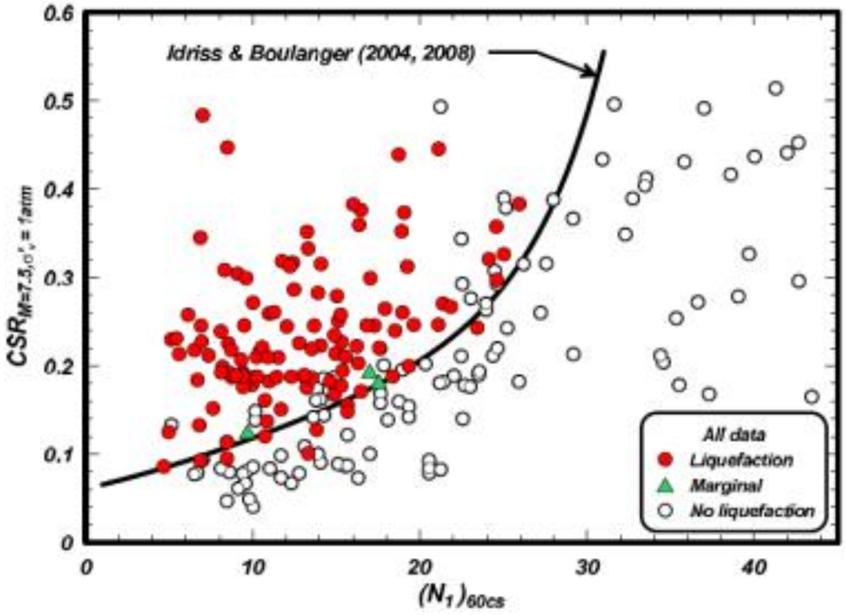

Figure 4-1: Deterministic *CRR* Curve for Idriss and Boulanger (2010) (after Idriss and Boulanger, 2010)

4.2 **Empirical Probabilistic Methods**

As previously mentioned, deterministic models did not completely capture the difference between liquefying and non-liquefying soils included in their case histories. Using powerful statistical tools, researchers developed probabilistic models that characterize the scatter in the data and include probabilities in the *CRR* equations. In essence, several *CRR* curves are regressed for each model and each curve has an associated probability of liquefaction (P_L). Some of the first attempts to quantify the probability of liquefaction were performed by Liao et al. (1988), Youd and Noble (1997), and Toprak et al. (1999). These methods were based on relatively small databases and with early statistical tools. More recent models (Cetin et al., 2004; Boulanger and Idriss, 2012; Juang et al., 2012) have been developed with larger databases, more computing power and Bayesian statistical tools.

4.2.1 Probabilistic Cetin et al. (2004) Procedure

Cetin et al. (2004) in the probabilistic version of their empirical model calculated *CRR* in the same way as in the deterministic version, except for a few changes in constants to incorporate uncertainty and an addition of the P_L term, as shown:

$$CRR = \exp\left[\frac{N_{1,60}\cdot\left(1+\theta_1 FC\right)-\theta_3\cdot\ln\left(M_w\right)-\theta_4\cdot\ln\left(\frac{\sigma_v'}{P_a}\right)+\theta_5 FC+\theta_6+\sigma_\varepsilon\cdot\Phi^{-1}\left(P_L\right)}{\theta_2}\right] \tag{4-8}$$

where Φ^{-1} is the inverse standard cumulative normal distribution function, and the values of θ_1 through θ_6 and σ_ε are provided in Table 4-1. The values of θ_1 through θ_6 in this table already include model error, but the coefficients marked as "measurement/estimation errors included" incorporates uncertainties associated with input parameters (i.e. $N_{1,60}$, *FC*, etc.). Note that there is a different *CRR* for each P_L of interest. This is illustrated in Figure 4-2 where several *CRR* curves of different P_L values are presented.

Table 4-1: Cetin et al. (2004) Model Coefficients With and Without Measurement/Estimation Errors (from Kramer and Mayfield, 2007)

Measurement/estimation errors	θ_1	θ_1	θ_1	θ_1	θ_1	θ_1	σ_ε
Included	0.004	13.79	29.06	3.82	0.06	15.25	4.21
Removed	0.004	13.32	29.53	3.70	0.05	16.85	2.70

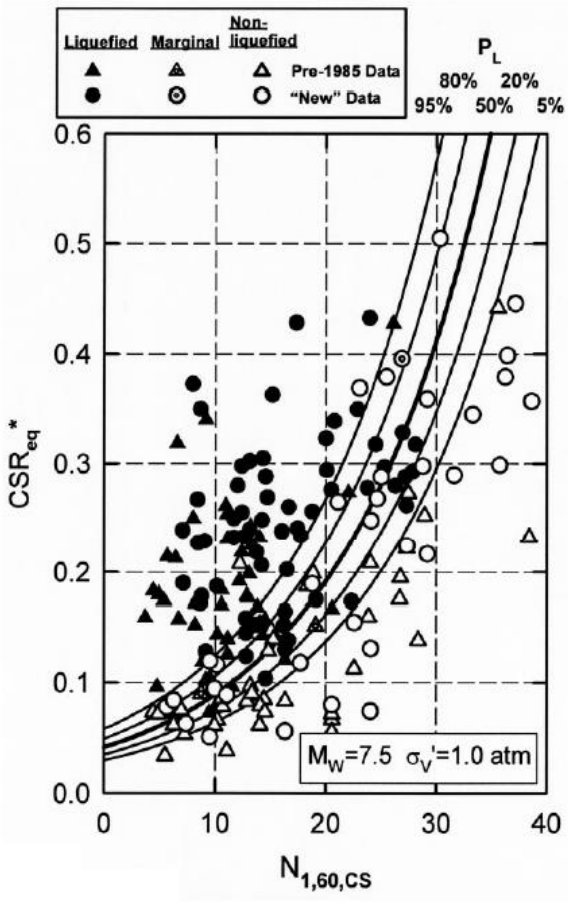

Figure 4-2: Probabilistic *CRR* Curves (after Cetin et al., 2004)

4.2.2 Probabilistic Boulanger and Idriss (2012) Procedure

Boulanger and Idriss (2012) also developed a probabilistic version of their empirical liquefaction triggering model. This probabilistic model looks very similar to the deterministic version except for a few adjustments to the coefficients and the addition of a P_L term:

$$CRR = \exp\left[\left(\frac{(N_1)_{60,cs}}{14.1}\right)+\left(\frac{(N_1)_{60,cs}}{126}\right)^2-\left(\frac{(N_1)_{60,cs}}{23.6}\right)^3+\left(\frac{(N_1)_{60,cs}}{25.4}\right)^4-2.67+\sigma_{\ln(R)}\cdot\Phi^{-1}(P_L)\right] \quad (4\text{-}9)$$

where $\sigma_{ln(R)}$ is the standard deviation associated with the natural log of the source-to-site distance. The value of $\sigma_{ln(R)}$ depends on whether parametric uncertainty (i.e. uncertainty associated with input parameters) or model uncertainty (i.e. imperfection in the predictions of the model) is being considered. If model uncertainty alone is considered, then $\sigma_{ln(R)}$ is equal to 0.13. If both model and parametric uncertainty are considered, then $\sigma_{ln(R)}$ is equal to 0.277 (Franke et al. 2014a). Several *CRR* curves for varying P_L values are plotted in Figure 4-3.

The Boulanger and Idriss method has since gone through another update (2014), which adjusted the *MSF* parameter used to calculate *CSR* (Equation (4-6)) and added a probabilistic CPT-based liquefaction triggering model (Boulanger and Idriss, 2014 and 2015). This 2014 version of their model will be mentioned briefly throughout the remainder of the paper, but the basis of the newly proposed performance-based procedure presented in this thesis is based on the 2012 version.

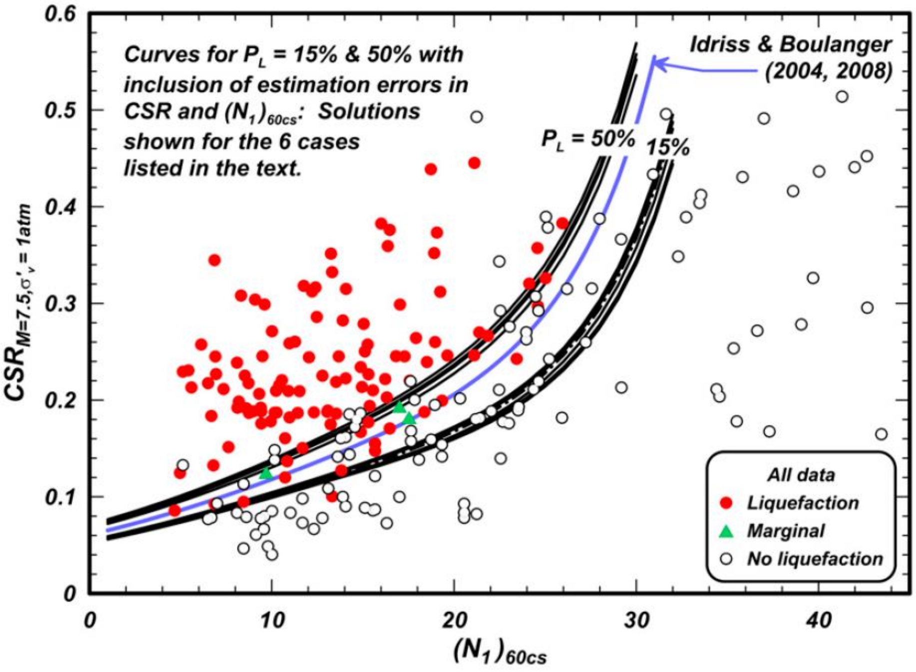

Figure 4-3: Probabilistic *CRR* Curves for P_L = 15% and 50% with Inclusion of Parametric Uncertainty (after Boulanger and Idriss, 2012)

4.3 **Chapter Summary**

In this chapter, several methods of liquefaction evaluation are introduced. Strain-based methods are only briefly mentioned while discussion of stress-based methods commands the majority of this chapter. Though many CPT, shear wave velocity, and dilatometer-based methods have been developed, these methods are only cited for reference. The more common SPT-based methods, which provide the basis for the new simplified procedure derived in this thesis, are discussed in greater detail. SPT-based methods of liquefaction evaluation have been shown to be reasonable because some of the same factors that affect SPT resistance also affect liquefaction resistance (i.e. density, overconsolidation, non-uniformity, angularity, fines content). In particular, the two major SPT-based methods in use today are highlighted, which are Idriss and Boulanger (Idriss and Boulanger, 2008 and 2010; Boulanger and Idriss, 2012 and 2014) and Cetin et al. (2004). Each model has both a deterministic and a probabilistic approach. Deterministic methods attempt to draw a single boundary *CRR* line that differentiates between soils that liquefy and soils that do not liquefy. Probabilistic methods rely on powerful statistical tools to estimate probability of liquefaction (P_L) for several *CRR* curves, each with an associated P_L.

5. PERFORMANCE-BASED EARTHQUAKE ENGINEERING

For decades, engineers have been trying to make structures more resistant against earthquake-induced damage. In an attempt to guide engineers towards safe design practices, engineers and seismologists have developed seismic design codes. These codes have been constantly reviewed and edited as new understanding and better practices have been developed. Current codes are somewhat restrictive in the way they prescribe precise design methods and acceptable building materials instead of focusing on the desired end result (Mayfield, 2007). To refocus on the end result (or performance) of a structure rather than the design process alone, the Pacific Earthquake Engineering Research (PEER) Center has developed a new approach to seismic design (Cornell and Krawinkler, 2000; Krawinkler, 2002; Deierlein et al., 2003). This new approach, called performance-based earthquake engineering (PBEE), focuses on meeting the needs of the structure's stakeholders (e.g. owners, users, government, and the public) rather than minimum code specifications. Three key components of PBEE include the following:

1) Performance levels and objectives can be quantified.
2) Performance can be reliably predicted.
3) The cost of improved performance can be evaluated so that rational trade-offs can be based on considerations of life-cycle cost rather than on construction costs alone (Mayfield, 2007).

The importance of the first key component cannot be overstated. In many cases in the past, each person involved in the seismic design process had different objectives and definitions of what "acceptable performance" meant. Seismologists focused on magnitudes and accelerations, engineers calculated stresses and factors of safety, owners cared about the economic viability of the project, and government officials and the public were primarily concerned about life safety. This is not to say that each group did not care about the other groups' concerns, but rather it was difficult to communicate each unique definition of "performance" in a consistent and understandable manner. Figure 5-1 provides an illustration of some different ways of measuring performance (after Moehle and Dierlein, 2004). The PBEE framework developed by PEER is especially useful for the purpose of streamlining the decision-making process and allowing each group to communicate effectively.

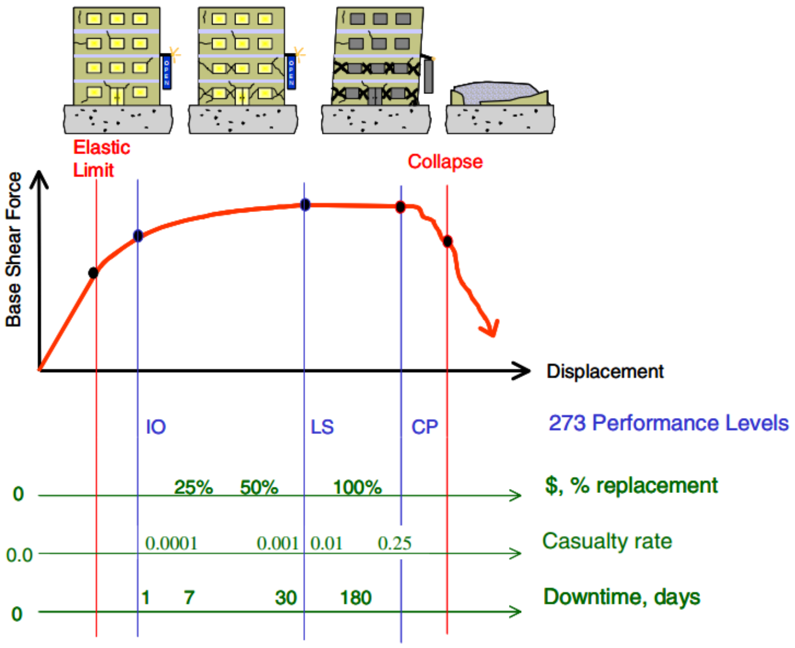

Figure 5-1: Visualization of Performance-Based Earthquake Engineering (after Moehle and Dierlein, 2004)

5.1 PBEE Framework Developed by PEER

The following framework parameters defined by PEER describe the components of the PBEE method.

- *Intensity measure* (*IM*): a characterization of ground motion. Examples: a_{max} or I_a.
- *Engineering Demand Parameter (EDP)*: an effect of the *IM* on a system of interest. Examples: excess pore pressures or FS_L.
- *Damage Measure (DM)*: a physical effect associated with the *EDP*. Examples: settlement or lateral displacement.
- *Decision Variable (DV)*: a useful parameter for decision-makers that characterizes risk associated with the *DM*s. Examples: casualties, repair cost, downtime, or economic loss.

The end goal of the PBEE framework is to quantify the mean annual rate of exceedance (or frequency) of one or more key *DV*s (λ_{DV}). The equation to calculate λ_{DV} is shown below.

$$\begin{aligned}\lambda = \sum_{k=1}^{N_{DM}} \sum_{j=1}^{N_{EDP}} \sum_{i=1}^{N_{IM}} & P\left[DV > dv \mid DM = dm_k\right] \times \\ & P\left[DM = dm_k \mid EDP = edp_j\right] P\left[EDP = edp_j \mid IM = im_i\right] \Delta\lambda_{im_i}\end{aligned} \tag{5-1}$$

where $P[a|b]$ describes the conditional probability of a given b; N_{DM}, N_{EDP}, and N_{IM} = number of increments of *DM*, *EDP*, and *IM*, respectively; and $\Delta\lambda_{\text{im}}$ is the incremental mean annual rate of exceedance for intensity measure im_i. The structure of this equation should look somewhat familiar, because it uses the total probability theorem as a PSHA does (see Equation (3-4)). Note that this framework equation incorporates each parameter from *IM*s like *PGA* all the way up to *DV*s like casualties or economic loss, and that the uncertainty of each *IM*, *EDP*, *DM*, and *DV* is built into the respective $P[a|b]$ terms. Another way of communicating λ_{DV} is through a return period (T_r), which is the inverse of λ_{DV}.

The performance-based decision-making process provided through PEER's PBEE framework is revolutionary. The flexibility and confidence provided through this process could have a tremendous effect on the way practicing engineers approach seismic design. For example, engineers and stakeholders can decide together what level of damage or what return period is acceptable and economical within the guidance of the code. Some buildings must be functional after a large earthquake, and therefore will cost a large sum up front during construction for such a robust design. Other buildings may not be expected to still function after a large earthquake, and therefore could be built using an inexpensive initial design and rebuilt after the earthquake. It should not be required that a warehouse holding inexpensive goods be designed to perform the same way a hospital, fire station, or nuclear power plant should. On the other hand, a stakeholder wishing to build a structure to a higher performance level than the current code affords should not be restricted or forced to go through a confusing and frustrating process of adjusting the code-based designs to provide a more robust design. This is where PBEE can provide an objective approach to achieve the goals of the stakeholders and meet the safety requirements of those who will use the structure.

5.1.1 Hazard Curves for *DV*

As previously discussed in the section about PSHAs, hazard curves plot the mean annual rate of exceedance of some parameter for each parameter in question. A hazard curve in the PBEE framework could be made for any of the framework parameters (*IM*, *EDP*, *DM*, and *DV*). Equation (5-1) provides the calculation necessary to create a hazard curve for the *DV* of interest, which could be casualties, down time, or economic loss. With such a hazard curve (like the one shown in

Figure 5-2), decision-makers can easily and clearly see the frequency of different levels of loss (in lives, dollars, or time), which can lead to a more informed decision about the final design of a structure. In addition, these decision-makers can have confidence in the hazard curve because it was developed using a range of possible scenarios rather than just one hypothetical scenario that may not occur.

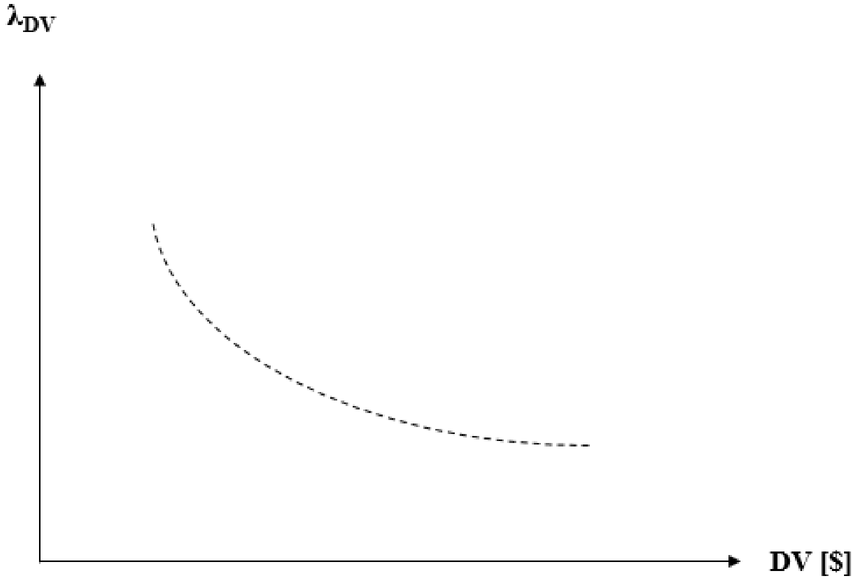

Figure 5-2: Illustration of a Hypothetical Hazard Curve with Economic Loss as the *DV*

5.2 **Performance-Based Liquefaction Initiation**

As discussed previously, current conventional liquefaction assessment methods use deterministic equations and a single ground motion scenario. Unfortunately, this deterministic approach does not account for uncertainties or probabilities associated with seismic hazards and does not consider the wide range of possible combinations of GMPs. According to Kramer and Mayfield (2007), deterministic methods have been shown to produce inconsistent estimates of actual liquefaction hazards when applied to areas of different seismicity levels. They suggest that practicing engineers consider liquefaction analyses in a performance-based manner rather than in a deterministic manner. To illustrate how a performance-based approach to liquefaction assessment works, the remainder of this chapter will explain the incorporation of liquefaction initiation models into the PBEE framework.

Liquefaction parameters such as FS_L, SPT blow count required to resist liquefaction (N_{req}), P_L, and CSR are considered *EDP*s in the PBEE approach. To incorporate these liquefaction parameters into the PBEE approach, the $P[EDP|IM]$ term must be developed using probabilistic liquefaction triggering models such as Cetin et al. (2004) and Boulanger and Idriss (2012). The process for developing the $P[EDP|IM]$ term for each of these two popular liquefaction triggering models is summarized here.

5.2.1 Incorporation of Probabilistic Cetin et al. (2004) Model into PBEE

Kramer and Mayfield (2007) first incorporated the Cetin et al. (2004) into the PBEE framework by developing an equation for the mean annual rate of *non*exceedance of a selected FS_L^* (Λ_{FSL^*}). The term for nonexceedance was required because FS_L, unlike many other *EDP*s, is more favorable when its value is higher and less favorable when its value is lower. Thus, the engineer would be most interested in when the FS_L might be expected to *not* exceed a given value of FS_L^*. The equation for Λ_{FSL} was defined as

$$\Lambda_{FS_L^*} = \sum_{i=1}^{N_{IM}} P\left[FS_L < FS_L^* \mid IM_i\right] \Delta\lambda_{IM_i} \qquad (5\text{-}2)$$

This equation, based on the PBEE framework, assumes that the *IM* is a sufficient measure to predict the *EDP*. However, upon inspection of the Cetin et al. (2004) model, the FS_L term is not dependent on one *IM* alone. FS_L is dependent on both *PGA* and M_w. Therefore, Kramer and

Mayfield (2007) modified Equation (5-2) to include a combination of two *IM*s in the following manner:

$$\Lambda_{FS_L^*} = \sum_{j=1}^{N_{M_W}} \sum_{i=1}^{N_{a_{\max}}} P\left[FS_L < FS_L^* \mid a_{\max,i}, m_j\right] \Delta\lambda_{a_{\max,i}, m_j} \tag{5-3}$$

where N_M and N_{amax} are the number of subdivided magnitude and peak acceleration increments, respectively; and $\Delta\lambda_{a_{\max,i}, m_j}$ is the incremental mean annual rate of exceedance for a_{max} and magnitude, m_j. Note that there are two summation symbols in this equation, which means that this equation considers every feasible combination of a_{max} and M_w. Kramer and Mayfield (2007) suggested that the conditional probability term in Equation (5-3) can be calculated by first solving for P_L from the probabilistic Cetin et al. (2004) equation (Equation (4-8)) and then calculating $P\left[FS_L < FS_L^* \mid a_{\max,i}, m_j\right]$ where $CSR = CSR_{eq,i} \cdot FS_L^*$ (with $CSR_{eq,i}$ computed from $a_{max,i}$) and $M_w = m_j$, like so:

$$P\left[FS_L < FS_L^* \mid a_{\max,i}, m_j\right] = \Phi\left[-\frac{(N_1)_{60}(1+\theta_1 FC) - \theta_2 \ln\left(CSR_{eq,i} \cdot FS_L^*\right) - \theta_3 \ln m_j - \theta_4 \ln\left(\frac{\sigma_v'}{p_a}\right) + \theta_5 FC + \theta_6}{\sigma_\varepsilon}\right] \tag{5-4}$$

Another way that Kramer and Mayfield (2007) characterized liquefaction hazard was in terms of N_{req}. They stated that liquefaction would occur when $N < N_{req}$ or when $FS_L < 1.0$, and therefore, $P\left[N < N_{req}\right] = P\left[FS_L < 1.0\right]$. The following equation can be used to calculate the mean annual rate of exceedance for N_{req}* at a depth of interest:

$$\lambda_{N_{req}^*} = \sum_{j=1}^{N_{M_W}} \sum_{i=1}^{N_{a_{\max}}} P\left[N_{req} > N_{req}^* \mid a_{\max,i}, m_j\right] \Delta\lambda_{a_{\max,i}, m_j} \tag{5-5}$$

where

$$P\left[N_{req} > N_{req}^{*} \mid a_{\max,i}, m_j\right] = \Phi\left[-\frac{N_{req}^{*}\left(1+\theta_1 FC\right) - \theta_2 \ln\left(CSR_{eq,i}\right) - \theta_3 \ln m_j - \theta_4 \ln\left(\dfrac{\sigma_v'}{p_a}\right) + \theta_5 FC + \theta_6}{\sigma_\varepsilon}\right] \quad (5\text{-}6)$$

5.2.2 Incorporation of Probabilistic Boulanger and Idriss (2012) Model into PBEE

Franke et al. (Franke and Wright, 2013; Franke et al., 2014a) incorporated the Boulanger and Idriss (2012) into the PBEE framework by solving for the conditional probability term required in the calculation of $\lambda_{FS_L^*}$. They did this by first solving for the P_L term found in the probabilistic Boulanger and Idriss (2012) model (Equation (4-9)) and solving for $P\left[FS_L < FS_L^{*} \mid a_{\max,i}, m_j\right]$ in a similar manner as Kramer and Mayfield (2007) did. The resulting equation for $P\left[FS_L < FS_L^{*} \mid a_{\max,i}, m_j\right]$ is:

$$P\left[FS_L < FS_L^{*} \mid a_{\max,i}, m_j\right] = \Phi\left[-\frac{\left(\dfrac{(N_1)_{60,cs}}{14.1}\right) + \left(\dfrac{(N_1)_{60,cs}}{126}\right)^2 - \left(\dfrac{(N_1)_{60,cs}}{23.6}\right)^3 + \left(\dfrac{(N_1)_{60,cs}}{25.4}\right)^4 - 2.67 - \ln\left(FS_L^{*} \cdot CSR_{M=7.5,\sigma_v'=1atm,i,j}\right)}{\sigma_\varepsilon}\right] \quad (5\text{-}7)$$

where $CSR_{M=7.5,\sigma_v'=1atm}$ is the cyclic stress ratio corresponding to an equivalent $M_w = 7.5$ earthquake under an effective confining stress of 1 atmosphere.

5.3 **Chapter Summary**

This chapter introduces PBEE as a relatively new approach to seismic design that focuses on the results or outcomes of a design under earthquake loading rather than pre-determined code-based specifications. PEER developed a PBEE framework that incorporates several parameters such as intensity measures, engineering demand parameters, damage measures, and decision variables. This framework allows various stakeholders (i.e. engineers, owners, government, and the general public) to come to a combined decision about a seismic design based on the overall outcome of casualties, economic loss, or downtime. These stakeholders can have confidence in the PBEE method because it directly accounts for the uncertainties associated with each of the framework parameters and considers multiple earthquake scenarios rather than a single deterministic event. Kramer and Mayfield (2007) and Franke and Wright (2013) previously incorporated the Cetin et al. (2004) and Boulanger and Idriss (2012) probabilistic liquefaction triggering models, respectively, into the PBEE framework by solving for the conditional probability term, $P\left[FS_L < FS_L^* \mid a_{\max,i}, m_j\right]$ for each model. This incorporation of liquefaction parameters as *EDP*s in the PBEE framework allows for a performance-based analysis of liquefaction hazard.

6. DERIVATION OF A NEW SIMPLIFIED PERFORMANCE-BASED PROCEDURE

Though PBEE has gained popularity over the past decade and researchers like Kramer and Mayfield (2007) and Franke and Wright (2013) have incorporated liquefaction triggering into the PBEE framework, the PBEE procedure still remains somewhat difficult for engineers to perform on a regular basis. While some have developed software such as *WSliq* (Huang, 2008; Kramer, 2008) and *PBLiquefY* (Wright, 2013; Franke et al., 2014d) to perform PBEE calculations, these programs require some familiarity with PBEE principles that is not yet common among all engineers. To make PBEE more readily available to a broader range of engineers and to facilitate more rapid PBEE analysis, simplified procedures for the Cetin et al. (2004) model have been previously derived (Mayfield et al., 2010; Franke et al., 2014b). The simplified performance-based procedure for the Boulanger and Idriss (2012) model is derived in this chapter.

6.1 **Previous Simplified Performance-Based Liquefaction Assessment Procedures**

To provide engineering practitioners with the improved objectivity and consistency of the performance-based approach without requiring complex probabilistic or iterative calculations, Mayfield et al. (2010) introduced a simplified performance-based procedure that incorporates the Cetin et al. (2004) probabilistic liquefaction triggering model. This procedure was subsequently updated and applied to the seismic design of bridges by Franke et al. (2014b).

While most engineering practitioners characterize seismic loading for a liquefaction triggering assessment using *CSR*, the simplified performance-based triggering procedures of

Mayfield et al. (2010) and Franke et al. (2014b) characterize seismic loading using the SPT resistance required to resist liquefaction initiation, N_{req}. Mayfield et al. (2010) graphically demonstrated how N_{req} is related to *CSR* through the *CRR*, as shown in Figure 6-1. With the N_{req} approach, liquefaction triggering potential is evaluated by comparing the actual SPT resistance in a given soil layer, $\left(N_1\right)_{60,cs}$ or N_{site}, against N_{req}. The difference between $\left(N_1\right)_{60,cs}$ and N_{req} can be expressed as:

$$\Delta N_L = \left(N_1\right)_{60,cs} - N_{req} \tag{6-1}$$

Therefore, a negative value of ΔN_L suggests an insufficient amount of available SPT resistance in the soil to resist liquefaction triggering.

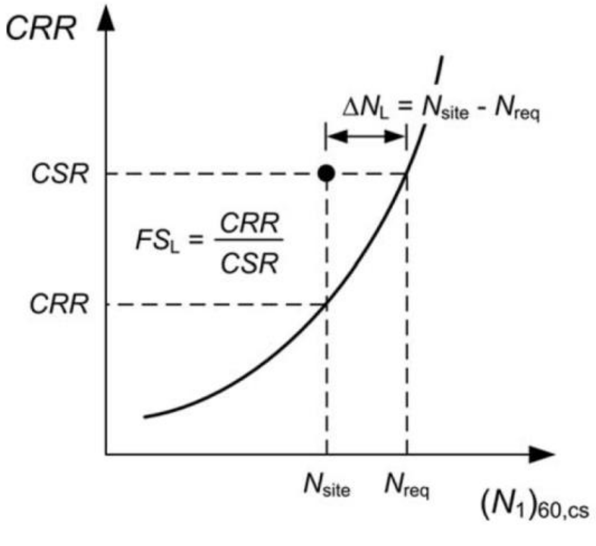

Figure 6-1: Graphical Relationship between *CSR*, *CRR*, N_{site}, N_{req}, FS_L, and ΔN_L (after Mayfield et al., 2010)

The Mayfield et al. (2010) and Franke et al. (2014b) simplified performance-based procedures use maps called *liquefaction parameter maps*, which display hazard-targeted estimates of N_{req} corresponding to a "reference" soil layer located at a depth of 6 meters below the ground surface in saturated clean sand, as depicted in Figure 6-2. These liquefaction parameter maps are created by analyzing this hypothetical reference soil layer using a full PBEE procedure at a given return period across a region at intermittent geographic coordinates. The simplified procedures provide a series of adjustment equations to correct mapped reference values of N_{req} for site-specific soil information to produce probabilistic estimates of N_{req} that closely approximate the N_{req} values that would be computed from a full performance-based liquefaction triggering procedure such as Kramer and Mayfield (2007). A sample liquefaction parameter map is provided in Figure 6-3.

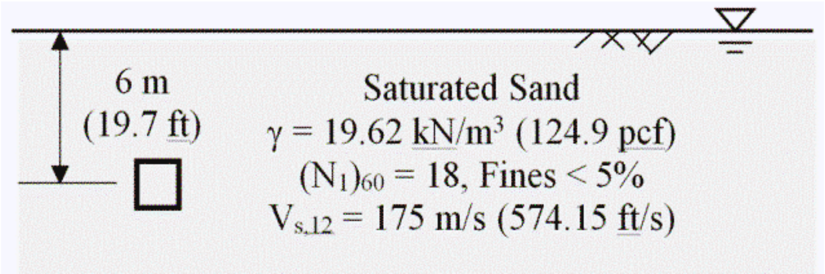

Figure 6-2: Reference Soil Layer Used to Develop Liquefaction Parameter Maps in the Mayfield et al. (2010) Simplified Uniform Hazard Liquefaction Assessment Procedure

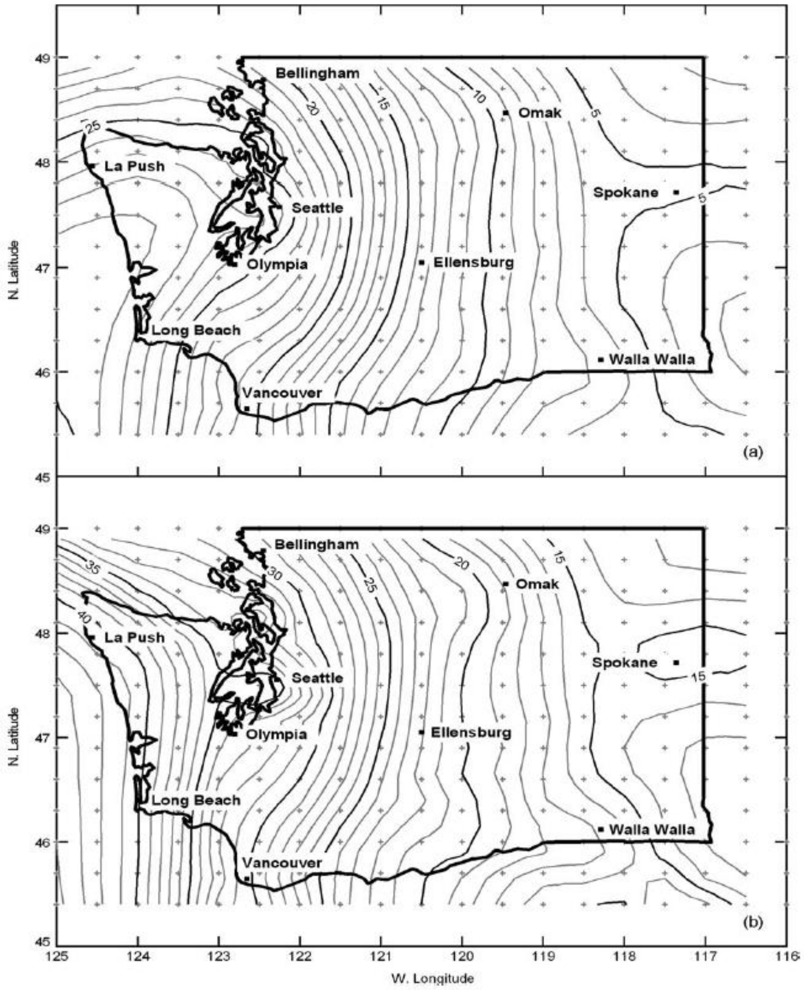

Figure 6-3: Sample Liquefaction Parameter Map of N_{req} for Washington State for Return Periods of (a) 475 Years and (b) 2,475 Years (after Mayfield et al., 2010)

6.1.1 Mayfield et al. (2010) Correction Factor

Mayfield et al. (2010) set out to solve for a correction factor, ΔN_{req} , which would convert the mapped reference value, N_{req}^{ref} to the site-specific value, N_{req}^{site}. The relationship between these parameters is defined as:

$$N_{req}^{site} = N_{req}^{ref} + \Delta N_{req} \tag{6-2}$$

Inserting the equations of N_{req}^{ref} and N_{req}^{site} would provide the equation for the needed correction factor. Using the Cetin et al. (2004) model, letting $N_{req} = N_{1,60}\left(1+\theta_1 FC\right)$ in Equation (4-8), and using the definition of *CSR_{eq}*, the correction factor ΔN_{req} was calculated as:

$$N_{req}^{ref} = 13.79\ln\left(0.65F_a^{ref}a_{\max,rock}\frac{\sigma_{v0}^{ref}}{\left(\sigma_{v0}^{'}\right)^{ref}}r_d^{ref}\right)+29.06\ln\left(M_w\right) \\ +3.82\ln\frac{\left(\sigma_{v0}^{'}\right)^{ref}}{p_a}-15.25-4.21\Phi^{-1}\left(P_L\right) \tag{6-3}$$

$$N_{req}^{site} = 13.79\ln\left(0.65F_a^{site}a_{\max,rock}\frac{\sigma_{v0}^{site}}{\left(\sigma_{v0}^{'}\right)^{site}}r_d^{site}\right)+29.06\ln\left(M_w\right) \\ +3.82\ln\frac{\left(\sigma_{v0}^{'}\right)^{site}}{p_a}-15.25-4.21\Phi^{-1}\left(P_L\right) \tag{6-4}$$

$$\Delta N_{req} = N_{req}^{site}-N_{req}^{ref} = 13.79\ln\left(\frac{\sigma_{v0}^{site}\Big/\left(\sigma_{v0}^{'}\right)^{site}}{\sigma_{v0}^{ref}\Big/\left(\sigma_{v0}^{'}\right)^{ref}}\right)+3.82\ln\frac{\left(\sigma_{v0}^{'}\right)^{site}}{\left(\sigma_{v0}^{'}\right)^{ref}} \\ +13.79\ln\frac{F_a^{site}}{F_a^{ref}}+13.79\ln\frac{r_d^{site}}{r_d^{ref}} \tag{6-5}$$

This equation for ΔN_{req} is the key to solving for hazard-targeted estimates of N_{req} at any depth at a site of interest. The values of N_{req}^{ref} would be provided through a liquefaction parameter map and the engineer would need only use Equations (6-2) and (6-5) to perform the simplified performance-based procedure.

6.2 Modified Simplified Performance-Based Procedure

While the N_{req} approach introduced by Mayfield et al. (2010) is intuitive and quantifies liquefaction triggering hazard in terms that are readily understandable to engineering practitioners (i.e., SPT resistance), some engineers are more comfortable assessing liquefaction triggering potential with a traditional approach incorporating *CSR* and *CRR*. Furthermore, the adjustment equations derived by Mayfield et al. (2010) and Franke et al. (2014b) are valid only for the Cetin et al. (2004) probabilistic liquefaction triggering model. Given the recent confusion regarding liquefaction triggering models in engineering practice, some engineers may be hesitant to apply the Mayfield et al. (2010) and/or Franke et al. (2014b) procedures due to their basis in the Cetin et al. (2004) model. To address these challenges, this section introduces a modified simplified performance-based liquefaction triggering procedure that is based on the Boulanger and Idriss (2012) probabilistic liquefaction triggering model, and that uses *CSR* rather than N_{req} to characterize seismic loading. With this new simplified procedure, engineers will be able to use site-specific soil information with newly-introduced *liquefaction loading maps* to develop probabilistic estimates of liquefaction triggering hazard at targeted return periods using the familiar liquefaction analysis parameters *CSR* and *CRR*.

As shown previously, according to the probabilistic liquefaction triggering model presented by Boulanger and Idriss (2012), the magnitude- and stress-corrected cyclic resistance ratio, $CRR_{M=7.5,\sigma_v'=1atm}$ (as a function of clean-sand equivalent SPT resistance, $\left(N_1\right)_{60,cs}$) is computed as:

$$CRR_{M=7.5,\sigma_v'=1atm}=\exp\left[\left(\frac{\left(N_1\right)_{60,cs}}{14.1}\right)+\left(\frac{\left(N_1\right)_{60,cs}}{126}\right)^2-\left(\frac{\left(N_1\right)_{60,cs}}{23.6}\right)^3+\left(\frac{\left(N_1\right)_{60,cs}}{25.4}\right)^4-2.67+\sigma_\varepsilon\cdot\Phi^{-1}\left(P_L\right)\right] \quad (6\text{-}6)$$

If P_L = 50% is used in Equation (6-6), then Equation (6-6) would represent the median cyclic resistance ratio as:

$$CRR_{M=7.5,\sigma_v'=1atm,P_L=50\%} = CRR = \exp\left[\left(\frac{(N_1)_{60,cs}}{14.1}\right)+\left(\frac{(N_1)_{60,cs}}{126}\right)^2-\left(\frac{(N_1)_{60,cs}}{23.6}\right)^3+\left(\frac{(N_1)_{60,cs}}{25.4}\right)^4-2.67\right] \quad (6\text{-}7)$$

According to Boulanger and Idriss (2012), Equation (6-6) can be manipulated to solve for P_L for a given soil layer as:

$$P_L = \Phi\left[-\frac{\left(\frac{(N_1)_{60,cs}}{14.1}\right)+\left(\frac{(N_1)_{60,cs}}{126}\right)^2-\left(\frac{(N_1)_{60,cs}}{23.6}\right)^3+\left(\frac{(N_1)_{60,cs}}{25.4}\right)^4-2.67-\ln\left(CSR_{M=7.5,\sigma_v'=1atm}\right)}{\sigma_\varepsilon}\right] \quad (6\text{-}8)$$

where $CSR_{M=7.5,\sigma_v'=1atm}$ is the cyclic stress ratio corresponding to an equivalent M_w = 7.5 earthquake under an effective confining stress of 1 atmosphere. As discussed previously, Idriss and Boulanger (2008) defined $CSR_{M=7.5,\sigma_v'=1atm}$ as:

$$CSR_{M=7.5,\sigma_v'=1atm} = 0.65\frac{\sigma_v}{\sigma_v'}\frac{a_{\max}}{g}r_d\frac{1}{MSF}\frac{1}{K_\sigma} = 0.65\frac{\sigma_v}{\sigma_v'}\frac{\left(F_{pga}\cdot PGA_{rock}\right)}{g}r_d\frac{1}{MSF}\frac{1}{K_\sigma} \quad (6\text{-}9)$$

where F_{pga} is a soil amplification factor to correct for local site response effects; and PGA_{rock} is the peak ground acceleration (in units of gravity, *g*) corresponding to bedrock with an average shear wave velocity equal to 760 meters/second in its upper 30 meters of depth (i.e., $V_{s,30} = 760$ m/sec).

As discussed previously, Franke and Wright (2013) incorporated the Boulanger and Idriss (2012) probabilistic triggering model in the Kramer and Mayfield (2007) PBEE approach to calculate the hazard curve for FS_L for a given soil layer. Franke et al. (2014c,) later added to the

Franke and Wright (2013) FS_L approach with equations that calculate the hazard curve for N_{req} for a given soil layer. With this approach, Franke et al. computed the mean annual rate of exceedance for some assumed required SPT resistance in a soil layer, $\lambda_{N^*_{req}}$ as:

$$\lambda_{N^*_{req}} = \sum_{j=1}^{N_M} \sum_{i=1}^{N_{a_{\max}}} P\left[N_{req} > N^*_{req} \mid a_{\max,i}, m_j\right] \Delta\lambda_{a_{\max,i}, m_j} \tag{6-10}$$

where

$$P\left[N_{req} > N^*_{req} \mid a_{\max,i}, m_j\right] = \Phi\left[-\frac{\frac{N^*_{req}}{14.1} + \left(\frac{N^*_{req}}{126}\right)^2 - \left(\frac{N^*_{req}}{23.6}\right)^3 + \left(\frac{N^*_{req}}{25.4}\right)^4 - 2.67 - \ln CSR_{i,j}}{\sigma_\varepsilon}\right] \tag{6-11}$$

and where N_M and $N_{a_{\max}}$ represent the number of magnitude and peak ground surface acceleration increments, respectively; $\Delta\lambda_{a_{\max,i}, m_j}$ is the joint incremental mean annual rate of exceedance for peak ground surface acceleration, $a_{\max,i}$ and magnitude, m_j (computed directly from the joint probability “bins” from a ground motion deaggregation analysis); and $CSR_{i,j}$ is computed with Equation (6-9), and σ_ε is either 0.13 for model uncertainty alone or 0.277 for total (i.e., model + parametric) uncertainty. N_{req} hazard curves can be computed by engineers for a given soil layer using computational tools that incorporate Equation (6-10) such as *WSliq* (Huang 2008; Kramer 2008) or *PBLiquefY* (Wright 2013; Franke et al. 2014d).

6.2.1 Liquefaction Loading Maps

Mayfield et al. (2010) utilized the full performance-based relationship for N_{req} (i.e., Equation (6-10)) with the Cetin et al. (2004) model to develop a hazard-targeted liquefaction parameter map for their defined reference soil layer (i.e., Figure 6-2). Mayfield et al. then manipulated the *CRR* relationship from the Cetin et al. (2004) model to derive adjustment equations to correct reference N_{req} values from the liquefaction parameter map for site-specific soil conditions. The derivation of these adjustment equations required the isolation of the SPT resistance term in the Cetin et al. (2004) *CRR* relationship. Unfortunately, isolation of the SPT resistance in the Boulanger and Idriss (2012) *CRR* relationship presented in Equation (6-6) is computationally difficult due to the polynomial nature of the equation. However, derivation of a simplified performance-based procedure is possible if the Mayfield et al. (2010) approach is modified so as to characterize seismic loading in a different manner.

As demonstrated in Figure 6-1, *CSR* is a function of *CRR* and N_{req} such that:

$$CSR_{M=7.5,\sigma_v'=1atm} = CRR\left(N_{req}\right) \tag{6-12}$$

Subsequently, Equations (6-7) and (6-12) can be combined to compute the median, magnitude- and stress-corrected cyclic shear stress, $CSR_{M=7.5,\sigma_v'=1atm}$ for the Boulanger and Idriss (2012) probabilistic triggering model as:

$$CSR_{m=7.5,\sigma_v'=1atm} = CSR = CRR\left(N_{req}\right) = \exp\left[\left(\frac{N_{req}}{14.1}\right)+\left(\frac{N_{req}}{126}\right)^2-\left(\frac{N_{req}}{23.6}\right)^3+\left(\frac{N_{req}}{25.4}\right)^4-2.67\right] \tag{6-13}$$

Equation (6-13) suggests the possibility of using N_{req} hazard curves developed from Equation (6-10) for a given soil profile to compute corresponding hazard curves for CSR. This process of computing CSR hazard curves is schematically presented in Figure 6-4. Using this approach, CSR hazard curves could be developed by researchers for the reference soil layer shown in Figure 6-2 across a grid of geographic points. By selecting a targeted return period or hazard level, uniform-hazard values of CSR could be obtained from these reference hazard curves and plotted to produce contour maps of reference CSR values, or CSR^{ref}. Because these maps contour CSR^{ref} instead of N_{req}, they are referred to as *liquefaction loading maps*. Furthermore, because CSR^{ref} is typically a decimal value less than unity, mapping the percent of CSR^{ref} (i.e., $CSR^{ref}(\%)$) allows for more precise contours, as well as easier interpretation and interpolation for design engineers. Figure 6-5 presents liquefaction loading maps of $CSR^{ref}(\%)$ at return periods of 475 years and 2,475 years for downtown Salt Lake City, Utah.

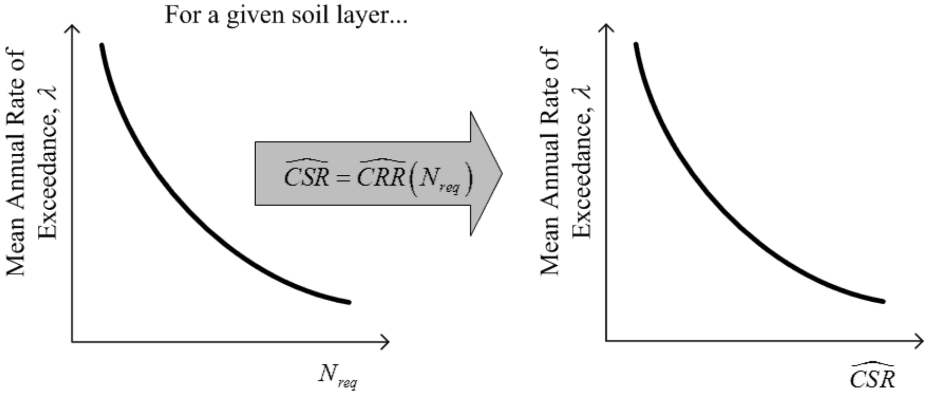

Figure 6-4: Demonstration of the Transformation of the N_{req} Hazard Curve to the $\widehat{CSR}$ Hazard Curve for a Given Soil Layer Using the $\widehat{CRR}$ Function

Liquefaction loading maps like the ones presented in Figure 6-5 can be used to rapidly assess the relative level of liquefaction seismic loading in a given geographic area. For example, higher $CSR^{ref}(\%)$ values indicate higher levels of seismic loading for liquefaction initiation. Higher $CSR^{ref}(\%)$ values also indicate that soils in that area require higher relative densities to prevent liquefaction initiation. While these qualitative assessments may be useful to some extent, engineers must remember that mapped values of $CSR^{ref}(\%)$ do not represent the actual values of

$CSR_{M=7.5,\sigma_v'=1atm}$ to be used in a liquefaction triggering assessment because they have not yet been corrected for site-specific soil conditions, a process that will be subsequently described.

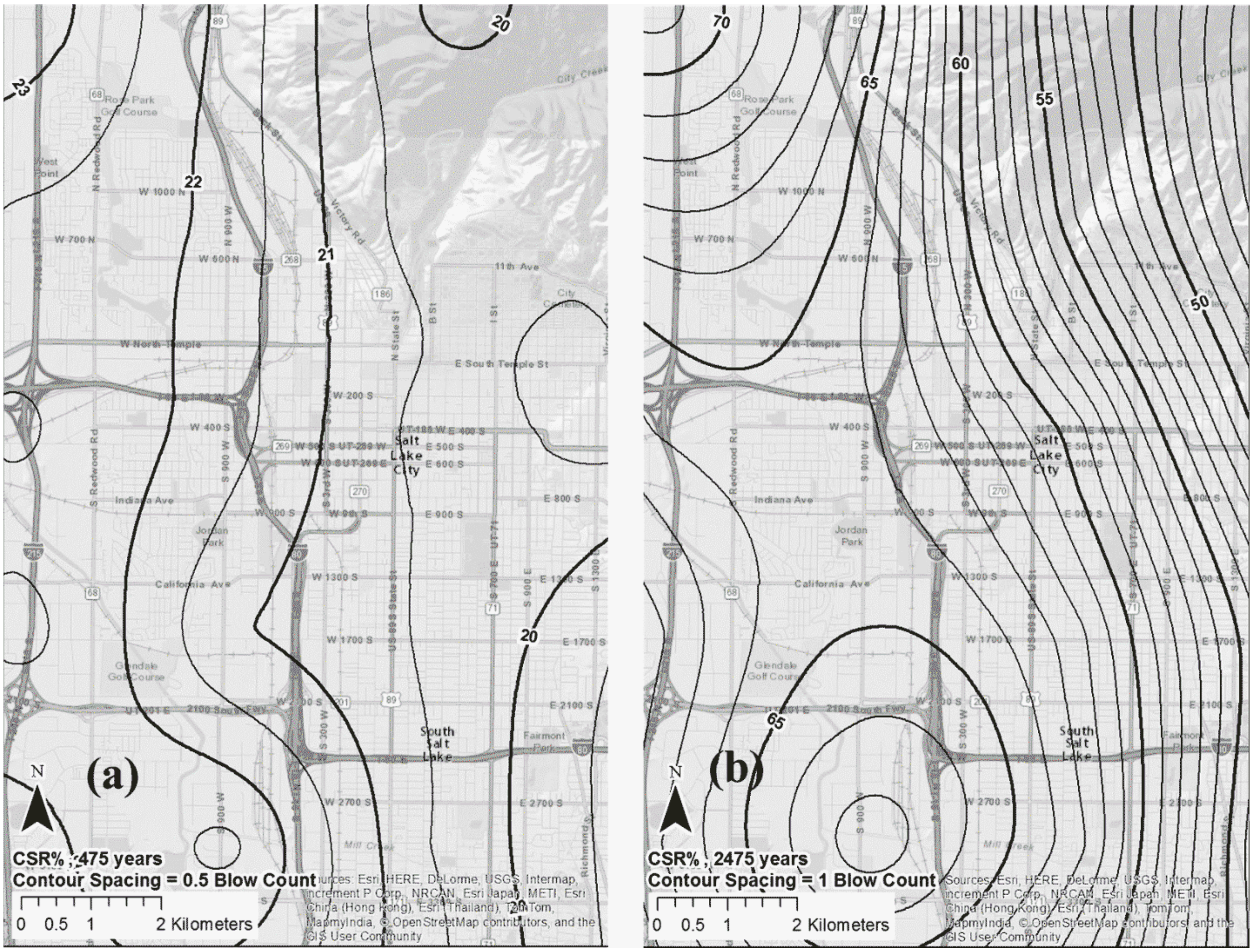

Figure 6-5: Liquefaction Loading Map Showing Contours of CSR^{ref} (%) for Salt Lake City, Utah at Return Periods of (a) 475 years and (b) 2,475 years

6.2.2 Adjustment Equations for Site-Specific Application

Because liquefaction loading maps correspond to the reference soil layer shown in Figure 6-2, mapped values of CSR^{ref} (%) must be corrected for site-specific soil conditions before they can be used to compute site-specific probabilistic estimates of liquefaction triggering potential. This triggering potential can be expressed as P_L; FS_L; and/or ΔN_L. The relationship between the site-specific value of $CSR_{M=7.5,\sigma_v'=1atm}$ and the mapped, reference value of CSR^{ref} (%) is expressed as:

$$\ln\left(CSR_{M=7.5,\sigma_v'=1atm}\right)=\ln\left(\frac{CSR^{ref}\,(\%)}{100}\right)+\Delta CSR \tag{6-14}$$

where ΔCSR is the *seismic loading adjustment factor*. Rearranging Equation (6-14), ΔCSR can be solved as:

$$\Delta CSR=\ln\left(CSR_{M=7.5,\sigma_v'=1atm}\right)-\ln\left(\frac{CSR^{ref}\,(\%)}{100}\right)=\ln\left(\frac{100\cdot CSR_{M=7.5,\sigma_v'=1atm}}{CSR^{ref}\,(\%)}\right) \tag{6-15}$$

If Equation (6-9) is substituted into Equation (6-15), then Equation (6-15) can be rewritten as:

$$\Delta CSR=\ln\left[\frac{0.65\left(\dfrac{\sigma_v}{\sigma_v'}\right)^{site}\left(\dfrac{F_{pga}^{site}\cdot PGA_{rock}^{site}}{g}\right)\cdot r_d^{site}\cdot\left(\dfrac{1}{MSF^{site}}\right)\cdot\left(\dfrac{1}{K_\sigma^{site}}\right)}{0.65\left(\dfrac{\sigma_v}{\sigma_v'}\right)^{ref}\left(\dfrac{F_{pga}^{ref}\cdot PGA_{rock}^{ref}}{g}\right)\cdot r_d^{ref}\cdot\left(\dfrac{1}{MSF^{ref}}\right)\cdot\left(\dfrac{1}{K_\sigma^{ref}}\right)}\right] \tag{6-16}$$

where the superscript '*site*' implies that the values are computed using site-specific soil information, and the superscript '*ref*'' implies that the values are computed using the reference soil profile shown in Figure 6-2.

There should be no difference in the bedrock ground motions between the reference soil profile and the actual soil profile at a given location, so it follows that $PGA_{rock}^{site}=PGA_{rock}^{ref}$. Therefore, Equation (6-16) can be simplified as:

$$\Delta CSR = \ln\left(\frac{\left(\sigma_v / \sigma_v'\right)^{site}}{\left(\sigma_v / \sigma_v'\right)^{ref}}\right) + \ln\left(\frac{F_{pga}^{site}}{F_{pga}^{ref}}\right) + \ln\left(\frac{r_d^{site}}{r_d^{ref}}\right) - \ln\left(\frac{MSF^{site}}{MSF^{ref}}\right) - \ln\left(\frac{K_\sigma^{site}}{K_\sigma^{ref}}\right)$$

$$= \Delta CSR_\sigma + \Delta CSR_{F_{pga}} + \Delta CSR_{r_d} + \Delta CSR_{MSF} + \Delta CSR_{K_\sigma} \tag{6-17}$$

where ΔCSR_σ, $\Delta CSR_{F_{pga}}$, ΔCSR_{r_d}, ΔCSR_{MSF}, and ΔCSR_{K_σ} are adjustment factors corresponding to soil stress, soil amplification, shear stress reduction, earthquake magnitude, and overburden pressure, respectively.

6.2.2.1 Adjustment for Soil Stress, ΔCSR_σ

The relationship for the stress adjustment factor, ΔCSR_σ is defined as:

$$\Delta CSR_\sigma = \ln\left[\frac{\left(\sigma_v / \sigma_v'\right)^{site}}{\left(\sigma_v / \sigma_v'\right)^{ref}}\right] \tag{6-18}$$

If the liquefaction loading map for $CSR^{ref}(\%)$ was developed using the reference soil profile shown in Figure 6-2, then Equation (6-18) can be simplified as:

$$\Delta CSR_\sigma = \ln\left[\frac{\left(\sigma_v / \sigma_v'\right)^{site}}{2}\right] \tag{6-19}$$

Mayfield et al. (2010) used weight-volume relationships to investigate the possibility of simplifying the stress adjustment factor in their simplified procedure based on the Cetin et al.

(2004) model. By substituting specific gravity and void ratio for the vertical stress terms, and then by assuming that the site-specific void ratio and specific gravity were relatively close to those used in the reference soil profile, Mayfield et al. developed a simplified equation for their stress adjustment factor that was simply a function of depth and depth to groundwater. Mayfield et al. demonstrated that this simplified equation was quite insensitive to changes in void ratio, and thus introduced relatively little error into their computed results. A similar investigation was performed with ΔCSR_{σ} in this study to evaluate the possibility of developing a simplified relationship for Equation (6-19). However, it was observed that the natural logarithm function associated with the seismic loading adjustment factor (i.e., Equation (6-15)) causes ΔCSR to be very sensitive to even small bias. Therefore, no further simplifications of Equation (6-19) were pursued.

6.2.2.2 Adjustment for Soil Amplification, $\Delta CSR_{F_{pga}}$

The relationship for the soil amplification adjustment factor, $\Delta CSR_{F_{pga}}$ is given as:

$$\Delta CSR_{F_{pga}} = \ln\left(\frac{F_{pga}^{site}}{F_{pga}^{ref}}\right) \tag{6-20}$$

If a liquefaction loading map is developed using "bedrock" ground motions (i.e., $a_{\max} = PGA_{rock}$) then F_{pga}^{ref} is fixed at a value of 1.0 for all sites. With this assumption, the adjustment factor for soil amplification is simplified as:

$$\Delta CSR_{F_{pga}} = \ln\left(\frac{F_{pga}^{site}}{1}\right) = \ln\left(F_{pga}^{site}\right) \tag{6-21}$$

The site-specific soil amplification factor, F_{pga}^{site}, can be estimated using multiple methods. Kramer and Mayfield (2007) used the empirical site amplification model of Stewart et al. (2003)

in their performance-based procedure. Complex projects may justify the effort and expense of computing F_{pga}^{site} using site response analysis. However, most engineering practitioners will likely use codified site amplification factors based on PGA_{rock} and soil site classification to estimate F_{pga}^{site}. Common soil amplification factors specified by ASCE (2013), IBC (2014), and AASHTO (2014) are summarized in Table 6-1.

Table 6-1: Values of Site Amplification Factor, F_{pga}^{site}, Corresponding to Several Modern Seismic Design Codes (Values Taken from ASCE 2013; IBC 2014; AASHTO 2014)

Site Class	Site Amplification Factor, F_{pga}				
	PGA(g)<0.10	PGA(g)=0.20	PGA(g)=0.30	PGA(g)=0.40	PGA(g)>0.50
A	0.8	0.8	0.8	0.8	0.8
B	1.0	1.0	1.0	1.0	1.0
C	1.2	1.2	1.1	1.0	1.0
D	1.6	1.4	1.2	1.1	1.0
E	2.5	1.7	1.2	0.9	0.9
F	Site Response Analysis Required				

6.2.2.3 *Adjustment for Shear Stress Reduction*, ΔCSR_{r_d}

The shear stress reduction factor, r_d, was defined by Idriss and Boulanger (2008) as:

$$r_d = \exp\left[\alpha + \beta \cdot M_w\right] \tag{6-22}$$

$$\alpha = -1.012 - 1.126\sin\left(\frac{z}{11.73} + 5.133\right) \tag{6-23}$$

$$\beta = 0.106 + 0.118\sin\left(\frac{z}{11.28} + 5.142\right) \tag{6-24}$$

where *z* represents sample depth from the ground surface in meters. Accounting for site-specific and reference soil conditions, the relationship for ΔCSR_{r_d} becomes:

$$\Delta CSR_{r_d} = \ln\left(\frac{r_d^{site}}{r_d^{ref}}\right) = \ln\left(\frac{\exp\left(\alpha^{site} + \beta^{site} \cdot M_w^{site}\right)}{\exp\left(\alpha^{ref} + \beta^{ref} \cdot M_w^{ref}\right)}\right) \tag{6-25}$$

Because ground motions are the same for both reference and actual soil profiles, $M_w^{site} = M_w^{ref}$. Therefore, Equation (6-25) can be simplified as:

$$\Delta CSR_{r_d} = \left(\alpha^{site} - \alpha^{ref}\right) + M_w^{site}\left(\beta^{site} - \beta^{ref}\right) \tag{6-26}$$

Mayfield et al. (2010) demonstrated that the r_d term in the Cetin et al. (2004) model is relatively insensitive to the value of M_w for a particular range of values (M_w = 5.97 to 7.70). This observation allowed the correction factor for r_d in the Mayfield et al. simplified procedure to assume a uniform M_w value of 6.5 for all analyses without introducing significant bias into the results. In this study, the r_d value from the Idriss and Boulanger (2008) model was found to be quite sensitive to M_w. This sensitivity is demonstrated in Figure 6-6, which illustrates the variability of r_d with depth (0 to 25m) and M_w (5.5 to 8.0). Due to the wide range of computed r_d values for different M_w, M_w^{site} cannot be removed from Equation (6-26).

For the reference soil profile used in this study (Figure 6-2), $\alpha^{ref} = -0.3408$ and $\beta^{ref} = 0.0385$. Thus, Equation (6-26) is simplified as:

$$\Delta CSR_{r_d} = \left(\alpha^{site} + 0.3408\right) + M_w^{site}\left(\beta^{site} - 0.0385\right) \tag{6-27}$$

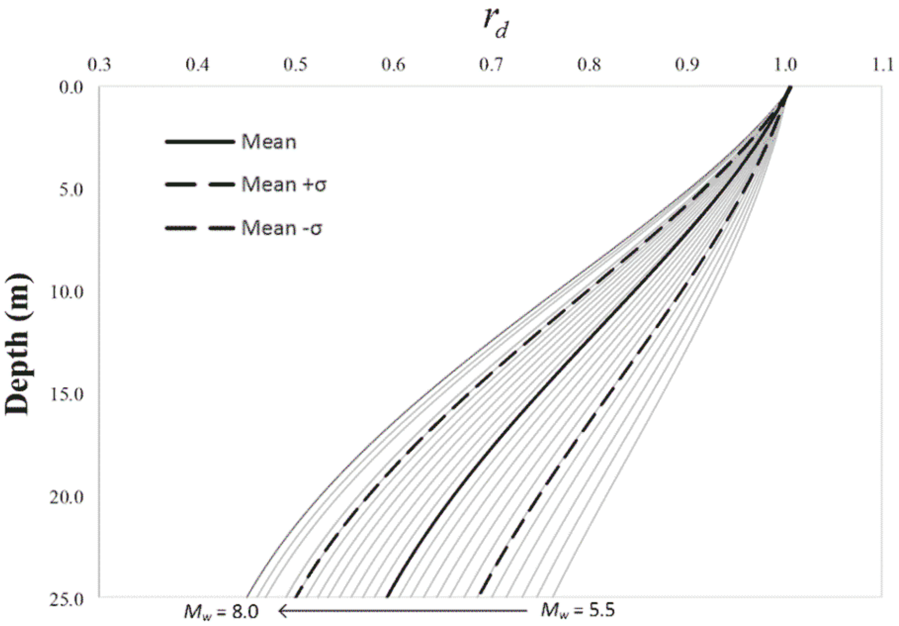

Figure 6-6: Shear Stress Reduction Factor (r_d) vs. Depth for a Range of M_w Values (5.5 to 8.0) According to the Idriss and Boulanger (2008) Model

Equation (6-27) can also be written in terms of depth to the site-specific soil sublayer (in meters) from the ground surface, z^{site} as:

$$\Delta CSR_{r_d} = \left(-0.6712 - 1.126 \sin\left(\frac{z^{site}}{11.73} + 5.133 \right) \right) + M_w^{site} \left(0.0675 + 0.118 \sin\left(\frac{z^{site}}{11.28} + 5.142 \right) \right) \tag{6-28}$$

For this simplified procedure, the value of M_w^{site} should be taken as the *mean* moment magnitude from the probabilistic deaggregation of PGA_{rock} at the targeted return period.

6.2.2.4 Adjustment for Magnitude Scaling Factor, ΔCSR_{MSF}

The adjustment factor for the *MSF* is computed as:

$$\Delta CSR_{MSF} = -\ln\left[\frac{MSF^{site}}{MSF^{ref}}\right] \tag{6-29}$$

According to Idriss and Boulanger (2008) and Boulanger and Idriss (2012), the *MSF* is a simple function of M_w. Because $M_w^{site} = M_w^{ref}$, then $MSF^{site} = MSF^{ref}$ and ΔCSR_{MSF} = 0. Therefore, ΔCSR_{MSF} can be neglected in Equation (6-17).

Boulanger and Idriss (2014) recently proposed an update to their relationship for MSF in which the effect of soil characteristics including relative density (as a function of $(N_1)_{60,cs}$) is accounted for in estimating *MSF*. Because $(N_1)_{60,cs}$ generally varies between soil layers, $MSF^{site} \neq MSF^{ref}$. If the Boulanger and Idriss (2014) relationship for the *MSF* is used in developing a given liquefaction loading map, then Equation (6-29) can be modified as:

$$\Delta CSR_{MSF} = -\ln\left(\frac{1+\left(MIN\left\{\begin{matrix}2.2\\ 1.09+\left(\dfrac{(N_1)_{60,cs}^{site}}{31.5}\right)^2\end{matrix}\right\}-1\right)\left(8.64\exp\left(\dfrac{-M_w^{site}}{4}\right)-1.325\right)}{1+\left(MIN\left\{\begin{matrix}2.2\\ 1.09+\left(\dfrac{(N_1)_{60,cs}^{ref}}{31.5}\right)^2\end{matrix}\right\}-1\right)\left(8.64\exp\left(\dfrac{-M_w^{site}}{4}\right)-1.325\right)}\right) \tag{6-30}$$

where $(N_1)_{60,cs}^{ref} = 18$ blows per 0.3 meter, as shown in Figure 6-2.

Simplifying Equation (6-30) gives:

$$\Delta CSR_{MSF} = -\ln\left[\frac{1+MIN\left\{\begin{matrix}\left(\dfrac{(N_1)_{60,cs}^{site}}{31.5}\right)^2+0.09\\1.2\end{matrix}\right\}\cdot\left(8.64\exp\left(\dfrac{-M_w^{site}}{4}\right)-1.325\right)}{3.603\exp\left(\dfrac{-M_w^{site}}{4}\right)+0.447}\right] \tag{6-31}$$

6.2.2.5 Adjustment for Overburden Pressure, ΔCSR_{K_σ}

The adjustment factor for the overburden pressure is given as:

$$\Delta CSR_{K_\sigma} = -\ln\left(\frac{K_\sigma^{site}}{K_\sigma^{ref}}\right) \tag{6-32}$$

According to Idriss and Boulanger (2008), K_σ can be estimated for a given soil layer as:

$$K_\sigma = 1 - C_\sigma \ln\left(\frac{\sigma'_v}{P_a}\right) \le 1.1 \tag{6-33}$$

$$C_\sigma = \frac{1}{18.9-2.55\sqrt{(N_1)_{60,cs}}} \le 0.3 \tag{6-34}$$

where P_a is atmospheric pressure in units consistent with σ_v'. Idriss and Boulanger (2010) commented that the K_σ limit of 1.1 has a somewhat negligible effect, and can therefore be omitted if an engineer desires. Omitting this limitation and substituting Equations (6-33) and (6-34) into Equation (6-32), the overburden correction equation can be expressed as:

$$\Delta CSR_{K_\sigma} = -\ln\left(\frac{1 - C_\sigma^{site}\ln\left(\frac{\left(\sigma'_v\right)^{site}}{P_a}\right)}{1 - C_\sigma^{ref}\ln\left(\frac{\left(\sigma'_v\right)^{ref}}{P_a}\right)}\right) \tag{6-35}$$

If a liquefaction loading map for $CSR^{ref}\left(\%\right)$ was developed using the reference soil profile shown in Figure 6-2, then Equation (6-35) can be simplified as:

$$\left(\Delta CSR_{K_\sigma}\right)_i = -\ln\left(\frac{1 - MIN\left\{\begin{matrix} 0.3 \\ \dfrac{1}{18.9 - 2.55\sqrt{\left[\left(N_1\right)_{60,cs}^{site}\right]_i}} \end{matrix}\right\}\cdot\ln\left(\frac{\left(\sigma'_v\right)_i^{site}}{P_a}\right)}{1.067}\right) \tag{6-36}$$

6.2.2.6 *Assessing Liquefaction Triggering Potential with* $CSR_{M=7.5,\sigma_v'=1atm}$

Once the value of $CSR^{ref}\left(\%\right)$ is obtained from the appropriate liquefaction loading map, and the adjustment factors ΔCSR_σ, $\Delta CSR_{F_{pga}}$, ΔCSR_{r_d}, ΔCSR_{MSF}, and ΔCSR_{K_σ} are computed for each sublayer in a given soil profile , then the site-specific, hazard-targeted $CSR_{M=7.5,\sigma_v'=1atm}$ can be computed for site-specific soil sublayer *i* as:

$$\left(CSR_{M=7.5,\sigma_v'=1atm}\right)_i = \exp\left[\begin{matrix}\ln\left(\dfrac{CSR^{ref}(\%)}{100}\right) + \left(\Delta CSR_\sigma\right)_i + \left(\Delta CSR_{F_{pga}}\right)_i + \left(\Delta CSR_{r_d}\right)_i \\ + \left(\Delta CSR_{MSF}\right)_i + \left(\Delta CSR_{K_\sigma}\right)_i\end{matrix}\right] \tag{6-37}$$

Thus $\left(CSR_{M=7.5,\sigma_v'=1atm}\right)_i$ can be used to compute hazard-targeted estimates of liquefaction triggering potential for soil sublayer *i* in terms of P_L; FS_L; and/or ΔN_L using relationships already familiar to engineers. For example, FS_L for soil sublayer *i* can be computed as:

$$\left(FS_L\right)_i = \frac{\left(CRR\right)_i}{\left(CSR_{M=7.5,\sigma_v'=1atm}\right)_i} = \frac{\exp\left[\left(\frac{\left[\left(N_1\right)_{60,cs}\right]_i}{14.1}\right)+\left(\frac{\left[\left(N_1\right)_{60,cs}\right]_i}{126}\right)^2-\left(\frac{\left[\left(N_1\right)_{60,cs}\right]_i}{23.6}\right)^3+\left(\frac{\left[\left(N_1\right)_{60,cs}\right]_i}{25.4}\right)^4-2.67\right]}{\left(CSR_{M=7.5,\sigma_v'=1atm}\right)_i} \tag{6-38}$$

Similarly, P_L for soil sublayer *i* can be computed as:

$$P_L = \Phi\left[-\frac{\left(\frac{\left[\left(N_1\right)_{60,cs}\right]_i}{14.1}\right)+\left(\frac{\left[\left(N_1\right)_{60,cs}\right]_i}{126}\right)^2-\left(\frac{\left[\left(N_1\right)_{60,cs}\right]_i}{23.6}\right)^3+\left(\frac{\left[\left(N_1\right)_{60,cs}\right]_i}{25.4}\right)^4-2.67-\ln\left[\left(CSR_{M=7.5,\sigma_v'=1atm}\right)_i\right]}{\sigma_\varepsilon}\right] \tag{6-39}$$

where $\sigma_\varepsilon = 0.13$ if the liquefaction loading map was developed assuming model uncertainty only, or $\sigma_\varepsilon = 0.277$ if the liquefaction loading map was developed assuming both parametric and model uncertainty.

Finally, ΔN_L (Mayfield et al. 2010) for soil sublayer *i* can be computed as:

$$\left(\Delta N_L\right)_i = \left[\left(N_1\right)_{60,cs}\right]_i - \left(N_{req}^{site}\right)_i \tag{6-40}$$

where $\left(N_{req}^{site}\right)_i$ can be closely approximated from $\left(CSR_{M=7.5,\sigma_v'=1atm}\right)_i$ ($R^2 = 0.999$) as:

$$\begin{aligned}\left(N_{req}^{site}\right)_i = {} & 1.237\cdot\left(\ln\left(\frac{1}{\left(CSR_{M=7.5,\sigma_v'=1atm}\right)_i}\right)\right)^4 - 4.9183\cdot\left(\ln\left(\frac{1}{\left(CSR_{M=7.5,\sigma_v'=1atm}\right)_i}\right)\right)^3 \\ & +1.7624\cdot\left(\ln\left(\frac{1}{\left(CSR_{M=7.5,\sigma_v'=1atm}\right)_i}\right)\right)^2 - 5.4733\cdot\left(\ln\left(\frac{1}{\left(CSR_{M=7.5,\sigma_v'=1atm}\right)_i}\right)\right) + 33.65\end{aligned} \tag{6-41}$$

Equation (6-41) is valid for $0.07 \leq \left(CSR_{M=7.5,\sigma_v'=1atm}\right)_i \leq 1.26$. If the value of $\left(CSR_{M=7.5,\sigma_v'=1atm}\right)_i$ is outside this recommended range, then the value of $\left(N_{req}^{site}\right)_i$ must be solved iteratively using Equation (6-13).

6.3 **Chapter Summary**

This chapter reviews previously developed simplified procedures for performance-based liquefaction initiation evaluation (Mayfield et al., 2010 and Franke et al., 2014b). Unfortunately, these simplified procedures are limited to the Cetin et al. (2004) liquefaction initiation model alone. Engineers who would prefer to use the Boulanger and Idriss (2012) model do not currently have a simplified performance-based method to use. The remainder of this chapter is devoted to deriving a simplified performance-based method that uses the Boulanger and Idriss (2012) model as its liquefaction triggering curve instead of the Cetin et al. (2004) model. This simplified procedure requires a contour map of CSR^{ref} (%) values and a set of correction equations to adjust the mapped CSR^{ref} (%) value to site-specific soil conditions. This procedure produces site-specific, hazard-targeted values of $CSR_{M=7.5,\sigma_v'=1atm}$, P_L, FS_L, and/or ΔN_L for each susceptible layer in the soil profile.

7. ANALYSIS AND RESULTS

Though the previous chapter showed that it is possible to derive a simplified performance-based procedure for the Boulanger and Idriss (2012) liquefaction triggering model, the method is not applicable in practice until it has been validated and further developed. This chapter shows the results of a validation study for the simplified performance-based method derived in the previous chapter. As discussed previously, the simplified procedure must use liquefaction loading maps. This chapter also describes the development of these liquefaction loading maps for six states. Further discussion on the application of the simplified procedure is also included.

7.1 Validation of Simplified Performance-based Procedure

Ten cities across the continental United States were selected for the validation study. These cities were the same cities used to validate the Mayfield et al. (2010) simplified procedure (which uses the Cetin et al. (2004) liquefaction model). Each city's PGA (used to calculate F_{PGA}) and mean M_w for three return periods (475, 1039, and 2475) were retrieved from the 2008 USGS interactive deaggregation website and summarized in Table 7-1. Note that the 2008 USGS website does not include data for T_R = 1033 years, therefore the M_w and the F_{PGA} corresponding to T_R = 1039 years must be used when estimating N_{req}^{site} and $CSR^{site}(\%)$ for T_R = 1033 years. The values of $CSR^{ref}(\%)$ for these 10 cities are provided in Table 7-2.

Table 7-1: Ten Cities Selected for Validation Study (Data from 2008 USGS Interactive Deaggregations Website, F_{PGA} Calculated using AASHTO 2012 Table 3.10.3.2-1)

			T_R = 1039			T_R = 475			T_R = 2475		
Location	**Latitude**	**Longitude**	**Mean M_w**	***PGA***	F_{PGA}	**Mean M_w**	***PGA***	F_{PGA}	**Mean M_w**	***PGA***	F_{PGA}
Butte	46.003	-112.533	6.03	0.1206	1.559	6.03	0.0834	1.600	6.05	0.1785	1.443
Charleston	32.776	-79.931	6.87	0.3680	1.132	6.61	0.1513	1.497	7.00	0.7287	1.000
Eureka	40.802	-124.162	7.40	0.9662	1.000	7.33	0.6154	1.000	7.45	1.4004	1.000
Memphis	35.149	-90.048	7.19	0.3346	1.165	6.98	0.1604	1.479	7.24	0.5711	1.000
Portland	45.523	-122.675	7.29	0.2980	1.204	7.24	0.1990	1.402	7.31	0.4366	1.063
Salt Lake City	40.755	-111.898	6.84	0.4030	1.097	6.75	0.2126	1.375	6.90	0.6717	1.000
San Francisco	37.775	-122.418	7.38	0.5685	1.000	7.31	0.4394	1.061	7.44	0.7254	1.000
San Jose	37.339	-121.893	6.67	0.5627	1.000	6.66	0.4560	1.044	6.66	0.6911	1.000
Santa Monica	34.015	-118.492	6.79	0.5372	1.000	6.74	0.3852	1.115	6.84	0.7415	1.000
Seattle	47.530	-122.300	6.82	0.4444	1.056	6.75	0.3110	1.189	6.88	0.6432	1.000

Table 7-2: Mapped Values of CSR^{ref} (%) for the 10 Cities in the Validation Study

	T_R = 1033	T_R = 475	T_R = 2475
Location	CSR^{ref} (%)	CSR^{ref} (%)	CSR^{ref} (%)
Butte	10.370	7.434	14.671
Charleston	33.460	12.750	66.794
Eureka	109.640	67.819	162.159
Memphis	34.730	14.811	61.245
Portland	37.080	23.485	55.225
Salt Lake City	38.090	20.724	62.332
San Francisco	68.490	50.860	90.113
San Jose	57.890	45.322	72.345
Santa Monica	52.700	37.984	71.788
Seattle	47.290	32.213	67.879

To calculate the site-specific $CSR^{site}(\%)$, an assumed soil profile was applied at each site. The parameters associated with this soil profile are presented in Figure 7-1. This site profile was chosen because it is similar to the profile used by Mayfield et al. (2010) to validate their simplified procedure.

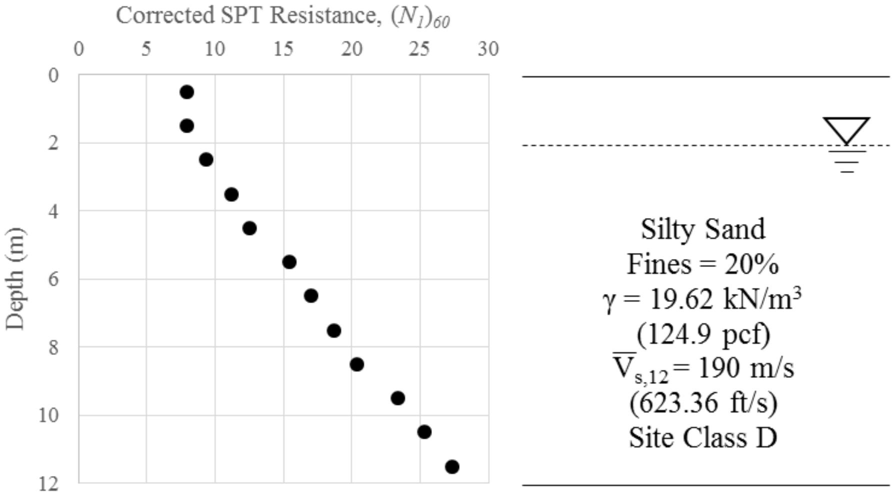

Figure 7-1 Site-Specific Soil Profile Used to Validate the Simplified Performance-Based Model

Using liquefaction loading maps (created using *PBLiquefY*) and the soil profile selected for the site specific analysis, the value of $CSR^{site}(\%)$ was determined for each layer of the site-specific soil profile and for each site using the simplified performance-based method. These $CSR^{site}(\%)$ values were converted to N_{req}^{site}, FS_L^{site}, and P_L values using Equation (6-41), Equation (6-38), and Equation (6-39), respectively.

The same soil profile shown in Figure 7-1 was analyzed at the same 10 cities using the full performance-based procedure. The necessary calculations were executed using *PBLiquefY*, which uses Equations (6-10) and (6-11) to develop a hazard curve that provides values of N_{req} for any return period. These N_{req} values were also converted to CSR, FS_L, and P_L for comparison with the simplified procedure.

The $CSR^{site}(\%)$, ΔN_L, FS_L^{site}, and P_L values from the simplified method for $T_R = 1{,}033$ years are displayed in Figure 7-2 along with the $CSR^{site}(\%)$, ΔN_L, FS_L^{site}, and P_L values computed using the full performance-based method. Also included in this plot is $(N_1)_{60,cs}^{site}$ with depth, which is the in-situ clean sand-equivalent SPT resistance of the site soil profile. Similar profiles were developed and analyzed at return periods of 475 and 2,475 years (tabulated data for all three return periods are provided in the Appendix as A-1 and A-2). The full performance-based and simplified performance-based methods yielded almost identical results for each city analyzed. When collectively considering all return periods and all cities, the average observed differences between the full and performance-based procedures were 0.027 for $CSR_{M=7.5,\sigma_v'=1atm}$, 0.041 for FS_L, 0.020 for P_L, and 0.377 for ΔN_L. The maximum differences observed between the full and simplified performance-based procedures were 0.101 for $CSR_{M=7.5,\sigma_v'=1atm}$, 0.506 for FS_L, 0.225 for P_L, and 1.91 for ΔN_L.

All computed liquefaction triggering results from the simplified and full performance-based procedures are presented together in comparative scatter plots shown in Figure 7-3. Each point on this plot represents a single layer in the site soil profile located in one city for one return period (for a total of 300 points per plot). Figure 7-3 demonstrates that the results from the simplified performance-based liquefaction triggering procedure generally approximate the results from the full performance-based liquefaction triggering procedure quite well at the analyzed return periods. All computed R^2 values were greater than 0.98.

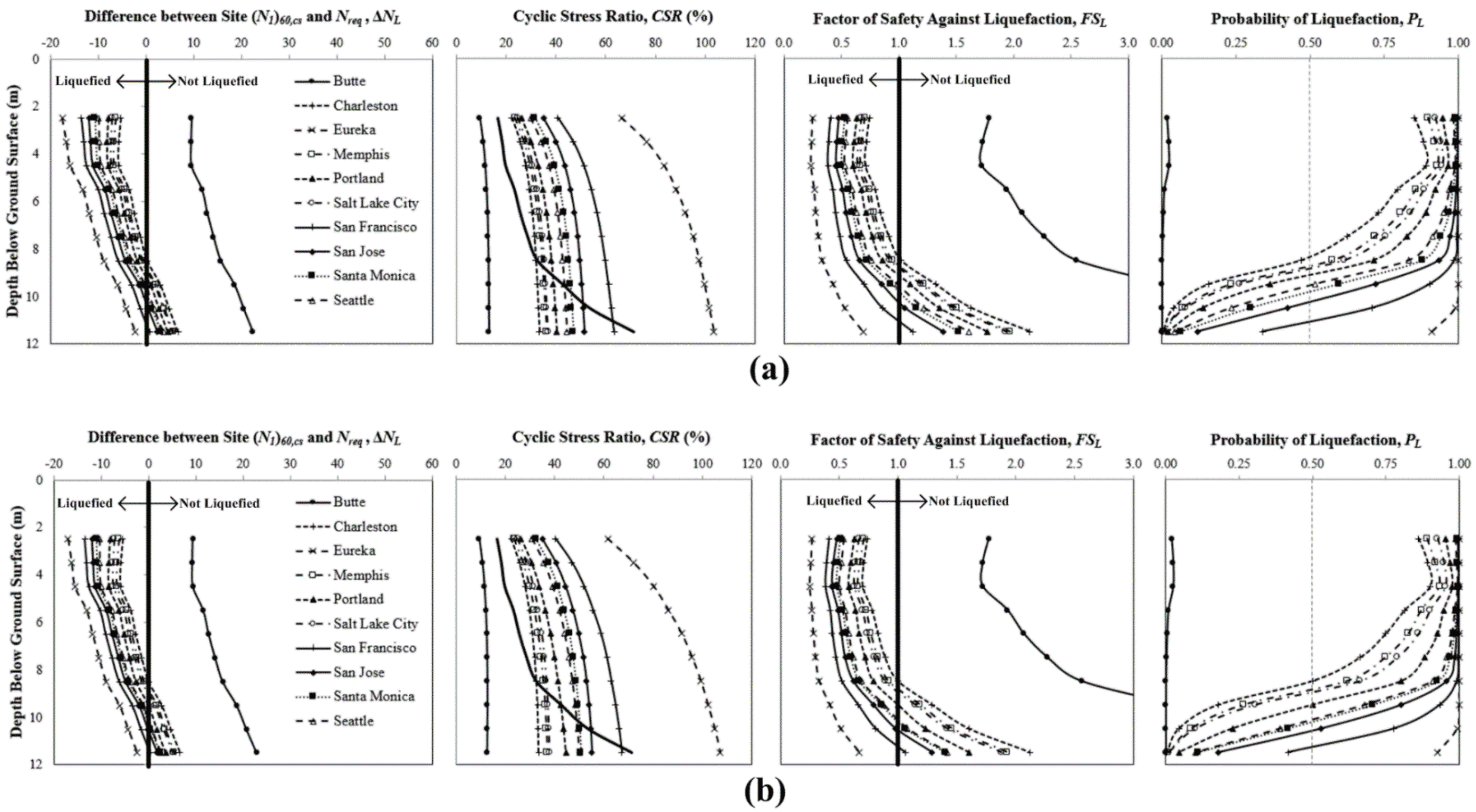

Figure 7-2: $CSR^{site}(\%)$, ΔN_L, FS_L^{site}, and P_L **with Depth as Calculated Using (a) the New Simplified Performance-Based Procedure, and (b) the Full Performance-Based Procedure (**T_R **= 1,033 Years)**

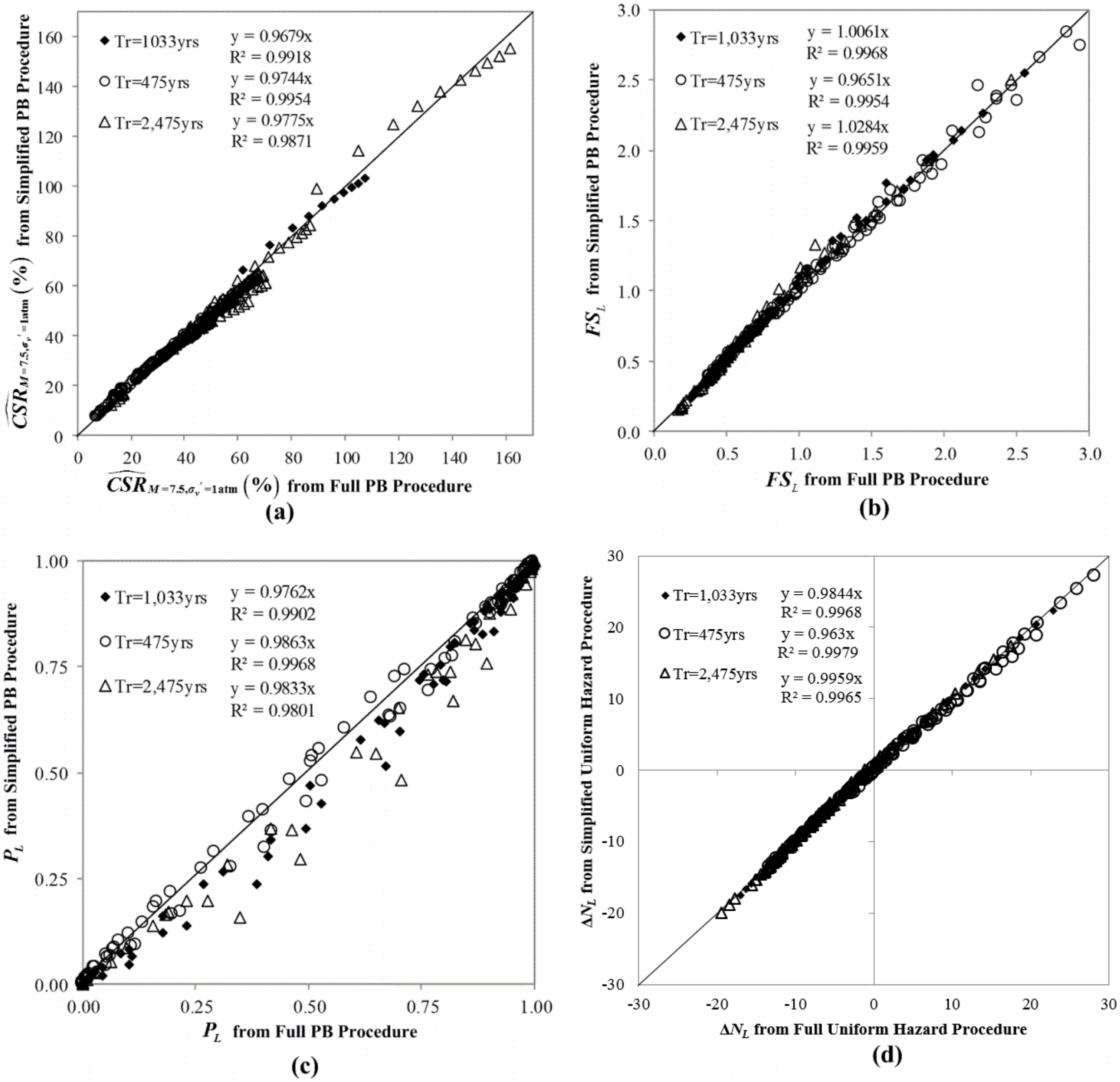

Figure 7-3 Comparative Scatter Plots for Simplified and Full Performance-Based Procedures for (a) $CSR_{M=7.5,\sigma_v'=1atm}(\%)$, (b) FS_L, (c) P_L, and (d) ΔN_L

Examination of the P_L scatterplot in Figure 7-3(c) reveals some increased scatter in the vicinity of $P_L = 0.50$, but relatively little scatter near the tails (i.e., $P_L = 0\%$ and $P_L = 100\%$). This scatter in the vicinity of $P_L = 50\%$ can be attributed to the very steep slope of the cumulative distribution function near a probability value of 50%. Engineers should therefore be aware that even very small errors in the computed $CSR_{M=7.5,\sigma_v'=1atm}$ can be somewhat amplified in Equation (6-39) if the computed value of P_L is between 25% and 75%.

7.2 **Grid Spacing Study**

As discussed previously in the derivation of the new simplified performance-based liquefaction assessment procedure, this new procedure is dependent upon accurate reference maps called liquefaction loading maps. As part of the development of these maps, the map-maker must decide how many full performance-based analyses to perform and where to perform them. This decision is crucial to the accuracy of the liquefaction loading maps. If the pre-determined locations of the full performance-based analyses are spaced too far apart, the resolution of the map may not be fine enough to capture the subtle changes in liquefaction hazard across geographic areas. This lack of detail may lead to decreased accuracy. On the other hand, if the locations of the full performance-based analyses are spaced too close together, the number of analyses required to map a large area may be too computationally difficult. For this research, several states were meant to be mapped, which required both computational efficiency and adequate accuracy. This section of the paper will discuss how the proper grid spacing (i.e. distance between geographic points to be analyzed) was determined to achieve these two requirements.

7.2.1 Preliminary Study of the Correlation with Peak Ground Acceleration

The objective of this study was to develop a simple, well-defined set of rules for determining optimum grid spacing. It was initially hypothesized that optimum grid spacing would be dependent upon peak ground acceleration (i.e. *PGA*), which is one of the input parameters in the Boulanger and Idriss (2012) probabilistic liquefaction initiation model. Specifically, it was hypothesized that areas of high seismicity would require finer grid spacing and areas of low seismicity would not require such high resolution to achieve the desired accuracy. To explore the effects of *PGA* on optimum grid spacing, this preliminary study focused on four cities in areas of varying seismicity: Berkeley, California; Salt Lake City, Utah; Butte, Montana; and Clemson, South Carolina with *PGA* values as shown in Table 7-3.

Table 7-3: Cities Used in Preliminary Grid Spacing Study

City	**Anchor Point**		***PGA* (g) (T_R = 2475 years)**
	Latitude	**Longitude**	
Berkeley, CA	37.872	-122.273	1.1340
Salt Lake City, UT	40.755	-111.898	0.6478
Butte, MT	46.003	-112.533	0.1785
Clemson, SC	34.683	-82.837	0.1439

Using a square grid (like the one shown in Figure 7-4) with the city's anchor point as the center of the square, several grid spacings were tested. This preliminary testing process included grid spacings of 1, 2, 4, 8, 16, 25, 35, and 50 km (0.62, 1.24, 2.49, 4.97, 9.94, 15.5, 21.7 and 31.1 mi). Then a full performance-based liquefaction analysis was performed at each corner point and the center anchor point to solve for N_{req} and *CSR*% at three return periods (475, 1033, and 2475 years). This process was repeated for each city in the preliminary study.

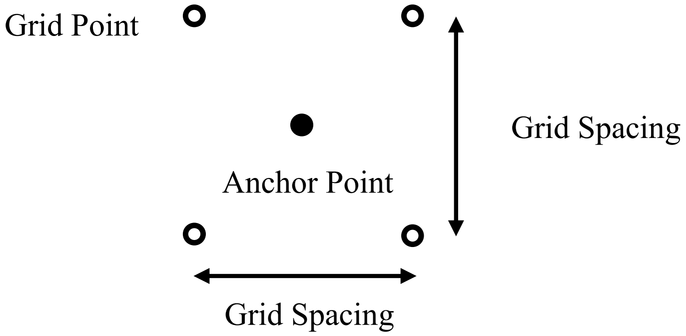

Figure 7-4. Layout of Grid Points Centered on a City's Anchor Point

An estimate of the liquefaction hazard at the center point (i.e. the interpolated value of either N^{ref}_{req} or CSR^{ref}%) was calculated using the four corner points. This interpolated value was then compared to the actual value of the center point as calculated using a full performance-based liquefaction analysis. The difference between the interpolated value and the true value at the center is called the error term. The error terms were normalized to the actual values at the anchor points by calculating the percent error term as follows:

$$PercentError = \frac{|\,InterpolatedValue - ActualValue\,|}{ActualValue} \times 100\% \tag{7-1}$$

The maximum percent error (i.e. the maximum percent error across all return periods for a given anchor point) became the deciding parameter in selecting optimum grid spacing for a given location. The relationship between maximum percent error and grid spacing was analyzed for each city and is displayed in Figure 7-5, Figure 7-6, Figure 7-7, and Figure 7-8. As can be seen in these figures, the relationship between maximum percent error and grid spacing is different for each city. Berkeley had the highest *PGA* value (1.1340g) out of the cities used in this preliminary study and required the smallest grid spacing (approximately 5 km or 3.107 mi) to restrict the maximum percent error to 5%. On the other hand, the maximum percent error for Clemson, which had the lowest *PGA* value (0.1439g), never exceeded 1% even with 50km (31.07 mi) grid spacing. Based on these graphs, it appears that seismicity (or *PGA*) has an impact on optimum grid spacing.

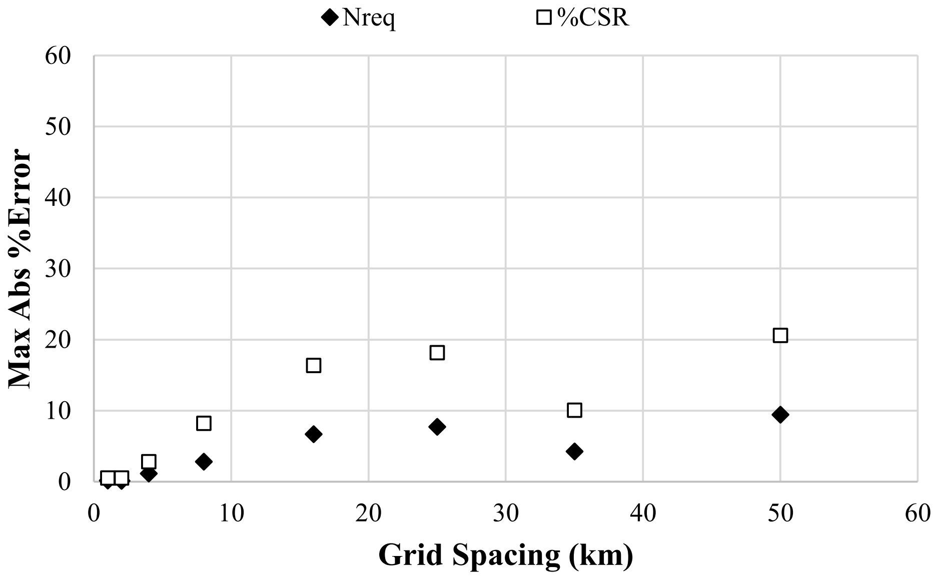

Figure 7-5. Variation of Maximum Absolute Percent Error with Increasing Distance between Grid Points (Berkeley, CA)

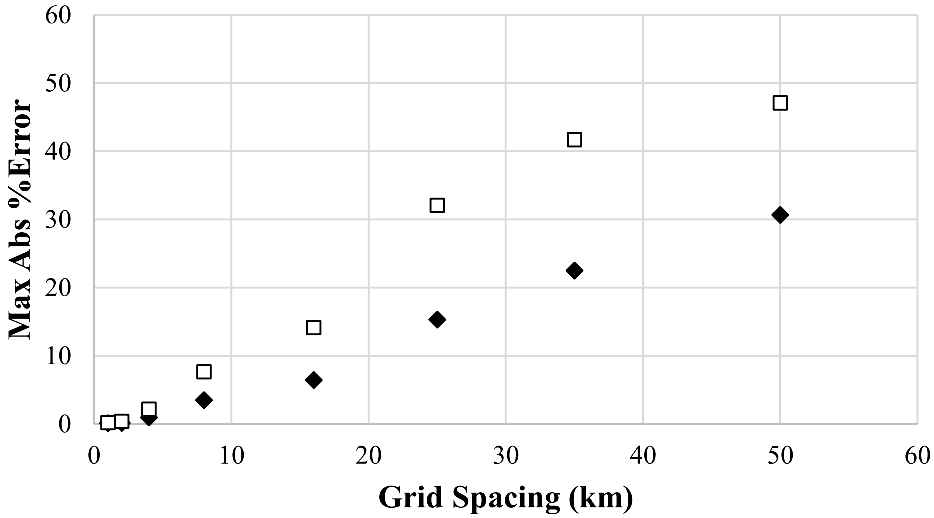

Figure 7-6. Variation of Maximum Absolute Percent Error with Increasing Distance between Grid Points (Salt Lake City, UT)

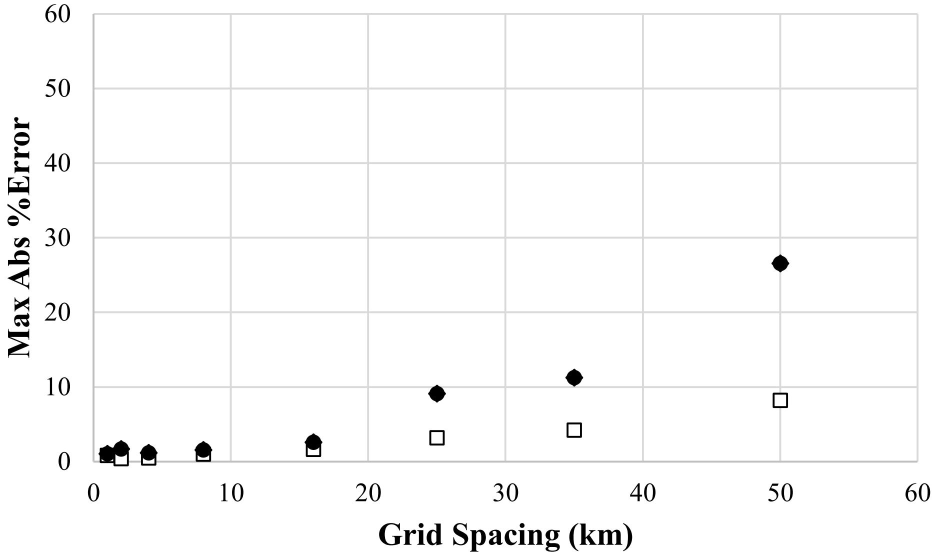

Figure 7-7. Variation of Maximum Absolute Percent Error with Increasing Distance between Grid Points (Butte, MT)

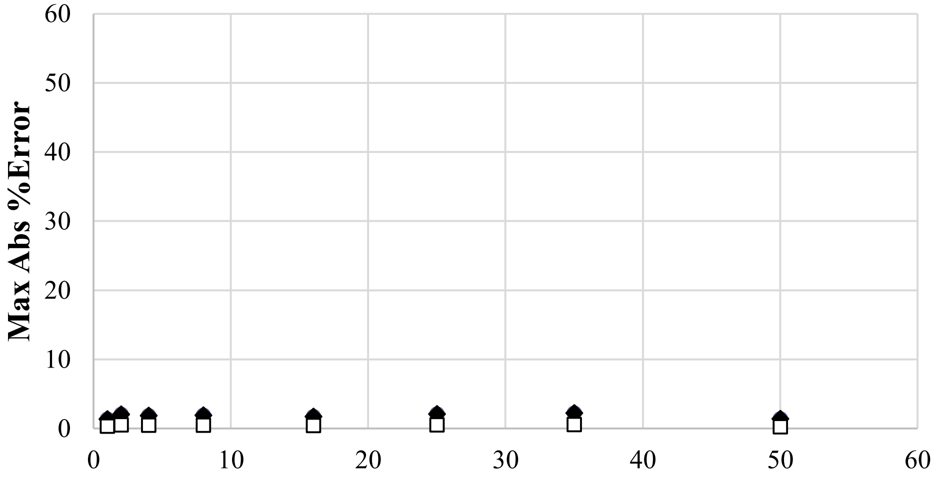

Figure 7-8. Variation of Maximum Absolute Percent Error with Increasing Distance between Grid Points (Clemson, SC).

7.2.2 Development of a Correlation between *PGA* and Optimum Grid Spacing

Based on the data from the preliminary study, it was assumed that *PGA* did have an effect on the relationship between grid spacing and maximum percent error. Specifically, it was hypothesized that as *PGA* increases, the optimum grid spacing decreases. To estimate the effect of *PGA* on optimum grid spacing, a similar study was conducted focusing on 36 cities from a wide range of *PGA* values (Figure 7-9).

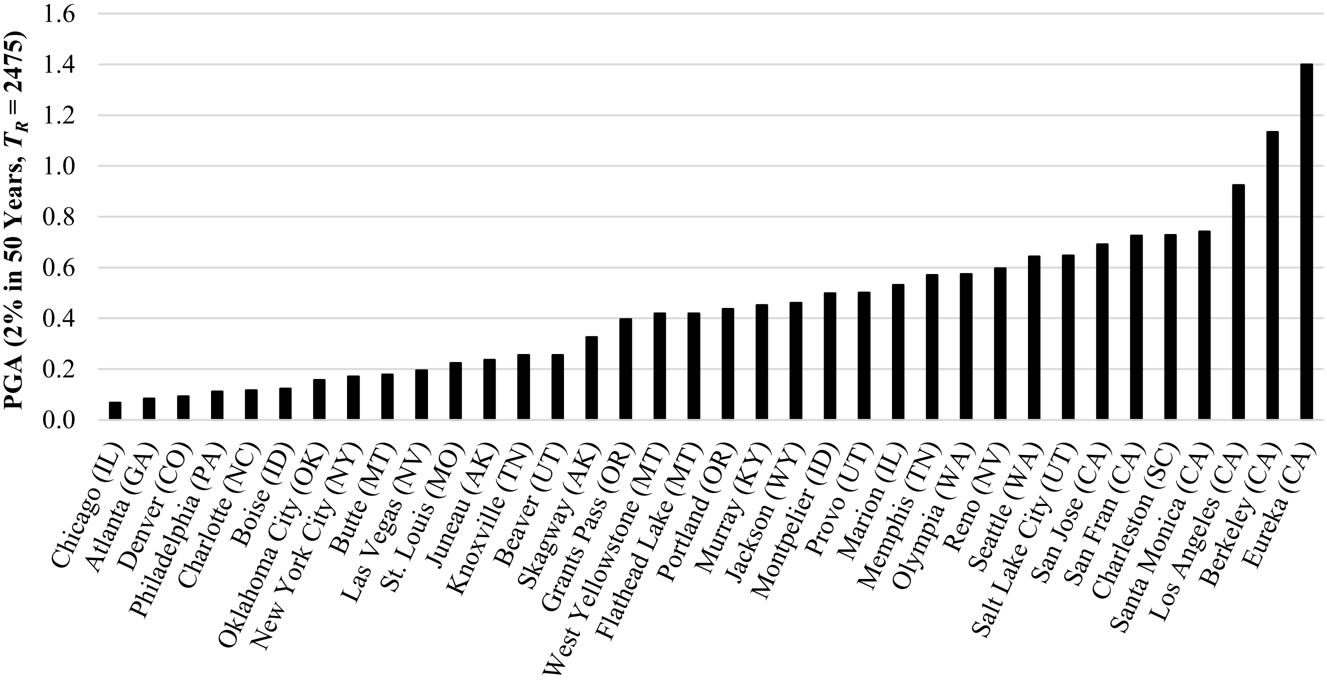

Figure 7-9. Range of *PGA* Values for Cities Included in Grid Spacing Study

The desired outcome of the final grid spacing study was to create a correlation between *PGA* and optimum grid spacing in km. An equation for the best-fit trend line alone would not be sufficient, because defining grid points to use in an analysis does not work well with non-integer values for grid spacing and constantly changing distances between points. Therefore, it was necessary to divide the different cities into *PGA* "bins" or defined ranges of values. These bins were determined using the USGS 2008 *PGA* hazard map (T_r = 2475 years) as shown in Figure 7-10. The *PGA* hazard map was chosen because it was clear and readily available as a well-documented definition of which areas in the country had significantly different seismicity levels compared to other areas' seismicity levels. The objective of this study was to determine the optimum grid spacing for each color bin.

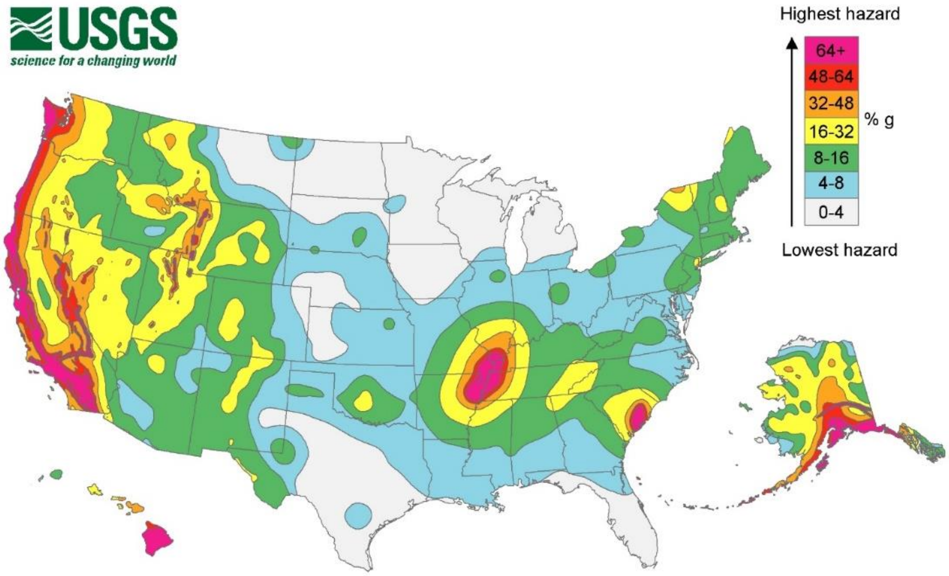

Figure 7-10. *PGA* Hazard Map (T_R = 2475 years) after USGS 2008

As in the preliminary study, a full performance-based analysis was performed at the anchor point of each city and at the corners of the grid surrounding the anchor point. This was repeated for multiple grid spacings until the percent error was within a reasonable amount. It was determined that "optimum grid spacing" would be defined as the smallest grid spacing (i.e shortest distance between grid points) that yielded a maximum percent error of 5% across all return periods based on *CSR*%. This definition is used because when the maximum percent error based on *CSR*% is limited to 5%, the interpolated value of N_{req} is within 1.2 blow counts of the actual value calculated at the anchor point, as shown in Figure 7-11. This seemed to be a reasonable amount of error, considering the inherent error in obtaining SPT blow counts during soil exploration at a site. If the definition of optimum grid spacing was defined as the smallest grid spacing that yielded a maximum difference of 1.2 blow counts, then the values of percent error based on *CSR*% may be unacceptably high. For example, as shown in Figure 7-11, if the maximum difference in N_{req} is 1.2 blow counts, the percent error in *CSR*% could be as high as 22.7%, which could cause substantial inaccuracies. Thus the definition of optimum grid spacing was defined based on *CSR*% and not N_{req}.

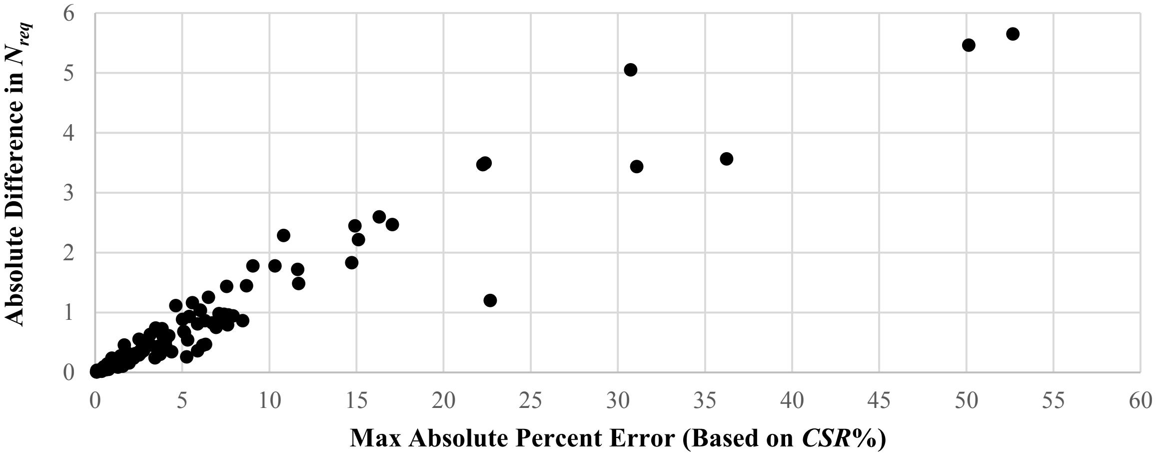

Figure 7-11. Comparison of Difference in N_{req} to Max Absolute Percent Error Based on *CSR*%

Optimum grid spacing was estimated for each city included in the study that reached at least a maximum percent error of 5% based on *CSR*% (not N_{req}). Optimum grid spacing was then plotted against *PGA* as shown in Figure 7-12. The vertical dashed lines indicate the boundaries between *PGA* bins as defined in the USGS 2008 *PGA* hazard map. The general trend of the points ($R^2 = 0.584$) supports the hypothesis that as *PGA* increases the optimum grid spacing decreases.

A hand-drawn lower bound was used to determine the optimum grid spacing based on *PGA*. The lower bound line was chosen as a conservative estimate of optimum grid spacing.

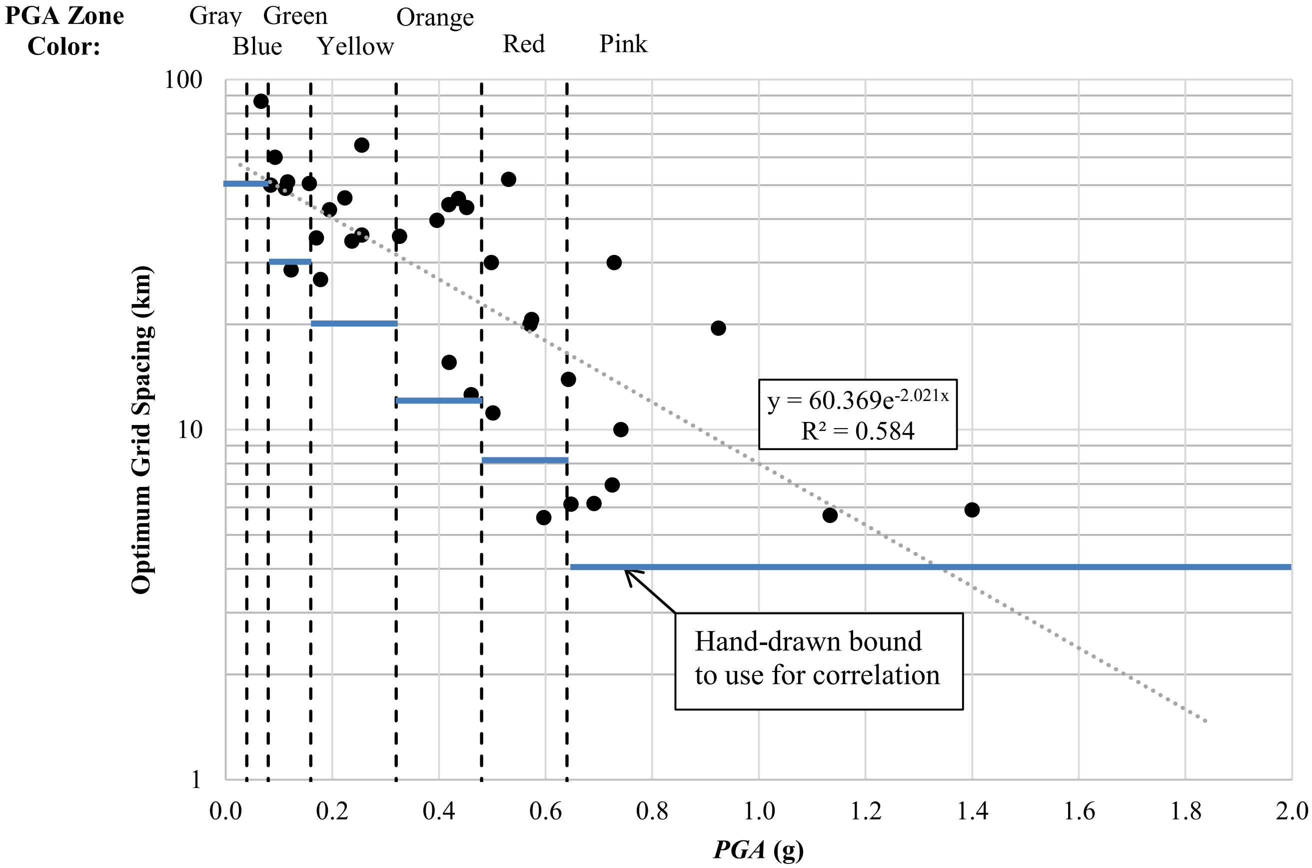

Figure 7-12 Correlation between *PGA* and Optimum Grid Spacing to Achieve 5% Maximum Absolute Percent Error (Based on *CSR*%)

The hand-drawn lower bound shown in Figure 7-12 was used to determine the set of rules for selecting grid spacing in the mapping procedure. Within each *PGA* bin, a lower-bound value for optimum grid spacing was selected. The set of rules includes one optimum grid spacing distance for each *PGA* bin included in the study. Table 7-4 summarizes this set of rules. In summary, the correlation determined in this grid spacing study provided a set of rules to use when creating liquefaction loading maps of *CSR*% and liquefaction parameter maps of N_{req}.

Table 7-4: Proposed Set of Rules to Determine Optimum Grid Spacing within a *PGA* Range

PGA	Color	Spacing (km)	Spacing (mi)
0 - 0.04	Gray	50	31.1
0.04 - 0.08	Blue	50	31.1
0.08 - 0.16	Green	30	18.6
0.16 - 0.32	Yellow	20	12.4
0.32 - 0.48	Orange	12	7.5
0.48 - 0.64	Red	8	5.0
0.64+	Pink	4	2.5

7.3 **Development of Liquefaction Loading Maps**

Development of liquefaction loading maps is performed in four steps: 1) create a list of geographic coordinates following the prescribed set of rules for grid spacing (Table 7-4), 2) run full probabilistic analyses at those locations, 3) use an interpolation scheme (e.g. Kriging, inverse distance weighted) to develop a continuous surface across the gridded region, and 4) create contour lines to visually represent the change in the mapped reference parameter. The software ArcMAP 10.1 (ESRI, 2011), developed by the Environmental Systems Research Institute, ESRI, was used to perform steps 1, 3 and 4 while *PBLiquefY* (Wright 2013; Franke et al. 2014d) was used to perform step 2.

7.3.1 Creating the List of Grid Points to Be Analyzed

Using ArcMap, each state in the study was divided into polygons representing the different *PGA* color zones from the USGS 2475-year return period *PGA* hazard map (USGS 2008, Figure 7-10). The "Fishnet" tool in ArcMAP created a grid of points at a specified grid spacing (Table

7-4) within each color zone. These points were merged into one shapefile for each state and exported to a text file of geographic coordinates to be analyzed using *PBLiquefY*.

Additionally, the representatives for each state involved in the research was asked to provide a list of any sensitive areas that they felt constituted an "Area of Concern" (AOC). These areas were locations where a finer grid spacing was thought necessary to provide more refined contours of N_{req} or $CSR\%$. An AOC could be a densely populated urban area, an area with sensitive infrastructure, or some area of critical interest to the state DOT. Each AOC was treated as though it were in a *PGA* color zone two levels above its actual color zone. For example, if the AOC was in the green section of the hazard map, the grid spacing in the AOC would be reduced to that of the orange level. Areas that were in a red *PGA* color zone were treated as though they were in a pink zone and areas that were in a pink zone were not treated any differently. This is because the grid spacing chosen for this zone was already an exceptionally conservative value. An example of the distribution of points across a state is provided in Figure 7-13. Some points outside of the state borders were added to increase the accuracy of the maps near the edges of the state boundaries. The total number of coordinates analyzed in each state is presented in Table 7-5.

Table 7-5: Number of Grid Points Analyzed for Map Development (by State)

State	Number of Grid Points to Analyze
AK	17,927
CT	190
ID	2,511
MT	1,585
SC	937
UT	947
Total	**24,097**

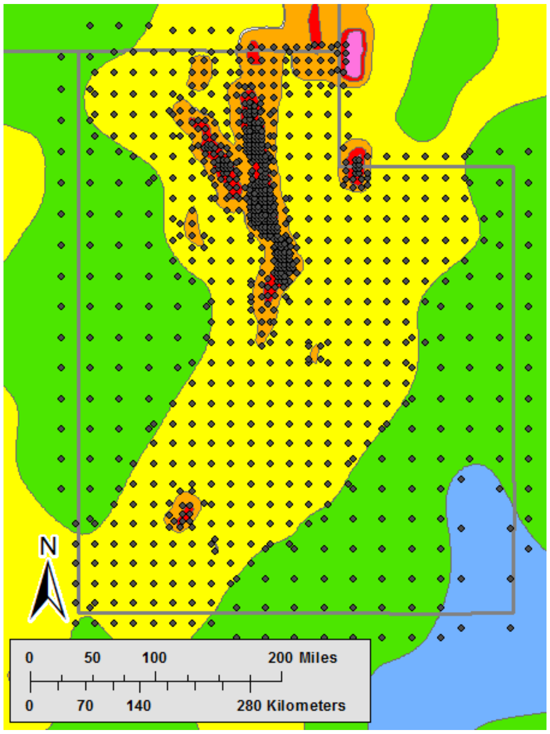

Figure 7-13 Location of Grid Points for Utah with *PGA* Color Zones in Background

7.3.2 Analysis of Grid Points

Each text file containing geographic coordinate points to be analyzed were entered into the program *PBLiquefY*. *PBLiquefY* produced output files containing full performance-based results (N_{req} for the Cetin et al., 2004 method and *CSR*% for the Boulanger and Idriss, 2012 method) for the given reference soil profile (Figure 6-2) at three return periods: 475, 1033, and 2475. As discussed in the derivation of this simplified method, the 2008 equation for the *MSF* factor was used for the Boulanger and Idriss (2012) analyses and the value of F_{PGA} was fixed at 1.0 for all analyses. As discussed previously, the full performance-based analyses for CT, ID, MT, SC, and UT were based on the 2008 USGS deaggregations while the analyses for AK were based on the 1996 USGS deaggregations. The output files produced by *PBLiquefY* were then opened in ArcMAP software for spatial interpolation and contouring.

7.3.3 Interpolation between Analyses at Specified Grid Points

The analyzed grid points in the previous step do not capture every possible location an engineer would need to analyze, which means that an interpolation between analyzed grid points is necessary. Several interpolating schemes are available in ArcMAP such as inverse-distance weighting (IDW), natural neighbor, kriging and co-kriging (ESRI Resource Center). Kriging was selected as the interpolation method for this study because several studies have shown that kriging methods tend to produce less error and perform better than other non-geostatistical schemes like IDW (Li and Heap, 2011 and Luo et al., 2007). Though co-kriging has been shown to be slightly more accurate than kriging (Luo et al., 2007), the difference in interpolation error is small and the kriging method is easier and faster. A sample kriging raster is visually represented in Figure 7-14.

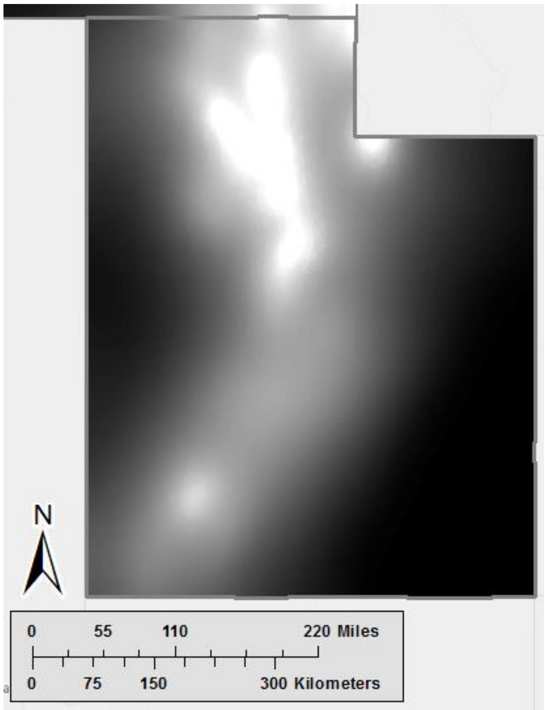

Figure 7-14: Sample Kriging Raster for Utah (N_{req}^{ref}, T_R = 1033) with Light Areas as Larger Values of N_{req}^{ref}

The analyzed grid points for each state were interpolated within their respective state boundaries except for the mountain-west states. The three mountain-west states (UT, MT, and ID) were interpolated together to improve accuracy and continuity at the borders between the states.

7.3.4 Creating Contours of the Interpolated Surface

Contour lines provide a visual aid for engineers to estimate the referenced liquefaction loading values CSR^{ref}(%) and N_{req}^{ref}. The appropriate spacing of the contour lines depends on the return period and scale of the map, how quickly the liquefaction loading values change with distance for the specific region, and the user's desired accuracy in interpolating between the contour lines (Figure 7-15 further illustrates this concept). For example, a map of the state of Utah may have larger differences in the liquefaction loading values between each line than would a map of Salt Lake County alone. A map of southeastern Utah, which has very little variation in both CSR^{ref}(%) and N_{req}^{ref}, would require a smaller difference between contour values than would a map of the Wasatch Front, which is highly variable in both CSR^{ref}(%) and N_{req}^{ref}. In the development of maps for this study, spacing between contour lines were chosen for each map based on what appeared to be most suitable for each region and scope.

Although contour lines are useful in a printed form, there could be user error in estimating the mapped reference value for a site between contour lines. A more accurate way to obtain the mapped value is available through opening the raster file in ArcMap or some other geospatial software. The user could enter the exact coordinates for the site of interest and retrieve the mapped reference value from the Kriging interpolation. Though this method is more accurate, not all engineers have such software available or the necessary training. In this case, the printed maps with contour lines would be sufficient. Completed maps for each state in this study at return periods of 475, 1033, and 2475 are provided in Appendix B as Figures B-1 through B-35. Further explanation of how to use the maps is provided in Section 7.6 “Simplified Performance-based Liquefaction Assessment Procedure”.

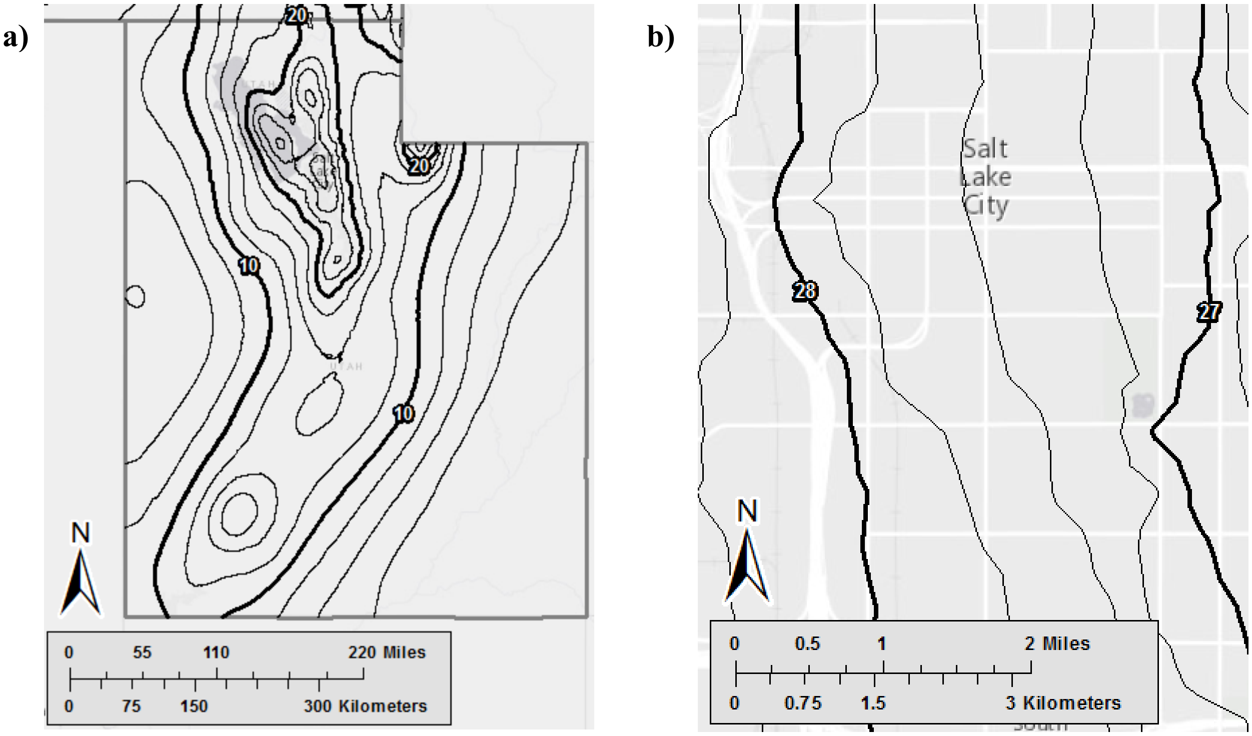

Figure 7-15: Comparison between a) Map of Utah with Contour Spacing of 2.5 SPT Blow Counts, and b) Map of Salt Lake City with Contour Spacing of 0.25 SPT Blow Counts (Both Maps Represent T_R = 1033 Years)

7.4 Comparison between Deterministic and Simplified Performance-based Methods

Though performance-based methods have many advantages, there are some cases where a deterministic analysis may be beneficial. To identify which cases would require a deterministic analysis, three cities were selected for a comparison study: Butte, MT (low seismicity); Salt Lake City, UT (medium seismicity); and San Francisco, CA (high seismicity). The liquefaction hazard in each city was estimated using three different methods: deterministic, pseudo-probabilistic, and simplified performance-based. The simplified performance-based method has been described previously in this report. The deterministic and pseudo-probabilistic procedures are described as follows.

7.4.1 Deterministic Liquefaction Hazard Analysis

In the deterministic procedure, ground motions are obtained through a DSHA (described previously). A DSHA involves deterministically assessing the seismic sources in the nearby region of the site of interest and identifying the source that produces the highest hazard in the area. The software EZ-FRISK was used to identify the top five seismic sources within 200 km for San Francisco and Salt Lake City. The 2008 USGS Seismic Source Model within EZ-FRISK does not include some faults in low seismic regions, such as Butte. Thus, the governing fault for Butte (Rocker Fault) was identified using the USGS quaternary fault database (USGS et al., 2006). In the case of Salt Lake City and San Francisco, EZ-FRISK provided values of M_w, PGA, and R for both the 50th (i.e. median) and 84th (i.e. median + σ) percentiles using three of the NGA models for the Western United States (Boore and Atkinson, 2008; Campbell and Bozorgnia, 2008; and Chiou and Youngs, 2008) and weighting schemes shown in Table 7-6. For Butte, the 50th and 84th percentile M_w values were estimated using a correlation with surface rupture length developed by Wells and Coppersmith (1994), and PGA was calculated using the same three NGA models based on measured dimensions and assumed characteristics of the Rocker Fault. Summaries of the seismic sources considered in this DSHA and details of the Rocker Fault calculations are provided in Tables C-1 and C-2, respectively, in the appendix. Once the model inputs have been determined through the DSHA they are entered into the respective empirical liquefaction hazard models. A summary of the governing input variables used in the deterministic liquefaction initiation and lateral spread displacement models are provided in Table 7-7.

Table 7-6: NGA Model Weights Used in the Deterministic Procedure

Attenuation Model	Weight
Boore & Atkinson (2008)	0.333
Campbell & Bozorgnia (2008)	0.333
Chiou & Youngs (2008)	0.333

Table 7-7: Input Variables Used in the Deterministic Models (a_{max} Calculated Using F_{pga} from AASHTO Code)

Location	Latitude	Longitude	Distance (km)	Mean M_w	Median (50%)		Median + σ (84%)	
					PGA	a_{max}	PGA	a_{max}
Butte	46.003	-112.533	4.92	6.97	0.5390	0.5390	0.9202	0.9202
Salt Lake City	40.755	-111.898	1.02	7.00	0.5911	0.5911	1.005	1.005
San Francisco	37.775	-122.418	12.4	8.05	0.3175	0.3754	0.5426	0.5426

Estimations of liquefaction initiation potential (FS_L, N_{req}, and CSR%) were calculated deterministically using equations from the Idriss and Boulanger (2008) liquefaction triggering model (Equations (4-6), (4-7) and (4-1), presented previously).

7.4.2 Pseudo-probabilistic Liquefaction Hazard Analysis

In the pseudo-probabilistic procedure, the variables used in the empirical liquefaction hazard models are obtained from a PSHA (previously described). These variables are used in the same equations used in the deterministic analysis. The USGS 2008 interactive deaggregation website (USGS 2008) provided the mean magnitude (M_w), peak ground acceleration (PGA) for rock, and source-to-site distance (R) from a PSHA at a return period of 1,039 years for each city of interest. The resulting values are summarized in Table 7-8.

Table 7-8: Input Values Found Using USGS 2008 Deaggregations (T_R = 1,039 years)

Location	Latitude	Longitude	Distance (km)	Mean M_w	PGA	F_{pga}
Butte	46.003	-112.533	24.9	6.03	0.1206	1.559
Salt Lake City	40.755	-111.898	4.20	6.84	0.4030	1.097
San Francisco	37.775	-122.418	12.0	7.38	0.5685	1.000

7.4.1 Comparisons with the Simplified Performance-based Procedure

In each of the three cities analyzed, the results from the pseudo-probabilistic procedure suggested greater liquefaction hazard than the results from the performance-based procedure. The direct comparison of both methods is provided in Figure 7-16.

Direct comparison plots (Figure 7-17 through Figure 7-19) show that the deterministic analyses frequently over-predicted liquefaction hazard. This over-prediction is especially evident in the case of Butte where the simplified performance-based method estimated N_{req} values as low as 3.1% of the deterministic N_{req} values. This discrepancy could be because the likelihood of the large Rocker Fault near Butte rupturing and achieving the 50% ground motion is very low. Therefore, in the simplified performance-based approach (which incorporates likelihoods of seismic events in the calculations), the associated N_{req} is much lower. These comparison plots also highlight the significant discrepancy between the 50th and 84th percentile ground motions. In the case of San Francisco at the 2,475-year return period, the 50th percentile ground motions under-predict N_{req} while the 84th percentile ground motions over-predict N_{req}. This discrepancy produces a dilemma for the engineer who has to decide which ground motions appropriately characterize the liquefaction hazard for the given site. However, the simplified performance-based procedure does not depend on this decision and can provide a more consistent estimate of liquefaction hazard.

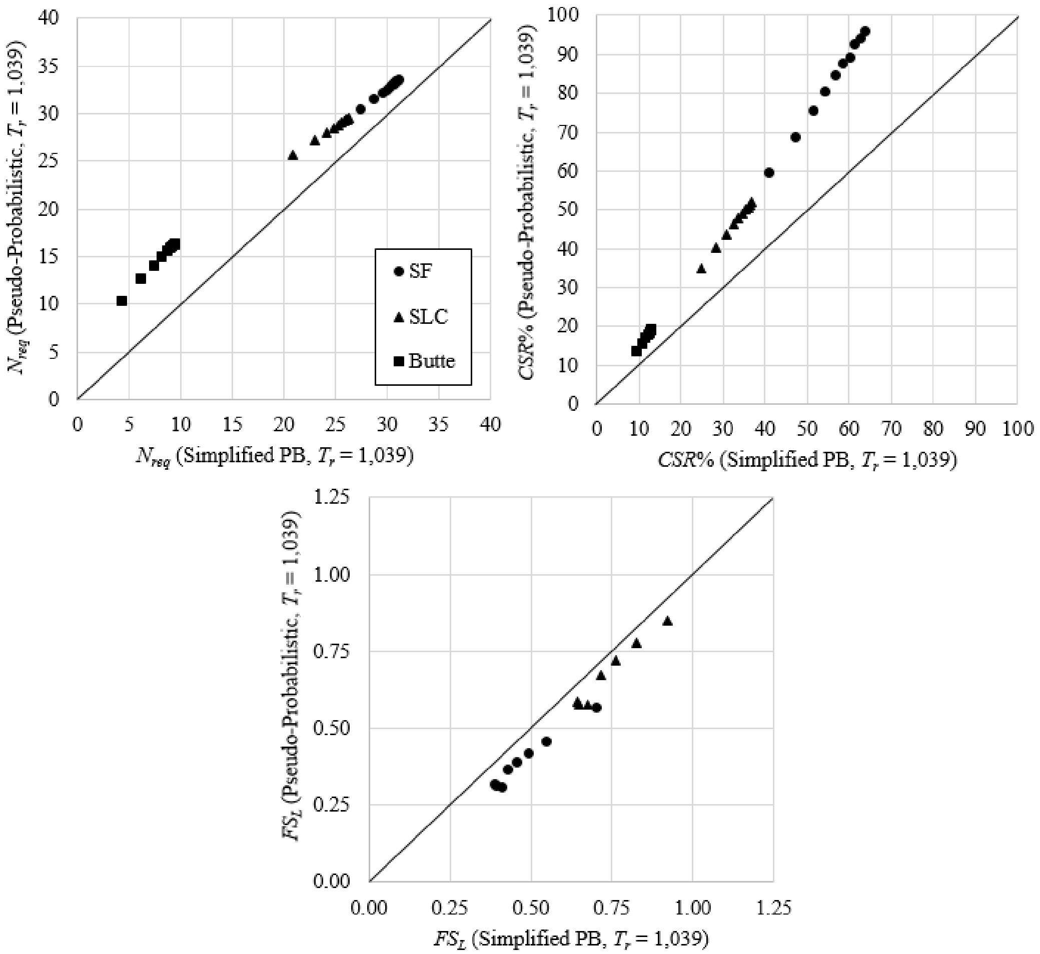

Figure 7-16: Comparison of Pseudo-Probabilistic and Simplified Performance-Based Values of N_{req}, CSR%, and FS_L.

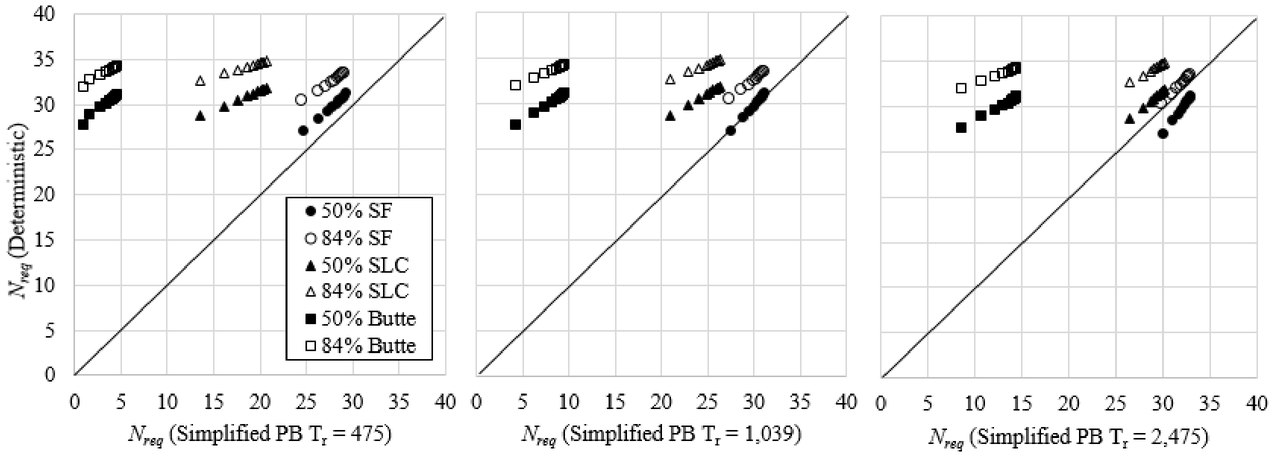

Figure 7-17: Comparison of Deterministic and Simplified Performance-Based Values of N_{req}.

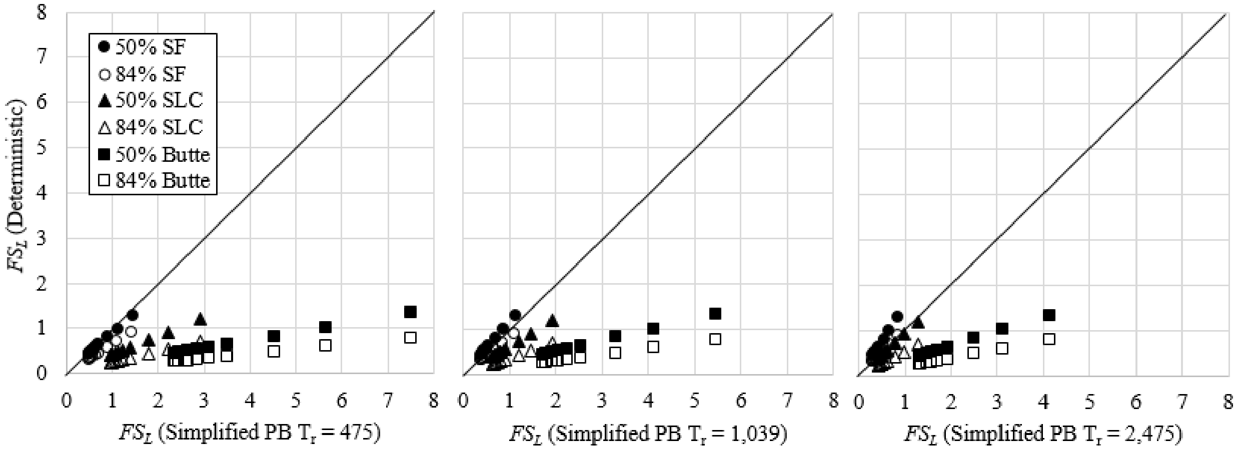

Figure 7-18 Comparison of Deterministic and Simplified Performance-Based Values of *FS_L*.

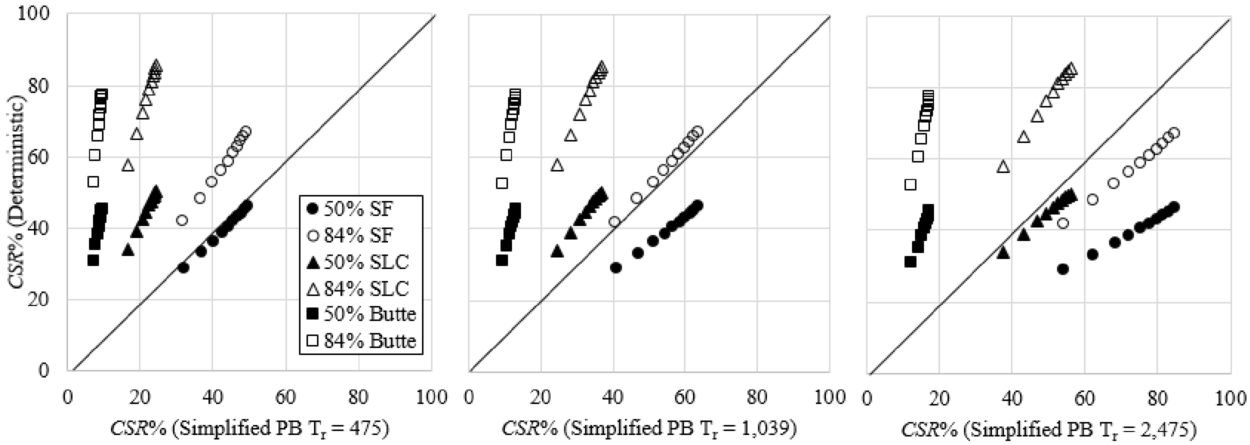

Figure 7-19: Comparison of Deterministic and Simplified Performance-Based Values of *CSR*%.

7.4.1 How Deterministic Analyses Should Be Incorporated

The results of this comparison study show that deterministic methods severely over-predicted liquefaction hazard in Butte—an area of low seismicity. The deterministic results also slightly over-predicted liquefaction hazards at high return periods in Salt Lake City—an area of medium seismicity. In San Francisco—an area of high seismicity—the deterministic methods slightly under-predicted liquefaction hazard when considering the 50th percentile ground motions in the deterministic method and the 2,475-year return period in the simplified performance-based procedures. These results suggest that the deterministic results could be used as an upper bound in areas of high seismicity, but in areas of low seismicity, the deterministic analysis could be optional. Engineers performing analyses in areas of medium to high seismicity could choose to use a deterministic analysis as a "reality check" against the simplified performance-based results. If both deterministic and performance-based methods are considered, engineers should apply the following rule: the *lowest* hazard governs (i.e. lower value of N_{req}, P_L, or CSR, and higher value of FS_L).

This rule may seem counter-intuitive, but the idea is not completely foreign—when developing a spectral acceleration design envelope, the lower of the deterministic and probabilistic values is the governing acceleration. Likewise, in a liquefaction hazard analysis, the lower value governs. The reasoning behind this rule is as follows: if the deterministic value is lower than the performance-based value, the combination of multiple seismic sources in the performance-based analysis may suggest greater liquefaction hazard than would be caused by a single, nearby, governing fault. Therefore, the deterministic analysis provides a type of "reality check" against the performance-based analysis, and the deterministic results should be accepted. If the performance-based value is lower than the deterministic value, the reason may be that the governing fault has a significantly low likelihood of rupturing and achieving the 50th or 84th percentile ground motions. In this case, the deterministic results could be considered too extreme (especially for some projects that do not need to be designed to withstand such infrequent large events). Therefore, the performance-based results should be accepted as a representation of the more *likely* liquefaction hazard.

7.5 Simplified Performance-based Liquefaction Assessment Tool

To further simplify the process of using the new simplified performance-based method, a macro-enabled Excel spreadsheet (the *Simplified PB Liquefaction Assessment Tool*) was developed to perform the site-specific correction calculations and the deterministic analysis calculations when necessary. This section explains the components of the tool and provides some guidance on how it should be used.

7.5.1 Inputs

This section of the spreadsheet is the starting place of the analysis. Here, the user may select which analyses and options he or she would prefer and enter the soil profile information, mapped reference values, and other parameters that are necessary for the simplified performance-based procedure. At the bottom of the sheet, there is a section for deterministic inputs if the user would like to consider a deterministic analysis as well.

7.5.2 Map Help

This section shows an example of a $\log[D_H^{ref}]$ map and shows how to retrieve the mapped liquefaction loading value or lateral spread displacement value.

7.5.3 Simplified Performance-based Liquefaction Initiation

This section of the spreadsheet shows the calculations for the simplified performance-based liquefaction initiation procedure. The Boulanger and Idriss (2012) model is simplified as derived previously. The Cetin et al. (2004) model is simplified as derived in the Mayfield et al. (2010) publication. This section also provides the calculations for correcting field SPT blow counts to values of $(N_1)_{60,cs}$. The user is not required to do anything on this page. This section is simply for reference if the engineer would like to see the calculation process.

7.5.4 Deterministic Liquefaction Initiation

This section of the spreadsheet calculates deterministic liquefaction initiation values. The formulas for from the deterministic Idriss and Boulanger (2008) model and from the deterministic Cetin et al. (2004) model are used here. The user is not required to do anything on this page. This section is simply for reference if the engineer would like to see the calculation process.

7.5.5 Final Summary Report

This section shows the final results of the analyses chosen on the *Inputs* tab. The format of this section is already set up for easy printing. The headers of each page are associated with the project information entered on the *Inputs* tab. The first page provides a summary of inputs from the *Inputs* tab to facilitate easy checking of the inputs. The following pages show the results of the analyses. To print only the pages with the user-specified analyses, return to the *Inputs* tab and click the “Print Final Summary” button. The print preview window will appear and show only the user-specified analyses.

7.5.6 References

This section provides references for the models used in this spreadsheet and further guidance for using this spreadsheet.

7.6 Simplified Performance-based Liquefaction Assessment Procedure

This section describes the suggested simplified procedure for assessing liquefaction triggering hazard and lateral spread displacement.

1) Select an appropriate return period (T_R) for the project (this may depend on the intended use of the building, code requirements, etc.).

2) Retrieve the reference liquefaction loading value (i.e. N_{req}^{ref} or CSR^{ref}%) from the map with the desired return period and model (i.e. Cetin et al, 2004 or Boulanger and Idriss, 2012). Note that provided N_{req}^{ref} maps are based on the Cetin et al. model and *CSR*% maps are based on the Boulanger and Idriss model.

3) Open the simplified performance-based liquefaction assessment tool (provided as part of this report). Enter the required soil profile information into the *Inputs* tab. Required values include depth to center of the sublayer, field SPT blowcount, unit weight (γ), fines content in percent, and thickness of each sublayer.
    a. K_{DR}, a correction factor for age of sand deposits after the research of Hayati and Andrus (2009), is available as an optional input parameter. This value is not required, but may be used to increase the *CRR* of particular soil layers.
    b. Enter hammer information (i.e. hammer efficiency, rod stickup length, sampling diameter), which is used for $(N_1)_{60,cs}$ corrections.
    c. Soil profile information can be entered in either SI or English customary units. Select the desired option by clicking the associated toggle above the soil profile table.
    d. Even though the zone of interest to the user may not include sublayers near the ground surface, all sublayers above the zone of interest must be included in the inputs tab so that the effective stress calculations will work properly. In other words, begin at the ground surface and include all sublayers down to the end of the zone of interest.

  e. In the column labeled “Soil Type”, enter a label for each soil layer that adequately describes the layer. This label is not incorporated in the analysis, but provides the user with additional detail in the final report summary.
  f. In the column labeled “Susceptible?”, mark either “Yes” or “No” for each layer. “Yes” indicates that the layer is susceptible to liquefaction and should be incorporated in the P_L, FS_L, CSR and N_{req} calculations. “No” indicates that the layer is not considered susceptible to liquefaction and will only be included in the analysis to allow calculations of σ_v and σ_v for other susceptible soil layers. P_L, FS_L, CSR and N_{req} will not be calculated for layers marked with “No” in the “Susceptible?” column.

4) On the *Inputs* tab under “Analysis Selections”, select the desired models and analyses. If the user wishes to use a deterministic analysis as an upper-bound to the performance-based results, the user should select the appropriate deterministic checkbox.

5) On the *Inputs* tab, enter liquefaction triggering parameters to be used in the simplified performance-based correction factors (derived in the Year 1 Quarter 1 report). The calculations will be performed in the spreadsheet automatically, but a few parameters must be provided by the user:
  a. *PGA*: Peak Ground Acceleration should be retrieved from the 2008 (or 1996, for Alaska) USGS Interactive Deaggregation website (http://geohazards.usgs.gov/deaggint/2008/) at the return period specified in step 1. Note that the website uses exceedance probabilities instead of return periods. Use Table 7-9 to convert return periods to exceedance probabilities.

Table 7-9. Conversions between Return Period and Exceedance Probability for Use in the USGS Interactive Deaggregations Website

	Exceedance Probability	
Return Period	**Percent**	**Years**
475	10	50
1,039 (1,033)	2 (7)	21 (75)
2,475	2	50

After entering the latitude and longitude of the site, exceedance probability, Spectral Period of 0.0 seconds, and $V_{s,30}$ of 760 m/s, retrieve the *PGA* from the output report. This value is necessary for estimating the F_{pga}. An example of where this number is located in the output report is provided in the *References* tab of the spreadsheet.

b. F_{pga}: If the user checks the “Calculate F_{pga} automatically” checkbox, the spreadsheet will calculate F_{pga} according to the 2012 AASHTO code. However, this cannot be done if the Site Class is F (see notes about Site Class below), and therefore, the user must specify an F_{pga} value based on a site response analysis.

c. M_w: The mean moment magnitude (M_w) is used to calculate the MSF correction factor as discussed in the Year 1 Quarter 1 report. The value for M_w is found in the same output report created to find the *PGA* value. An example of where this number is located in the output report is provided in the *References* tab of the spreadsheet.

d. $V_{s,12}$: The shear wave velocity in the upper 12m (40 ft) is only required when using the Cetin et al (2004) model. For further guidance in calculating this value, see the *References* tab of the spreadsheet.

    e. Site Class: The site class is necessary for calculating the F_{pga}. Site class is determined based on soil type and soil properties. See the *References* tab of the spreadsheet for further help in determining site class.

6) On the *Inputs* tab under "Mapped Reference Values", enter the mapped values retrieved as part of step 2. At least one of the two parameters (CSR^{ref} (%) or N_{req}^{ref}) is necessary for analysis, but be aware of which model each of these parameters is associated with (see step 2). Also report the return period associated with the chosen map (this value will not be used in any calculations, but will be displayed on the final summary page for reference).

7) If the user wishes to use a deterministic analysis as an upper-bound to the performance-based results, the user should enter the deterministic values of PGA, M_w, and percentile of the PGA to be considered. This percentile value is used in the calculation of CRR, where the P_L value in the CRR equation is equal to (1 – percentile/100%). The user must also specify a site class for the soil or provide a user-defined value for F_{pga}.
    a. Deterministic values of PGA and M_w should be assessed by an experienced individual with proper training in DSHA.
    b. It is suggested (as explained previously in this report) that a deterministic analysis should be considered when the engineer suspects that the project could benefit from a deterministic cap. In areas of low seismicity, this is likely unnecessary.

8) Several checkboxes are displayed near the top of the *Inputs* tab that allow the user to select which analyses (liquefaction initiation, settlement, lateral spread, or seismic slope stability), models (Cetin et al or Boulanger and Idriss or both), and options (P_L

or FS_L) the user would like to consider. Select the desired analyses, models, and options before proceeding to the next step.

9) Once everything is correctly entered into the *Inputs* tab, click “Analyze”. The calculations will be displayed on the *PB Liquefaction Initiation* and *Det Liquefaction Initiation* tabs.
10) The *Final Summary* tab displays plots, tables and a summary of inputs in a printable format. The headers of these pages provide information such as company name, project name/number, date, etc. entered at the top of the *Inputs* tab.

7.7 **Chapter Summary**

This chapter validates the simplified performance-based procedure derived in the previous chapter. A direct comparison between the simplified procedure and the full performance-based procedure for 10 cities at three return periods shows that the simplified procedure reasonably approximates the results of a full performance-based procedure. In addition, the process for developing liquefaction loading maps is described and performed for six states. A comparison of results from the deterministic method and the simplified method suggest that, in areas of high seismicity, it may be beneficial to use a deterministic analysis as a realistic upper bound to the simplified method. Detailed instructions on how to execute the simplified procedure are also provided.

8. CONCLUSIONS

Seismically-induced liquefaction has been the cause of significant damage to infrastructure and is a serious concern in current civil engineering practice. Researchers have found that performance-based methods of liquefaction assessment provide more consistent and likely estimates of liquefaction hazard. Unfortunately, performance-based liquefaction assessment is not easily performed and can be difficult for practicing engineers to use on routine projects. Previous research has shown that performance-based methods of liquefaction assessment can be simplified into an approximation procedure. This simplification has successfully been completed for the Cetin et al. (2004) empirical liquefaction triggering model (Mayfield et al., 2010). Until now, however, such a simplification has not been performed for the liquefaction triggering model developed by Boulanger and Idriss (2012). The purpose of this research was to derive and validate a simplified performance-based procedure using the methodology described by Mayfield et al. (2010) and the Boulanger and Idriss (2012) empirical liquefaction triggering model. The following steps were necessary to fulfill this purpose:

1) The simplified performance-based procedure was derived. This derivation included the equations for several correction factors that adjust a reference value, CSR^{ref} (%), to reflect site-specific soil conditions, CSR^{site} (%). The value of CSR^{site} (%) may be converted to several liquefaction parameters, including FS_L, P_L, and N_{req}.

2) The simplified performance-based procedure was validated by analyzing 10 cities using the simplified procedure and the full performance-based procedure. The results from each procedure were compared, and it was found that the simplified procedure closely approximates the results of a full performance-based procedure.
3) A grid study was performed to assess the proper distance between analysis points in the development of the liquefaction loading maps. One major finding of this grid study was that the optimum grid spacing between points was affected by the value of the *PGA* in the geographic region. Using the contoured *PGA* map provided by USGS (2008), a relationship between *PGA* color scale on the map and optimum grid spacing was developed.
4) Liquefaction loading maps for the simplified method derived in this thesis and liquefaction parameter maps for the Mayfield et al. (2010) procedure were created for six states: Alaska, Connecticut, Idaho, Montana, South Carolina, and Utah.
5) Results from the simplified performance-based procedure were compared to results from a deterministic procedure for three cities of varying seismicity. This comparison showed that a deterministic analysis may be beneficial in areas of high seismicity. In cases where the deterministic analysis results in lower estimates of liquefaction hazard than the results of the simplified performance-based method, the deterministic results may be used as an upper bound to the liquefaction hazard.
6) A detailed, step-by-step description of the simplified performance-based procedure is included, along with an introduction to a sample spreadsheet created for the use of the funding agencies (the *Simplified PB Liquefaction Assessment Tool*). This spreadsheet calculates the correction factors for both the Mayfield et al. (2010) simplified procedure

and the simplified procedure derived in this thesis and also performs calculations for deterministic analyses, if desired.

The benefit of this simplified performance-based procedure is that practicing engineers may be able to more easily estimate the results of a full performance-based procedure using the Boulanger and Idriss (2012) liquefaction triggering model. Though this simplified method streamlines performance-based liquefaction assessment, no sophisticated or new method can compensate for poor geotechnical subsurface investigation. If the inputs of the model (e.g. SPT blow counts, soil type, soil data, estimates of layer thicknesses, etc.) are not accurately measured, the simplified model will not likely provide accurate estimates of liquefaction hazard.

It is important to note that this approach is not meant to replace the Mayfield et al. (2010) simplified approach, which is based in the Cetin et al. (2004) liquefaction triggering model. Rather, the simplified approach provided in this thesis is meant to be performed in tandem with and to complement the Mayfield et al. approach. Now practicing engineers can compare simplified performance-based estimates of both the Cetin et al. (2004) and Boulanger and Idriss (2012) models. Although it is not within the scope of this thesis to compare the two models, such a comparison could be beneficial to engineers who may want the results of a second simplified procedure to confirm or refute the results of another simplified procedure. This sort of comparison is now possible.

In summary, the simplified procedure developed in this research removes the difficulty of the full performance-based procedure while still providing reasonably close estimates of a full performance-based analysis. Thus, performance-based methods of liquefaction assessment are now more accessible to practicing engineers on routine projects.

REFERENCES

Abrahamson, N., and Silva, W. (2008). "Summary of the Abrahamson & Silva NGA Ground-Motion Relations," *Earthquake Spectra*: February 2008, Vol. 24, No. 1, pp. 67-97.

Alarcon-Guzman, A., Leonards, A., and Chameau, J.L. (1988). "Undrained monotonic and cyclic strength of sands," *Journal of Geotechnical Engineering,* ASCE, Vol. 114, No. 10, pp. 1089-1108.

Ambraseys, N.N. (1988). "Engineering Seismology," *Earthquake Engineering and Structural Dynamics*, Vol. 17, pp.1-105.

American Association of State Highway and Transportation Officials. (2014). *AASHTO LRFD Bridge Design Specifications, 7th Ed.*, ISBN: 1-56051-592-0, AASHTO, Washington, D.C.

American Society of Civil Engineers. (2013). *Minimum Design Loads for Buildings and Other Structures (ASCE Standard ASCE/SEI 7-10, third printing)*, ISBN: 978-0-7844-1085-1, ASCE, Reston, VA.

Ancheta, T.D., Darragh, R.B., Stewart, J.P., Seyhan, E., Silva, W.J., Chiou, B. S.-J., Wooddell, K.E., Graves, R. W., Kottke, A.R., Boore, D.M., Kishida, T., and Donahue, J.L. (2014). "NGA-West2 Database," *Earthquake Spectra*: Vol. 30, No. 3, pp. 989-1005.

Andrus, R. D., Piratheepan, P., Ellis, B. S., Zhang, J., & Juang, C. H. (2004). "Comparing liquefaction evaluation methods using penetration-V S relationships." *Soil Dynamics and Earthquake Engineering*, 24(9), 713-721.

Assimaki, D. and Jeong, S. (2013). "Ground-motion observations at Hotel Montana during the M7.0 2010 Haiti earthquake: topography or soil amplification?" *Bulletin of the Seismological Society of America*, Vol. 103, No. 5, pp. 2577-2590.

Atkinson, G.M. and Boore, D.M. (2003). "Empirical ground-motion relations for subduction-zone earthquakes and their application to Cascadia and other regions." *Bulletin of the Seismological Society of America*, Vol. 93, No. 4, p. 1703-1729.

Bardet, J., Tobita, T., Mace, N. and Hu, J. (2002) "Regional Modeling of Liquefaction-Induced Ground Deformation," *Earthquake Spectra*: Vol. 18, No. 1, pp. 19-46.

Bartlett, S. and Youd, T. (1995). "Empirical Prediction of Liquefaction-Induced Lateral Spread." *J. Geotech. Engrg*., 121(4), 316–329.

Baska, D.A. (2002). "An analytical/empirical model for prediction of lateral spread displacements," *PhD Dissertation*, 2002. University of Washington.

Baziar, M. H., & Nilipour, N. (2003). "Evaluation of liquefaction potential using neural-networks and CPT results." *Soil Dynamics and Earthquake Engineering*, 23(7), 631-636.

Been, K. and Jeffries, M.G. (1985). "A state parameter for sands," *Geotechnique*, Vol. 35, No. 2, pp. 99-112.

Boore, D.M., and Atkinson, G.M. (2008). "Ground-Motion Prediction Equations for the Average Horizontal Component of PGA, PGV, and 5%-Damped PSA at Spectral Periods between 0.01 s and 10.0 s," *Earthquake Spectra*: February 2008, Vol. 24, No. 1, pp. 99-138.

Boore, D.M., Joyner, W.B., and Fumal, T.E. (1993). "Estimation of response spectra and peak accelerations from western North America earthquakes: An interim report." *Open-File-Report 93-509,* U.S. Geological Survey, Reston, Virginia, pp. 72.

Boulanger, R. and Idriss, I. (2007). "Evaluation of Cyclic Softening in Silts and Clays." J. Geotech. Geoenviron. Eng., 133(6), 641–652

Boulanger, R. W., and Idriss, I. M. (2012). "Probabilistic standard penetration test-based liquefaction-triggering procedure." *J. Geotech. Geoenviron. Eng*., 10.1061/(ASCE)GT.1943-5606.0000700, 1185–1195.

Boulanger, R. W., and Idriss, I. M. (2014). "CPT and SPT based liquefaction triggering procedures." *Rep. UCD/CGM-14/01*, Dept. of Civil and Environmental Engineering, Univ. of California–Davis, Davis, CA.

Boulanger, R. W., & Idriss, I. M. (2015). "Magnitude scaling factors in liquefaction triggering procedures." *Soil Dynamics and Earthquake Engineering*.

Bray, J.D. and Rodriguez-Marek, A. (2004). "Characterization of forward-directivity ground motions in the near-fault region," *Soil Dynamics and Earthquake Engineering*: Vol 24, No. 11, p. 815-828.

Bray, J.D. and Sancio, R.B. (2006). "Assessment of the Liquefaction Susceptibility of Fine-Grained Soils." *J. Geotech. Geoenviron. Eng*. Vol 132, No. 9. p 1165 – 1177

Campbell, K.W., and Bozorgnia, Y. (2008). "NGA Ground Motion Model for the Geometric Mean Horizontal Component of PGA, PGV, PGD and 5% Damped Linear Elastic Response Spectra for Periods Ranging from 0.01 to 10 s," *Earthquake Spectra*: February 2008, Vol. 24, No. 1, pp. 139-171.

Cao, Z.Z..; Youd, T.L.; and Yuan X.M. (2011). "Gravelly soils that liquefied during 2008 Wenchuan, China earthquake, $M_s = 8.0$." *Soil Dynamics and Earthquake Engineering* 31(8):1132-1143.

Carraro, J., Bandini, P., and Salgado, R. (2003). “Liquefaction Resistance of Clean and Nonplastic Silty Sands Based on Cone Penetration Resistance.” *J. Geotech. Geoenviron. Eng.*, 129(11), 965–976.

Casagrande, A. (1936). “Characteristics of cohesionless soils affecting the stability of slopes and earth fills,” *Journal of the Boston Society of Civil Engineers*, reprinted in *Contributions to Soil Mechanics*, Boston Society of Civil Engineers, 1940, pp 257-276.

Castro, G. (1969). “Liquefaction of sands,” *Harvard Soil Mechanics Series 87*, Harvard University, Cambridge Massachusetts.

Castro, G. and Poulos, S.J. (1977). “Factors affecting liquefaction and cyclic mobility,” *Journal of the Geotechnical Engineering Division*, ASCE, Vol. 106, No. GT6, pp. 501-506.

Cetin, K. O., et al. (2004). “Standard penetration test-based probabilistic and deterministic assessment of seismic soil liquefaction potential.” *J. Geotech. Geoenviron. Eng.*, 10.1061/(ASCE)1090-0241(2004)130:12(1314), 1314–1340.

Cetin, K., Bilge, H., Wu, J., Kammerer, A., and Seed, R. (2009). ”Probabilistic Model for the Assessment of Cyclically Induced Reconsolidation (Volumetric) Settlements.” *J. Geotech. Geoenviron. Eng.*, 135(3), 387–398.

Chiou, B. S-J., and Youngs, R.R. (2008). “An NGA Model for the Average Horizontal Component of Peak Ground Motion and Response Spectra,” *Earthquake Spectra*: February 2008, Vol. 24, No. 1, pp. 173-215.

Cornell, C.A., and Krawinkler, H. (2000). “Progress and challenges in seismic performance assessment.” *PEER News,* April, 1-3.

Deierlein, G.G., Krawinkler, H., and Cornell, C.A. (2003). “A framework for performance-based earthquake engineering.” *Proc.*, *2003 Pacific Conference on Earthquake Engineering*, Wellington, New Zealand. Paper No. 140.

Delphine, D.F. and Nyst, M. (2015). “Building time-dependent earthquake recurrence models for probabilistic risk computations.” *Bulletin of the Seismological Society of America*.

Dobry, R., and Ladd, R. S. (1980). Discussion to "Soil liquefaction and cyclic mobility evaluation for level ground during earthquakes," by H.B. Seed and "Liquefaction potential: science versus practice," by R.B. Peck. Journal of Geotechnical Engineering, 106(GT6), 720-724.

Dobry, R., Ladd, R. S., Yokel, F. Y., Chang, R. M., and Powell, D. (1982). Prediction of pore water pressure buildup and liquefaction of sands during earthquake by the cyclic strain method. NBS Building Science Series 138, 150 pp. Gaithersburg, Maryland: National Bureau of Standards.

Dobry, R., Mohamad, R., Dakoulas, P., and Gazetas, G. (1984). Liquefaction evaluation of earth dams - a new approach. Proceedings, 8th world Conference on Earthquake Engineering, 3, 333-340.

Donahue, J.L. and Abrahamson, N.A. (2014). "Simulation-Based Hanging Wall Effects," *Earthquake Spectra*: Vol. 30, No. 3, pp. 1269-1284.

Douglas, B. J., Olsen, R. S., & Martin, G. R. (1981). "Evaluation of the cone penetrometer test for SPT liquefaction assessment." *Proceedings, In Situ Testing to Evaluate Liquefaction Susceptibility*. New York, New York: ASCE.

Ekstrom, L.T., and Franke, K.W. (2015) "A Simplified Procedure for the Performance-Based Prediction of Lateral Spread Displacements," *J. Geotech. Geoenviron. Eng.* ASCE (under review, publication pending).

ESRI (2011). ArcGIS Desktop: Release 10. Redlands, CA: Environmental Systems Research Institute.

ESRI Resource Center. "Comparing interpolation methods." *ArcGIS Help 10.1*. http://resources.arcgis.com/en/help/main/10.1/index.html#//009z000000z4000000 (accessed February 19, 2015).

Faris, A. T. (2004). "Probabilistic models for engineering assessment of liquefaction-induced lateral spreading displacements," *PhD Dissertation*, 2004. University of California, Berkeley.

Finn, W. D., Bransby, P.L., and Pickering, D.J. (1970). "Effect of strain history on liquefaction of sand." *Journal of the Soil Mechanics and Foundations Division* 96.6: 1917-1934.

Finn, W. D. (1991). "Assessment of liquefaction potential and post-liquefaction behavior on earth structures: Developments 1981-1991." (State-of-the-art paper). *Proceedings, 2nd International Conference on Recent Advances in Geotechnical Engineering and Soil Dynamics*, 3, 1833-1850. St. Louis, Missouri.

Franke, K. and Kramer, S. (2014). "Procedure for the Empirical Evaluation of Lateral Spread Displacement Hazard Curves." *J. Geotech. Geoenviron. Eng*., 140(1), 110–120.

Franke, K.W. and Wright, A.D. (2013). "An alternative performance-based liquefaction initiation procedure for the standard penetration test." *Geo-Congress 2013: Stability and Performance of Slopes and Embankments III*, ASCE GSP 231, 846-849.

Franke, K., Wright, A., and Ekstrom, L. (2014a). "Comparative Study between Two Performance-Based Liquefaction Triggering Models for the Standard Penetration Test." *J. Geotech. Geoenviron. Eng.* , 10.1061/(ASCE)GT.1943-5606.0001094 , 04014010.

Franke, K.W., Mayfield, R.T., and Wright, A.D. (2014b). "Simplified uniform hazard liquefaction analysis for bridges." *Trans. Research Record*, 2407, 47-55, DOI: 10.3141/2407-05.

Franke, K.W., Wright, A.D., and Ekstrom, L.T. (2014c). "Comparative study between two performance-based liquefaction triggering models for the standard penetration test." *J. Geotech. Geoenviron. Eng.*, 140(5), DOI: 10.1061/(ASCE)GT.1943-5606.0001094.

Franke, K.W., Wright, A.D., and Hatch, C.K. (2014d). "PBLiquefY: A new analysis tool for the performance-based evaluation of liquefaction triggering." *Proc., 10th Nat. Conf. Earthquake Eng.*, Paper No. 87, EERI, Oakland, CA.

Gao, Y., Zhang, N., Li, D., Liu, H., Cai, Y., and Wu, Y. (2012). "Effects of topographic amplification induced by a U-shaped canyon on seismic waves." *Bulletin of the Seismological Society of America*, Vol. 102, No. 4, p. 1748-1763.

GEER (2011). "Geotechnical Reconnaissance of the Christchurch, New Zealand Earthquake," Report No. GEER-027.

GEER (2010). "Geotechnical Reconnaissance of the 2010 Darfield (New Zealand) Earthquake," Report No. GEER-024.

GEER (2014). "Geotechnical Aspects of April 1, 2014 M8.2 Iquique, Chile Earthquake," Report No. GEER-038, Version 1.2.

Graves, R.W., Pitarka, A., and Somerville, P.G. (1998). "Ground-motion amplification in the Santa Monica area: effects of shallow basin-edge structure," *Bulletin of the Seismological Society of America,* Vol. 88, No. 5, pp. 1224-1242.

Green, R. A. (2001). *Energy-based evaluation and remediation of liquefiable soils*. Doctoral dissertation, Virginia Tech.

Hanzawa, H., Itoh, Y., and Suzuki, K. (1979). "Shear characteristics of a quick sand in the Arabian Gulf," *Soils and Foundations,* Vol. 19, No. 4, pp. 1-15

Huang, Y.-M. (2008). "Performance-based design and evaluation for liquefaction-related seismic hazards." *Ph.D. Dissertation*, University of Washington, Seattle, WA.

Idriss, I.M. (2008). "An NGA Empirical Model for Estimating the Horizontal Spectral Values Generated By Shallow Crustal Earthquakes," *Earthquake Spectra*: February 2008, Vol. 24, No. 1, pp. 217-242.

Idriss, I.M. and Boulanger, R.W. (2006). "Semi-empirical procedures for evaluating liquefaction potential during earthquakes" *11th International Conference on Soil Dynamics and Earthquake Engineering, ICSDEE, Part II.* Vol 26, Issues 2-4, p. 115-130.

Idriss, I.M., and Boulanger, R.W. (2008). *Soil liquefaction during earthquakes.* Monograph MNO-12, Earthquake Engineering Research Institute, Oakland, CA 261 pp.

Idriss, I. M., and Boulanger, R. W. (2010). "SPT-based liquefaction triggering procedures." Rep. UCD/CGM-10/02, Dept. of Civil and Environmental Engineering, Univ. of California–Davis, Davis, CA.

International Building Code. (2014). *2015 International Building Code*, ISBN: 978-1-60983-468-5, International Code Council, Inc., Country Club Hills, IL.

Ishihara, K. and Yoshimine, M. (1992). "Evaluation of settlements in sand deposits following liquefaction during earthquakes," *Soils and Foundations*, Vol. 32, No. 1, p. 173-188.

Juang, C. H., Ching, J., Luo, Z., & Ku, C. S. (2012). "New models for probability of liquefaction using standard penetration tests based on an updated database of case histories." *Engineering Geology*, 133, 85-93.

Kayen, R.E., Mitchell, J.K., Seed, R.B., Lodge, A., Nishio, S., and Coutinho, R. (1992). "Evaluation of SPT-, CPT-, and shear wave-based methods for liquefaction potential assessment using Loma Prieta data." *Technical Report NCEER*. Vol. 1. No. 92-0019. US National Center for Earthquake Engineering Research (NCEER), 177-204.

Kayen, R.E., and Mitchell, J.K. (1997). "Assessment of liquefaction potential during earthquakes by Arias intensity." *Journal of Geotechnical and Geoenvironmental Engineering*, 123.12: 1162-1174.

Kayen, R., Moss, R., Thompson, E., Seed, R., Cetin, K., Kiureghian, A., Tanaka, Y., and Tokimatsu, K. (2013). "Shear-Wave Velocity–Based Probabilistic and Deterministic Assessment of Seismic Soil Liquefaction Potential." *J. Geotech. Geoenviron. Eng*., 139(3), 407–419.

Kramer, S. L. (1996). *Geotechnical Earthquake Engineering*, Prentice Hall, Upper Saddle River, New Jersey.

Kramer, S. L. (2008). "Evaluation of liquefaction hazards in Washington State." WSDOT Report *WA-RD 668.1*, 152 pp.

Kramer, S. L., and Mayfield, R. T. (2007). "Return period of soil liquefaction." *J. Geotech. Geoenviron. Eng*., 10.1061/(ASCE)1090-0241 (2007)133:7(802), 802–813.

Kramer, S.L., Franke, K.W., Huang, Y., and Baska, D.A. (2007). "Performance-Based Evaluation of Lateral Spreading Displacement," *4th International Conference on Earthquake Geotechnical Engineering*. Paper No. 1208.

Krawinkler, H. (2002). "A general approach to seismic performance assessment." *Proc., Int. Conf. on Advances in New Challenges in Earthquake Engineering Research*, ICANCEER, Hong Kong.

Ku, C. S., Lee, D. H., & Wu, J. H. (2004). "Evaluation of soil liquefaction in the Chi-Chi, Taiwan earthquake using CPT." *Soil Dynamics and Earthquake Engineering*, 24(9), 659-673.

Ladd, R. S. (1974). "Specimen preparation and liquefaction of sands." *Journal of Geotechnical and Geoenvironmental Engineering,* 100.Proc. Paper 10857 Proceeding.

Li, J., Heap, A. (2011). "A review of comparative studies of spatial interpolation methods in environmental sciences: Performance and impact factors." *Ecological Informatics*, 6(3-4): 228-241.

Liao, S., Veneziano, D., and Whitman, R. (1988). “Regression Models For Evaluating Liquefaction Probability.” *J. Geotech. Engrg.*, 114(4), 389–411.

Liu, C. and Xu, J. (2013). “Experimental Study on the Effects of Initial Conditions on Liquefaction of Saturated and Unsaturated Sand.” *International Journal of Geomechanics*, 10.1061/(ASCE)GM.1943-5622.0000350 , 04014100.

Luo, W., Taylor, C., and Parker, S. R. (2008). “A comparison of spatial interpolation methods to estimate continuous wind speed surfaces using irregularly distributed data from England and Wales.” *Int. J. Climatol.,* 28: 947-959.

Marchetti, S. (1982). “Detection of liquefiable sand layers by means of quasi-static penetration tests.” In *Proc. 2nd European Symposium on Penetration Testing*, pp. 689-695.

Mayfield, R. T. (2007). *The return period of soil liquefaction*. Doctoral dissertation, University of Washington.

Mayfield, R. T., Kramer, S. L., and Huang, Y.-M. (2010). “Simplified approximation procedure for performance-based evaluation of liquefaction potential.” *J. Geotech. Geoenviron. Eng.*, 10.1061/(ASCE) GT.1943-5606.0000191, 140–150.

Mitchell, J. K., and Tseng, D-J. (1990). “Assessment of liquefaction potential by cone penetration resistance.” *Proceedings of the HB Seed Memorial Symposium*, Bi Tech Publishing. Vol. 2.

Moehle, J. and Deierlein, G.G. (2004). “A framework methodology for performance-based earthquake engineering.” *Proceedings, 13th World Conference on Earthquake Engineering, Vancouver B.C., Canada.* Paper No. 679.

Moss, R. E., Seed, R. B., Kayen, R. E., Stewart, J. P., Der Kiureghian, A., & Cetin, K. O. (2006). “CPT-based probabilistic and deterministic assessment of in situ seismic soil liquefaction potential.” *Journal of Geotechnical and Geoenvironmental Engineering*, 132(8), 1032-1051.

National Oceanic and Atmospheric Administration, NOAA. “Van Norman Dam (Lower San Fernando Dam (1971),” *https://www.ngdc.noaa.gov/hazardimages/picture/show/404* (accessed April 10, 2015).

Ohsaki, Y. (1970) "Effects of sand compaction on liquefaction during the Tokachioki earthquake." *Soils and Foundations*, 10.2: 112-128.

Olson, S.M. and Stark, T.D. (2002). “Liquefied strength ratio from liquefaction flow failure case histories,” *Canadian Geotechnical Journal*, 39(3): 629-647.

Parsons, T. (2008). “Earthquake recurrence on the south Hayward fault is most consistent with a time dependent, renewal process.” *Geophysical Research Letters*, Vol. 35, No. 21.

Pilz, M., Parolai, S., Stupazzini, M., Paolucci, R., and Zschau, J. (2011). "Modelling basin effects on earthquake ground motion in the Santiago de Chile basin by a spectral element code." *Geophysical Journal International*, Vol. 187, No. 2, pp. 929-945.

Poulos, S.J. (1981). "The steady state of deformation," *J. Geotech. Geoenviron. Eng.*, Vol 107, Issue GT5, pp. 553-562.

Poulos, S.J., Castro, G., and France, J.W. (1985). "Liquefaction Evaluation Procedure," *Journal of Geotechnical Engineering*, Vol. 111, No. 6, pp. 772-792.

Pyke, R., Chan, C.K., and Seed, H.B. (1974). Settlement and liquefaction of sands under multi-directional shaking. Earthquake Engineering Research Center, University of California.

Reyna, F., & Chameau, J. L. (1991). "Dilatometer based liquefaction potential of sites in the Imperial Valley." In *Second International Conference on Recent Advances in Geotechnical Earthquake Engineering and Soil Dynamics,* St. Louis, Missouri.

Robertson, P. and Campanella, R. (1985). "Liquefaction Potential of Sands Using the CPT." *J. Geotech. Engrg.*, 111(3), 384–403.

Robertson, P. K., & Campanella, R. G. (1986). "Estimating liquefaction potential of sands using the flat dilatometer." *Geotechnical Testing Journal*, 9(1), 38-40.

Running, D. L. (1996). *An energy-based model for soil liquefaction*. Doctoral dissertation, Washington State University.

Seed, H.B. (1980). Closure to soil liquefaction and cyclic mobility evaluation for level ground during earthquakes. *Journal of Geotechnical Engineering Division*, 106(GT6), 724.

Seed, H.B., and De Alba, P. (1986). "Use of SPT and CPT tests for evaluating the liquefaction resistance of soils." *Proceedings, In Situ '86*. ASCE.

Seed, R.B. and Harder, L.F. (1990). "SPT-based analysis of cyclic pore pressure generation and undrained residual strength," in J.M. Duncan ed., *Proceedings, H. Bolton Seed Memorial Symposium,* University of California, Berkeley, Vol. 2, pp. 351-376.

Seed, H.B. and Idriss, I.M. (1971). "Simplified procedure for evaluating soil liquefaction potential," *J. Soil Mech. and Found. Div.*, 97(SM9), p. 1249-1273.

Seed, H. B., and Peacock, W.H. (1971). "Test procedures for measuring soil liquefaction characteristics." *Journal of the Soil Mechanics and Foundations Division*, 97.8: 1099-1119.

Somerville, P.G., Smith, N.F., Graves, R.W., and Abrahamson, N.A. (1997). "Modification of empirical strong ground motion attenuation relations to include the amplitude and duration effects of rupture directivity," *Seismological Research Letters*, Vol. 68, No. 1, p. 199-222.

Stewart, J. P., & Whang, D. H. (2003). "Simplified procedure to estimate ground settlement from seismic compression in compacted soils," In *Proceedings 2003 Pacific Conference on Earthquake Engineering, Christchurch, New Zealand, Paper* (Vol. 46).

Stewart, J.P., Liu, A.H., and Choi, Y. (2003). "Amplification factors for spectral acceleration in tectonically active regions." *Bull. Seismol. Soc. Am.*, 93(7): 332-352.

Stokoe, K. H., Roesset, J. M., Bierschwale, J. G., and Aouad, M. (1988). "Liquefaction potential of sands from shear wave velocity." In *Proceedings, 9th World Conference on Earthquake Engineering,* Vol. 13, pp. 213-218.

Suzuki, Y., Tokimatsu, K., and Koyamada, K. (2003). "Correlation between soil liquefaction during earthquakes and CPT data." *Journal of Structural and Construction Engineering*(571).

Tokimatsu, K. and Seed, H. (1987). "Evaluation of Settlements in Sands Due to Earthquake Shaking." *J. Geotech. Eng*., 113(8), 861–878.

Tokimatsu, K., Kuwayama, S., & Tamura, S. (1991). "Liquefaction potential evaluation based on Rayleigh wave investigation and its comparison with field behavior." In *Second International Conference on Recent Advances in Geotechnical Earthquake Engineering and Soil Dynamics*. St. Louis, Missouri.

Toprak, S., Holzer, T. L., Bennett, M. J., and Tinsley, J. C. (1999). "CPT-and SPT-based probabilistic assessment of liquefaction potential." In *Proc., 7th US–Japan Workshop on Earthquake Resistant Design of Lifeline Facilities and Countermeasures against Liquefaction*.

Travasarou, T., Bray, J.D., and Abrahamson, N.A. (2003). "Empirical attenuation relationship for Arias Intensity," *Earthquake Engng Struct. Dyn.*, 32:1133-1155.

Tsukamoto, Y.; Kawabe, S.; Matsumoto, J.; and Hagiwara, S. (2014). "Cyclic Resistance of Two Unsaturated Silty Sands against Soil Liquefaction" *Soils and Foundations.* Vol 54, Issue 6, P 1094-1103.

United States Geological Survey, USGS (1989). *The Severity of an Earthquake*, a U. S. Geological Survey General Interest Publication. U.S. GOVERNMENT PRINTING OFFICE: 1989-288-913.

USGS and Montana Bureau of Mines and Geology. (2006). "Quaternary Fault and Fold Database of the United States." http://earthquake.usgs.gov/hazards/qfaults/ (date accessed: January 21, 2015).

USGS. (2008). "USGS 2008 interactive deaggregation." https://geohazards.usgs.gov/deaggint/2008/ (accessed March 26, 2014).

USGS. (2008). "2008 Seismic Hazard Map (PGA, 2% in 50 years)" http://earthquake.usgs.gov/hazards/products/graphic2pct50.jpg (accessed Sept 2, 2014).

Ulmer, K.J. and Franke, K.W. (2015). “A Modified Performance-Based Liquefaction Triggering Procedure using Liquefaction Loading Maps.” *J. Geotech. Geoenviron. Eng*., (under review, publication pending).

Unno, T.; Kazama, M..; Uzuoka, R.; and Sento, N. (2008). “Liquefaction of Unsaturated Sand Considering the Pore Air Pressure and Volume Compressibility of the Soil Particle Skeleton.” *Soils and Foundations*, Vol. 48, No. 1, pp 87-99.

Vasquez-Herrera, A., and Dobry, R. (1988). The behavior of undrained contractive sand and its effect on seismic liquefaction flow failures of earth structures. Report to the U.S. Army Corps of Engineers, 510 pp. Troy, New York: Renssalaer Polytechnic Institute.

Wang, W. (1979). *Some Findings in Soil Liquefaction*. Water Conservancy and Hydroelectric Power Scientific Research Institute, Beijing, China.

Wells, D.L., Coppersmith, K.J. (1994). New empirical relationships among magnitude, rupture length, rupture width, rupture area, and surface displacement. *Bulletin of the Seismological Society of America*. 84(4), 974-1002.

Wright, A.D. (2013). “Comparison of performance-based liquefaction initiation analyses between multiple probabilistic liquefaction models using the standard penetration test.” *M.S. Thesis*, 2013, Brigham Young University, Provo.

Vaid, Y.P., and Chern, J.C. (1985). “Cyclic and monotonic undrained response of saturatedy sands,” in V. Khosla ed., I*Advances in the Art of Testing Soils under Cyclic Conditions,* ASCE, New York, pp. 120-147.

Youd, T.L. and Hoose, S.N. (1977). “Liquefaction Susceptibility and Geologic Setting”, Proceedings of 6th World Conference on Earthquake Engineering, New Delhi, India. Volume 6, p 37-42

Youd, T.L. (1984). “Recurrence of liquefaction at the same site,” *Proceedings, 8th World Conference on Earthquake Engineering*, Vol. 3, pp. 231-238.

Youd, T. L., and Noble, S. K. (1997). *Liquefaction Criteria Based on Statistical and Probabilistic Analyses* (Technical Report NCEER-97).

Youd, T., Idriss, I., Andrus, R., Arango, I., Castro, G., Christian, J., Dobry, R., Finn, W., Harder, L., Jr., Hynes, M., Ishihara, K., Koester, J., Liao, S., Marcuson, W., III, Martin, G., Mitchell, J., Moriwaki, Y., Power, M., Robertson, P., Seed, R., and Stokoe, K., II (2001). “Liquefaction Resistance of Soils: Summary Report from the 1996 NCEER and 1998 NCEER/NSF Workshops on Evaluation of Liquefaction Resistance of Soils.” *J. Geotech. Geoenviron. Eng*., 127(10), 817–833.

Youd, T., Hansen, C., and Bartlett, S. (2002). ”Revised Multilinear Regression Equations for Prediction of Lateral Spread Displacement.” *J. Geotech. Geoenviron. Eng*., 128(12), 1007–1017.

Youngs, R.R., Chiou, S.-J., Silva, W.J., and Humphrey, J.R. (1997). "Strong ground motion attenuation relationships for subduction zone earthquakes." *Seismological Research Letters,* Vol. 68, No. 1, p. 58-73.

Zhao, J. X., Zhang, J., Asano, A., Ohno, Y., Oouchi, T., Takahashi, T., Ogawa, H., Irikura, K., Thio, H.K., Somerville, P.G., Fukushima, Ya., and Fukushima, Yo. (2006). "Attenuation relations of strong ground motion in Japan using site classification based on predominant period." *Bulletin of the Seismological Society of America*, Vol. 96, No. 3, p. 898-913.

APPENDIX A: SUPPLEMENTARY VALIDATION DATA

The following tables are supplementary to the validation results of this report but are too lengthy to include in the body of the text. Table A-1 displays the results of the simplified liquefaction triggering procedure while Table A-2 displays the results of the full probabilistic liquefaction triggering procedure.

Depth conversions to U.S. Customary Units: 2.5 m (8.20 ft), 3.5 m (11.48 ft), 4.5 m (14.76 ft), 5.5 m (18.04 ft), 6.5 m (21.33 ft), 7.5 m (24.61 ft), 8.5 m (27.89 ft), 9.5 m (31.17 ft), 10.5 m (34.45 ft), 11.5 m (37.73 ft)

Table A-1: Results from Simplified Liquefaction Triggering Procedure

			T_R = 1033 Simple PB (Idriss & Boulanger)				T_R = 475 Simple PB (Idriss & Boulanger)				T_R = 2475 Simple PB (Idriss & Boulanger)			
	Depth (m)	$N_{1,60,cs}$ site	N_{req}	$\%CSR^{site}$	FS_L	P_L	N_{req}	$\%CSR^{site}$	FS_L	P_L	N_{req}	$\%CSR^{site}$	FS_L	P_L
Butte	2.5	13.78	4.568	9.528	1.747	0.022	1.000	7.434	2.375	0.002	8.740	12.467	1.335	0.148
	3.5	15.62	6.554	10.867	1.691	0.029	2.029	7.994	2.299	0.001	10.965	14.223	1.292	0.177
	4.5	16.95	7.780	11.749	1.681	0.030	3.144	8.642	2.285	0.001	12.344	15.377	1.284	0.183
	5.5	19.87	8.522	12.301	1.892	0.011	3.811	9.049	2.572	0.000	13.178	16.104	1.445	0.092
	6.5	21.47	9.030	12.688	2.021	0.006	4.266	9.335	2.748	0.000	13.749	16.615	1.544	0.059
	7.5	23.12	9.356	12.940	2.213	0.002	4.553	9.518	3.008	0.000	14.111	16.945	1.690	0.029
	8.5	24.83	9.553	13.094	2.487	0.001	4.729	9.633	3.381	0.000	14.336	17.153	1.899	0.010
	9.5	27.79	9.685	13.197	3.238	0.000	4.846	9.709	4.401	0.000	14.484	17.291	2.471	0.001
	10.5	29.76	9.772	13.265	4.036	0.000	4.921	9.757	5.486	0.000	14.581	17.382	3.080	0.000
	11.5	31.81	9.848	13.325	5.346	0.000	4.990	9.803	7.268	0.000	14.669	17.465	4.079	0.000
Charleston	2.5	13.78	18.765	21.832	0.762	0.836	6.850	11.076	1.503	0.071	26.706	38.365	0.434	0.999
	3.5	15.62	21.090	25.043	0.734	0.868	9.023	12.683	1.449	0.090	28.077	44.043	0.417	0.999
	4.5	16.95	22.393	27.241	0.725	0.877	10.406	13.769	1.434	0.097	28.842	47.955	0.412	0.999
	5.5	19.87	23.158	28.716	0.810	0.776	11.284	14.485	1.606	0.044	29.299	50.607	0.460	0.997
	6.5	21.47	23.688	29.836	0.860	0.708	11.919	15.016	1.708	0.027	29.620	52.638	0.487	0.995
	7.5	23.12	24.052	30.657	0.934	0.597	12.362	15.393	1.860	0.013	29.846	54.151	0.529	0.989
	8.5	24.83	24.312	31.273	1.041	0.442	12.676	15.664	2.079	0.004	30.011	55.306	0.589	0.972
	9.5	27.79	24.519	31.781	1.344	0.143	12.921	15.878	2.691	0.000	30.145	56.276	0.759	0.840
	10.5	29.76	24.691	32.215	1.662	0.033	13.120	16.053	3.335	0.000	30.259	57.122	0.937	0.593
	11.5	31.81	24.855	32.643	2.182	0.002	13.310	16.221	4.392	0.000	30.368	57.957	1.229	0.228
Eureka	2.5	13.78	30.898	62.315	0.267	1.000	26.775	38.616	0.431	0.999	33.360	92.041	0.181	1.000
	3.5	15.62	31.855	71.732	0.256	1.000	28.158	44.432	0.414	0.999	34.124	105.987	0.173	1.000
	4.5	16.95	32.412	78.334	0.252	1.000	28.938	48.494	0.407	0.999	34.576	115.783	0.171	1.000
	5.5	19.87	32.757	82.929	0.281	1.000	29.413	51.310	0.454	0.998	34.860	122.624	0.190	1.000
	6.5	21.47	33.008	86.554	0.296	1.000	29.754	53.520	0.479	0.996	35.069	128.038	0.200	1.000
	7.5	23.12	33.193	89.368	0.320	1.000	30.000	55.226	0.518	0.991	35.223	132.260	0.216	1.000
	8.5	24.83	33.334	91.620	0.355	1.000	30.187	56.581	0.576	0.977	35.342	135.660	0.240	1.000
	9.5	27.79	33.453	93.596	0.457	0.998	30.343	57.761	0.740	0.862	35.443	138.653	0.308	1.000
	10.5	29.76	33.559	95.388	0.561	0.981	30.479	58.825	0.910	0.633	35.533	141.378	0.379	1.000
	11.5	31.81	33.661	97.183	0.733	0.869	30.611	59.888	1.190	0.265	35.620	144.113	0.494	0.995
Memphis	2.5	13.78	19.764	23.120	0.720	0.882	8.898	12.588	1.322	0.157	25.676	34.955	0.476	0.996
	3.5	15.62	22.022	26.578	0.692	0.909	11.242	14.450	1.272	0.193	27.188	40.195	0.457	0.998
	4.5	16.95	23.285	28.978	0.681	0.917	12.754	15.731	1.255	0.206	28.034	43.841	0.450	0.998
	5.5	19.87	24.039	30.628	0.760	0.839	13.730	16.598	1.402	0.111	28.543	46.355	0.502	0.994
	6.5	21.47	24.570	31.908	0.804	0.785	14.452	17.261	1.486	0.076	28.906	48.315	0.531	0.989
	7.5	23.12	24.946	32.882	0.871	0.691	14.974	17.755	1.613	0.042	29.166	49.812	0.575	0.977
	8.5	24.83	25.225	33.645	0.968	0.547	15.361	18.129	1.796	0.017	29.361	50.991	0.639	0.947
	9.5	27.79	25.454	34.299	1.246	0.214	15.681	18.444	2.317	0.001	29.523	52.009	0.822	0.761
	10.5	29.76	25.652	34.882	1.535	0.061	15.955	18.718	2.860	0.000	29.663	52.918	1.012	0.483
	11.5	31.81	25.841	35.461	2.009	0.006	16.220	18.986	3.752	0.000	29.799	53.825	1.324	0.156

Table A-1 Continued

			T_R = 1033 Simple PB (Idriss & Boulanger)				T_R = 475 Simple PB (Idriss & Boulanger)				T_R = 2475 Simple PB (Idriss & Boulanger)			
	Depth (m)	$N_{1,60,cs}$ site	N_{req}	$\%CSR^{site}$	FS_L	P_L	N_{req}	$\%CSR^{site}$	FS_L	P_L	N_{req}	$\%CSR^{site}$	FS_L	P_L
Portland	2.5	13.78	21.346	25.447	0.654	0.937	16.028	18.792	0.886	0.669	25.152	33.443	0.498	0.994
	3.5	15.62	23.426	29.272	0.628	0.954	18.582	21.609	0.851	0.721	26.736	38.474	0.478	0.996
	4.5	16.95	24.583	31.940	0.618	0.959	20.091	23.570	0.838	0.739	27.621	41.987	0.470	0.997
	5.5	19.87	25.274	33.783	0.689	0.911	21.011	24.920	0.934	0.598	28.155	44.417	0.524	0.990
	6.5	21.47	25.765	35.227	0.728	0.874	21.668	25.975	0.987	0.518	28.537	46.324	0.554	0.984
	7.5	23.12	26.116	36.336	0.788	0.805	22.137	26.780	1.069	0.405	28.812	47.790	0.599	0.968
	8.5	24.83	26.379	37.213	0.875	0.685	22.486	27.413	1.188	0.267	29.019	48.953	0.665	0.929
	9.5	27.79	26.597	37.974	1.125	0.335	22.775	27.960	1.528	0.063	29.192	49.965	0.855	0.714
	10.5	29.76	26.786	38.657	1.385	0.120	23.025	28.449	1.882	0.011	29.342	50.874	1.052	0.427
	11.5	31.81	26.968	39.341	1.811	0.016	23.265	28.937	2.462	0.001	29.488	51.785	1.376	0.125
Salt Lake City	2.5	13.78	20.465	24.103	0.691	0.909	13.594	16.475	1.010	0.485	25.979	35.895	0.464	0.997
	3.5	15.62	22.608	27.641	0.665	0.930	16.118	18.883	0.973	0.539	27.431	41.183	0.446	0.998
	4.5	16.95	23.789	30.059	0.657	0.935	17.651	20.521	0.962	0.555	28.235	44.806	0.441	0.998
	5.5	19.87	24.479	31.680	0.735	0.867	18.585	21.613	1.077	0.395	28.712	47.246	0.493	0.995
	6.5	21.47	24.955	32.906	0.779	0.816	19.242	22.432	1.143	0.314	29.044	49.099	0.522	0.990
	7.5	23.12	25.282	33.804	0.847	0.726	19.694	23.025	1.244	0.216	29.275	50.466	0.567	0.980
	8.5	24.83	25.513	34.472	0.945	0.581	20.012	23.460	1.388	0.118	29.442	51.493	0.632	0.951
	9.5	27.79	25.698	35.022	1.220	0.236	20.263	23.812	1.794	0.017	29.576	52.346	0.816	0.768
	10.5	29.76	25.851	35.491	1.508	0.069	20.470	24.109	2.220	0.002	29.687	53.078	1.009	0.488
	11.5	31.81	25.996	35.950	1.982	0.007	20.667	24.399	2.920	0.000	29.795	53.798	1.324	0.155
San Francisco	2.5	13.78	26.864	38.946	0.427	0.999	24.088	30.742	0.541	0.987	29.389	51.161	0.325	1.000
	3.5	15.62	28.240	44.826	0.410	0.999	25.811	35.367	0.520	0.991	30.490	58.910	0.312	1.000
	4.5	16.95	29.017	48.943	0.403	0.999	26.769	38.596	0.512	0.992	31.124	64.350	0.307	1.000
	5.5	19.87	29.491	51.807	0.449	0.998	27.346	40.831	0.570	0.979	31.516	68.146	0.341	1.000
	6.5	21.47	29.833	54.061	0.474	0.996	27.757	42.583	0.602	0.966	31.802	71.150	0.360	1.000
	7.5	23.12	30.081	55.810	0.513	0.992	28.053	43.931	0.652	0.939	32.011	73.488	0.390	1.000
	8.5	24.83	30.270	57.205	0.569	0.979	28.275	45.000	0.724	0.878	32.171	75.370	0.432	0.999
	9.5	27.79	30.429	58.427	0.731	0.871	28.460	45.929	0.930	0.603	32.307	77.025	0.555	0.983
	10.5	29.76	30.568	59.533	0.899	0.649	28.622	46.766	1.145	0.313	32.427	78.532	0.682	0.917
	11.5	31.81	30.702	60.642	1.175	0.280	28.777	47.602	1.497	0.073	32.544	80.043	0.890	0.663
San Jose	2.5	13.78	25.188	33.542	0.496	0.994	22.491	27.421	0.607	0.964	27.607	41.926	0.397	1.000
	3.5	15.62	26.722	38.422	0.478	0.996	24.368	31.409	0.585	0.973	28.854	48.023	0.383	1.000
	4.5	16.95	27.562	41.734	0.473	0.997	25.390	34.113	0.579	0.976	29.546	52.158	0.379	1.000
	5.5	19.87	28.051	43.924	0.530	0.989	25.981	35.900	0.648	0.941	29.953	54.892	0.424	0.999
	6.5	21.47	28.387	45.558	0.563	0.981	26.385	37.232	0.689	0.911	30.233	56.928	0.451	0.998
	7.5	23.12	28.614	46.728	0.613	0.961	26.656	38.185	0.750	0.851	30.423	58.385	0.490	0.995
	8.5	24.83	28.773	47.576	0.685	0.914	26.845	38.875	0.838	0.739	30.556	59.438	0.548	0.985
	9.5	27.79	28.895	48.252	0.886	0.670	26.991	39.425	1.084	0.386	30.659	60.278	0.709	0.893
	10.5	29.76	28.995	48.814	1.097	0.370	27.108	39.880	1.342	0.144	30.742	60.975	0.878	0.681
	11.5	31.81	29.089	49.359	1.443	0.093	27.220	40.320	1.767	0.020	30.821	61.649	1.156	0.301

Table A-1 Continued

			T_R = 1033 Simple PB (Idriss & Boulanger)				T_R = 475 Simple PB (Idriss & Boulanger)				T_R = 2475 Simple PB (Idriss & Boulanger)			
	Depth (m)	$N_{1,60,cs}$ site	N_{req}	$\%CSR^{site}$	FS_L	P_L	N_{req}	$\%CSR^{site}$	FS_L	P_L	N_{req}	$\%CSR^{site}$	FS_L	P_L
Santa Monica	2.5	13.78	23.956	30.437	0.547	0.985	20.730	24.493	0.680	0.918	27.485	41.406	0.402	0.999
	3.5	15.62	25.656	34.894	0.527	0.990	22.832	28.070	0.655	0.937	28.756	47.486	0.387	1.000
	4.5	16.95	26.586	37.933	0.521	0.991	23.985	30.504	0.647	0.942	29.465	51.641	0.382	1.000
	5.5	19.87	27.130	39.964	0.582	0.975	24.655	32.124	0.724	0.878	29.886	54.427	0.428	0.999
	6.5	21.47	27.505	41.493	0.618	0.959	25.114	33.338	0.769	0.828	30.180	56.534	0.454	0.998
	7.5	23.12	27.762	42.606	0.672	0.924	25.426	34.217	0.837	0.740	30.384	58.076	0.493	0.995
	8.5	24.83	27.944	43.427	0.750	0.851	25.644	34.860	0.934	0.597	30.529	59.225	0.550	0.985
	9.5	27.79	28.088	44.098	0.969	0.545	25.816	35.382	1.208	0.248	30.645	60.169	0.710	0.892
	10.5	29.76	28.207	44.666	1.199	0.257	25.955	35.818	1.495	0.073	30.742	60.973	0.878	0.681
	11.5	31.81	28.320	45.220	1.575	0.050	26.088	36.244	1.966	0.007	30.835	61.763	1.153	0.303
Seattle	2.5	13.78	23.208	28.820	0.578	0.976	19.016	22.145	0.752	0.849	26.908	39.111	0.426	0.999
	3.5	15.62	25.007	33.047	0.556	0.983	21.304	25.380	0.724	0.878	28.247	44.864	0.410	0.999
	4.5	16.95	25.991	35.934	0.550	0.985	22.577	27.583	0.716	0.886	28.993	48.806	0.405	0.999
	5.5	19.87	26.566	37.864	0.615	0.961	23.320	29.050	0.801	0.788	29.436	51.455	0.452	0.998
	6.5	21.47	26.964	39.323	0.652	0.939	23.830	30.151	0.851	0.720	29.745	53.465	0.480	0.996
	7.5	23.12	27.237	40.389	0.709	0.893	24.176	30.948	0.925	0.611	29.960	54.942	0.521	0.991
	8.5	24.83	27.431	41.180	0.791	0.801	24.419	31.533	1.033	0.454	30.114	56.050	0.581	0.975
	9.5	27.79	27.584	41.828	1.022	0.469	24.610	32.008	1.335	0.148	30.238	56.967	0.750	0.850
	10.5	29.76	27.711	42.380	1.263	0.200	24.765	32.406	1.652	0.035	30.342	57.752	0.927	0.608
	11.5	31.81	27.833	42.920	1.660	0.034	24.913	32.795	2.172	0.003	30.441	58.524	1.217	0.239

Table A-2: Results from Full Probabilistic Liquefaction Triggering Procedure

			T_R = 1033 Full PB (Idriss & Boulanger)				T_R = 475 Full PB (Idriss & Boulanger)				T_R = 2475 Full PB (Idriss & Boulanger)			
	Depth (m)	$N_{1,60,cs}$ site	N_{req}	$\%CSR^{site}$	FS_L	P_L	N_{req}	$\%CSR^{site}$	FS_L	P_L	N_{req}	$\%CSR^{site}$	FS_L	P_L
Butte	2.5	13.78	4.38	9.408	1.77	0.020	1	7.434	2.24	0.002	8.89	12.581	1.32	0.156
	3.5	15.62	6.29	10.682	1.72	0.025	1.62	7.767	2.37	0.001	11.09	14.325	1.28	0.184
	4.5	16.95	7.47	11.522	1.72	0.026	2.65	8.350	2.37	0.001	12.47	15.486	1.28	0.190
	5.5	19.87	8.21	12.067	1.93	0.009	3.29	8.730	2.67	0.000	13.36	16.266	1.43	0.098
	6.5	21.47	8.68	12.421	2.07	0.004	3.68	8.968	2.86	0.000	13.91	16.761	1.53	0.062
	7.5	23.12	8.94	12.619	2.27	0.002	3.88	9.092	3.15	0.000	14.27	17.092	1.68	0.031
	8.5	24.83	9.07	12.719	2.56	0.000	3.96	9.142	3.56	0.000	14.46	17.269	1.89	0.011
	9.5	27.79	9.09	12.735	3.36	0.000	3.95	9.136	4.68	0.000	14.52	17.325	2.47	0.001
	10.5	29.76	9.02	12.681	4.22	0.000	3.87	9.086	5.89	0.000	14.48	17.287	3.10	0.000
	11.5	31.81	8.9	12.589	5.66	0.000	3.73	8.999	7.92	0.000	14.37	17.185	4.15	0.000
Charleston	2.5	13.78	19.25	22.443	0.74	0.860	6.38	10.745	1.55	0.057	26.94	39.232	0.42	0.999
	3.5	15.62	21.54	25.762	0.71	0.889	8.39	12.202	1.51	0.070	28.37	45.472	0.40	0.999
	4.5	16.95	22.85	28.104	0.70	0.899	9.63	13.154	1.50	0.071	29.2	50.012	0.39	1.000
	5.5	19.87	23.68	29.819	0.78	0.815	10.42	13.781	1.69	0.029	29.75	53.497	0.44	0.999
	6.5	21.47	24.23	31.076	0.83	0.756	10.9	14.170	1.81	0.016	30.13	56.163	0.46	0.998
	7.5	23.12	24.6	31.984	0.89	0.655	11.18	14.399	1.99	0.007	30.41	58.281	0.49	0.995
	8.5	24.83	24.86	32.654	1.00	0.504	11.3	14.498	2.25	0.002	30.61	59.879	0.54	0.986
	9.5	27.79	25.03	33.108	1.29	0.179	11.31	14.507	2.95	0.000	30.76	61.127	0.70	0.902
	10.5	29.76	25.13	33.381	1.60	0.044	11.22	14.432	3.71	0.000	30.86	61.984	0.86	0.702
	11.5	31.81	25.19	33.547	2.12	0.003	11.06	14.300	4.98	0.000	30.94	62.684	1.14	0.322
Eureka	2.5	13.78	30.81	61.553	0.27	1.000	27.15	40.044	0.42	0.999	33.2	89.482	0.19	1.000
	3.5	15.62	31.88	72.010	0.26	1.000	28.59	46.600	0.39	1.000	34.08	105.096	0.18	1.000
	4.5	16.95	32.55	80.128	0.25	1.000	29.44	51.481	0.38	1.000	34.66	117.738	0.17	1.000
	5.5	19.87	32.98	86.133	0.27	1.000	30	55.225	0.42	0.999	35.02	126.741	0.18	1.000
	6.5	21.47	33.33	91.557	0.28	1.000	30.4	58.203	0.44	0.998	35.34	135.607	0.19	1.000
	7.5	23.12	33.58	95.759	0.30	1.000	30.7	60.622	0.47	0.997	35.58	142.853	0.20	1.000
	8.5	24.83	33.78	99.337	0.33	1.000	30.93	62.596	0.52	0.991	35.75	148.324	0.22	1.000
	9.5	27.79	33.93	102.156	0.42	0.999	31.11	64.217	0.67	0.929	35.89	153.055	0.28	1.000
	10.5	29.76	34.07	104.896	0.51	0.992	31.25	65.527	0.82	0.767	36.01	157.281	0.34	1.000
	11.5	31.81	34.18	107.127	0.67	0.930	31.36	66.588	1.07	0.404	36.13	161.673	0.44	0.998
Memphis	2.5	13.78	20.09	23.568	0.71	0.895	8.43	12.232	1.36	0.133	26.17	36.513	0.46	0.998
	3.5	15.62	22.35	27.163	0.68	0.921	10.62	13.942	1.32	0.159	27.73	42.462	0.43	0.999
	4.5	16.95	23.66	29.775	0.66	0.931	11.99	15.076	1.31	0.165	28.64	46.863	0.42	0.999
	5.5	19.87	24.5	31.733	0.73	0.869	12.9	15.859	1.47	0.083	29.24	50.252	0.46	0.997
	6.5	21.47	25.08	33.244	0.77	0.826	13.49	16.382	1.57	0.053	29.67	52.963	0.48	0.996
	7.5	23.12	25.49	34.403	0.83	0.746	13.87	16.725	1.71	0.026	29.98	55.083	0.52	0.991
	8.5	24.83	25.8	35.334	0.92	0.616	14.08	16.917	1.93	0.009	30.23	56.904	0.57	0.978
	9.5	27.79	26.02	36.025	1.19	0.269	14.18	17.009	2.51	0.000	30.43	58.437	0.73	0.871
	10.5	29.76	26.18	36.546	1.46	0.084	14.17	17.000	3.15	0.000	30.58	59.634	0.90	0.652
	11.5	31.81	26.3	36.946	1.93	0.009	14.1	16.935	4.21	0.000	30.69	60.539	1.18	0.278

Table A-2 Continued

			T_R = 1033 Full PB (Idriss & Boulanger)				T_R = 475 Full PB (Idriss & Boulanger)				T_R = 2475 Full PB (Idriss & Boulanger)			
	Depth (m)	$N_{1,60,cs}$ site	N_{req}	$\%CSR^{site}$	FS_L	P_L	N_{req}	$\%CSR^{site}$	FS_L	P_L	N_{req}	$\%CSR^{site}$	FS_L	P_L
Portland	2.5	13.78	21.9	26.367	0.63	0.952	15.62	18.383	0.91	0.640	25.97	35.866	0.46	0.997
	3.5	15.62	24.02	30.584	0.60	0.967	18.2	21.153	0.87	0.694	27.61	41.939	0.44	0.999
	4.5	16.95	25.27	33.771	0.58	0.974	19.78	23.142	0.85	0.717	28.59	46.600	0.42	0.999
	5.5	19.87	26.09	36.251	0.64	0.945	20.82	24.628	0.94	0.581	29.25	50.312	0.46	0.997
	6.5	21.47	26.68	38.271	0.67	0.926	21.56	25.795	0.99	0.508	29.74	53.429	0.48	0.996
	7.5	23.12	27.13	39.965	0.72	0.886	22.09	26.698	1.07	0.400	30.11	56.017	0.51	0.992
	8.5	24.83	27.48	41.387	0.79	0.806	22.48	27.402	1.19	0.266	30.43	58.437	0.56	0.983
	9.5	27.79	27.76	42.595	1.00	0.495	22.77	27.949	1.53	0.063	30.69	60.539	0.71	0.896
	10.5	29.76	27.99	43.638	1.23	0.230	22.99	28.379	1.89	0.011	30.89	62.245	0.86	0.707
	11.5	31.81	28.18	44.537	1.60	0.045	23.15	28.701	2.48	0.001	31.08	63.942	1.11	0.348
Salt Lake City	2.5	13.78	21.06	24.996	0.67	0.929	13.29	16.203	1.03	0.461	26.28	36.878	0.45	0.998
	3.5	15.62	23.18	28.762	0.64	0.947	15.77	18.532	0.99	0.512	27.78	42.684	0.43	0.999
	4.5	16.95	24.38	31.438	0.63	0.953	17.29	20.120	0.98	0.527	28.65	46.916	0.42	0.999
	5.5	19.87	25.13	33.381	0.70	0.904	18.28	21.247	1.10	0.371	29.21	50.072	0.46	0.997
	6.5	21.47	25.65	34.877	0.74	0.866	18.94	22.050	1.16	0.293	29.6	52.504	0.49	0.995
	7.5	23.12	25.99	35.930	0.80	0.794	19.38	22.611	1.27	0.197	29.87	54.314	0.53	0.990
	8.5	24.83	26.24	36.745	0.89	0.668	19.66	22.981	1.42	0.104	30.07	55.727	0.58	0.974
	9.5	27.79	26.41	37.320	1.15	0.313	19.83	23.210	1.84	0.014	30.22	56.829	0.75	0.848
	10.5	29.76	26.52	37.702	1.42	0.103	19.9	23.305	2.30	0.001	30.33	57.662	0.93	0.606
	11.5	31.81	26.58	37.913	1.88	0.011	19.91	23.319	3.06	0.000	30.39	58.125	1.23	0.231
San Francisco	2.5	13.78	27.22	40.322	0.41	0.999	24.51	31.758	0.52	0.990	29.39	51.169	0.33	1.000
	3.5	15.62	28.66	46.969	0.39	1.000	26.25	36.778	0.50	0.994	30.6	59.797	0.31	1.000
	4.5	16.95	29.5	51.861	0.38	1.000	27.26	40.482	0.49	0.995	31.32	66.199	0.30	1.000
	5.5	19.87	30.04	55.511	0.42	0.999	27.91	43.270	0.54	0.987	31.81	71.239	0.33	1.000
	6.5	21.47	30.47	58.752	0.44	0.999	28.38	45.522	0.56	0.981	32.16	75.235	0.34	1.000
	7.5	23.12	30.76	61.127	0.47	0.997	28.71	47.237	0.61	0.965	32.46	78.955	0.36	1.000
	8.5	24.83	30.97	62.950	0.52	0.991	28.95	48.560	0.67	0.925	32.67	81.736	0.40	1.000
	9.5	27.79	31.16	64.680	0.66	0.933	29.15	49.716	0.86	0.708	32.82	83.819	0.51	0.993
	10.5	29.76	31.31	66.102	0.81	0.777	29.3	50.615	1.06	0.420	32.94	85.545	0.63	0.955
	11.5	31.81	31.43	67.278	1.06	0.418	29.41	51.294	1.39	0.118	33.04	87.027	0.82	0.765
San Jose	2.5	13.78	25.67	34.937	0.48	0.996	23	28.399	0.59	0.973	27.74	42.506	0.39	1.000
	3.5	15.62	27.25	40.442	0.45	0.998	24.89	32.734	0.56	0.981	29.08	49.306	0.37	1.000
	4.5	16.95	28.16	44.441	0.44	0.998	25.95	35.803	0.55	0.984	29.88	54.383	0.36	1.000
	5.5	19.87	28.75	47.453	0.49	0.995	26.64	38.127	0.61	0.963	30.44	58.516	0.40	1.000
	6.5	21.47	29.15	49.716	0.52	0.992	27.09	39.809	0.64	0.944	30.79	61.382	0.42	0.999
	7.5	23.12	29.46	51.607	0.55	0.983	27.41	41.095	0.70	0.904	31.04	63.578	0.45	0.998
	8.5	24.83	29.67	52.963	0.62	0.960	27.63	42.026	0.77	0.821	31.28	65.814	0.50	0.994
	9.5	27.79	29.82	53.971	0.79	0.800	27.78	42.684	1.00	0.498	31.45	67.478	0.63	0.950
	10.5	29.76	29.92	54.662	0.98	0.530	27.88	43.133	1.24	0.218	31.57	68.694	0.78	0.816
	11.5	31.81	29.99	55.154	1.29	0.178	27.93	43.362	1.64	0.037	31.65	69.526	1.03	0.465

Table A-2 Continued

			$T_R = 1033$ Full PB (Idriss & Boulanger)				$T_R = 475$ Full PB (Idriss & Boulanger)				$T_R = 2475$ Full PB (Idriss & Boulanger)			
	Depth (m)	$N_{1,60,cs}$ site	N_{req}	$\%CSR^{site}$	FS_L	P_L	N_{req}	$\%CSR^{site}$	FS_L	P_L	N_{req}	$\%CSR^{site}$	FS_L	P_L
Santa Monica	2.5	13.78	24.77	32.419	0.51	0.992	21.24	25.278	0.66	0.934	27.6	41.896	0.40	1.000
	3.5	15.62	26.46	37.492	0.49	0.995	23.34	29.092	0.63	0.951	28.94	48.504	0.38	1.000
	4.5	16.95	27.43	41.178	0.48	0.996	24.53	31.808	0.62	0.957	29.75	53.497	0.37	1.000
	5.5	19.87	28.02	43.778	0.53	0.989	25.28	33.799	0.69	0.911	30.28	57.281	0.41	0.999
	6.5	21.47	28.47	45.978	0.56	0.982	25.78	35.272	0.73	0.875	30.65	60.207	0.43	0.999
	7.5	23.12	28.76	47.507	0.60	0.966	26.13	36.382	0.79	0.806	30.89	62.245	0.46	0.997
	8.5	24.83	28.97	48.674	0.67	0.927	26.38	37.217	0.88	0.685	31.08	63.942	0.51	0.993
	9.5	27.79	29.13	49.598	0.86	0.705	26.55	37.807	1.13	0.329	31.24	65.432	0.65	0.938
	10.5	29.76	29.24	50.252	1.06	0.410	26.65	38.163	1.40	0.111	31.35	66.490	0.81	0.783
	11.5	31.81	29.32	50.737	1.40	0.110	26.71	38.379	1.86	0.013	31.43	67.278	1.06	0.418
Seattle	2.5	13.78	24.06	30.676	0.54	0.986	19.42	22.663	0.73	0.867	27.4	41.053	0.41	0.999
	3.5	15.62	25.87	35.551	0.52	0.991	21.72	26.061	0.71	0.896	28.82	47.835	0.38	1.000
	4.5	16.95	26.92	39.157	0.50	0.993	23.04	28.479	0.69	0.907	29.67	52.963	0.37	1.000
	5.5	19.87	27.61	41.939	0.55	0.983	23.88	30.264	0.77	0.829	30.24	56.979	0.41	0.999
	6.5	21.47	28.09	44.107	0.58	0.975	24.45	31.609	0.81	0.775	30.66	60.290	0.43	0.999
	7.5	23.12	28.45	45.876	0.62	0.956	24.84	32.602	0.88	0.680	30.96	62.861	0.46	0.998
	8.5	24.83	28.72	47.291	0.69	0.911	25.11	33.326	0.98	0.533	31.22	65.243	0.50	0.994
	9.5	27.79	28.92	48.391	0.88	0.673	25.3	33.856	1.26	0.200	31.43	67.278	0.64	0.949
	10.5	29.76	29.09	49.364	1.08	0.385	25.43	34.228	1.56	0.053	31.6	69.004	0.78	0.820
	11.5	31.81	29.22	50.132	1.42	0.102	25.5	34.432	2.07	0.004	31.73	70.374	1.01	0.482

APPENDIX B: SAMPLE LIQUEFACTION LOADING MAPS

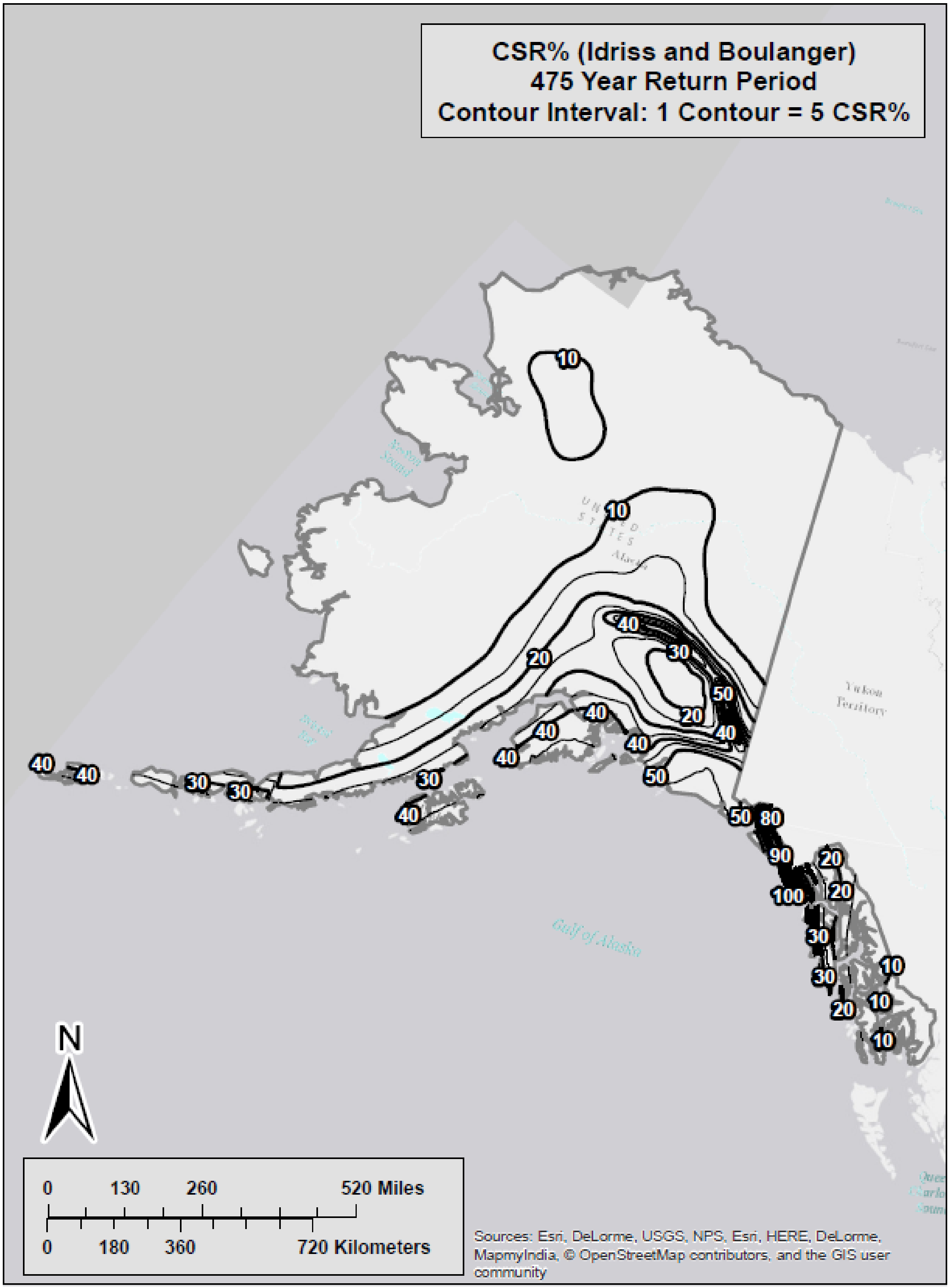

Sources: Esri, DeLorme, USGS, NPS, Esri, HERE, DeLorme, MapmyIndia, © OpenStreetMap contributors, and the GIS user community

Figure B-1 Liquefaction Triggering ($CSR\%^{ref}$) Map for Alaska (T_r = 475)

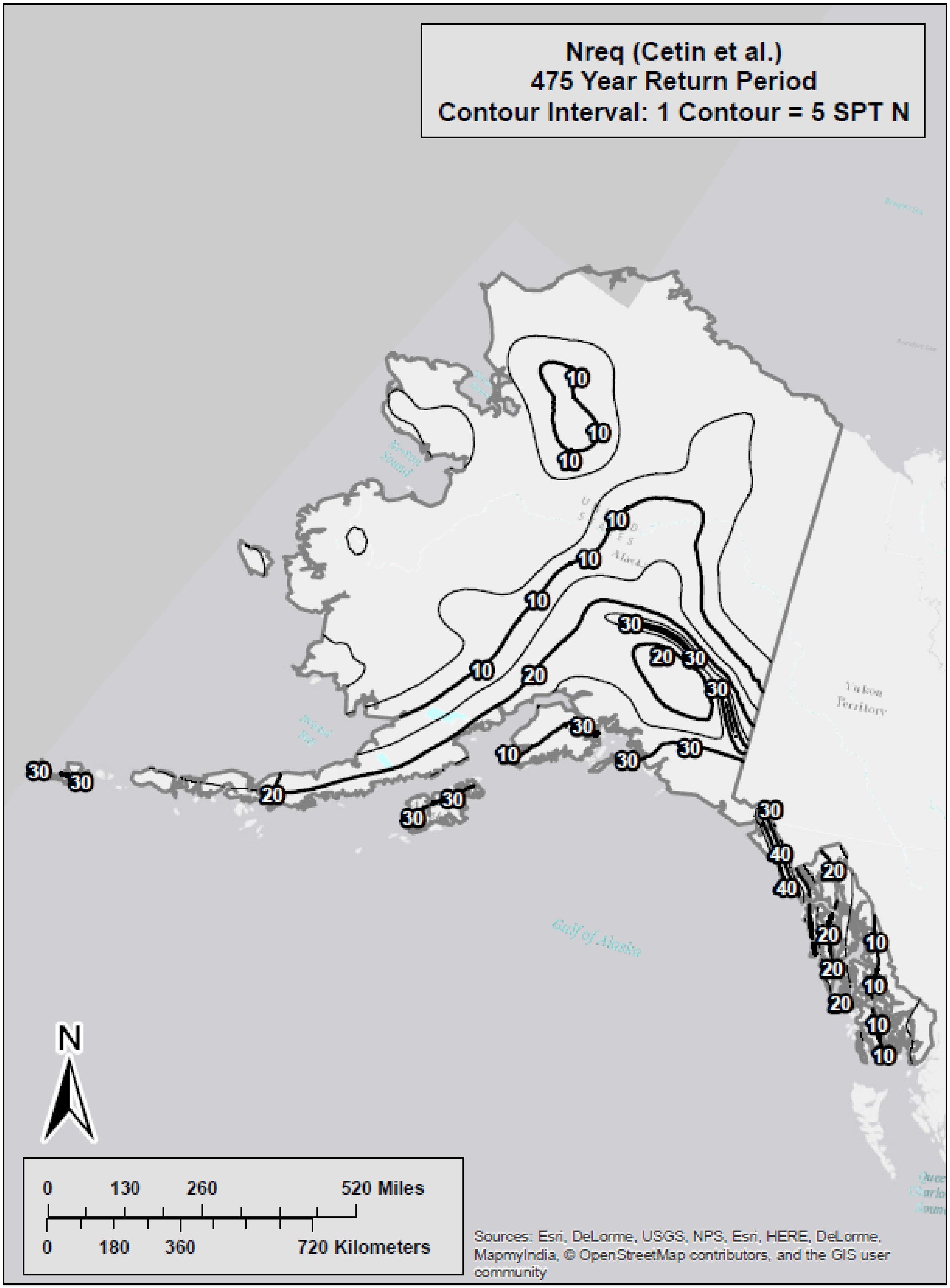

Figure B-2 Liquefaction Triggering (N_{req}^{ref}) Map for Alaska (T_r = 475)

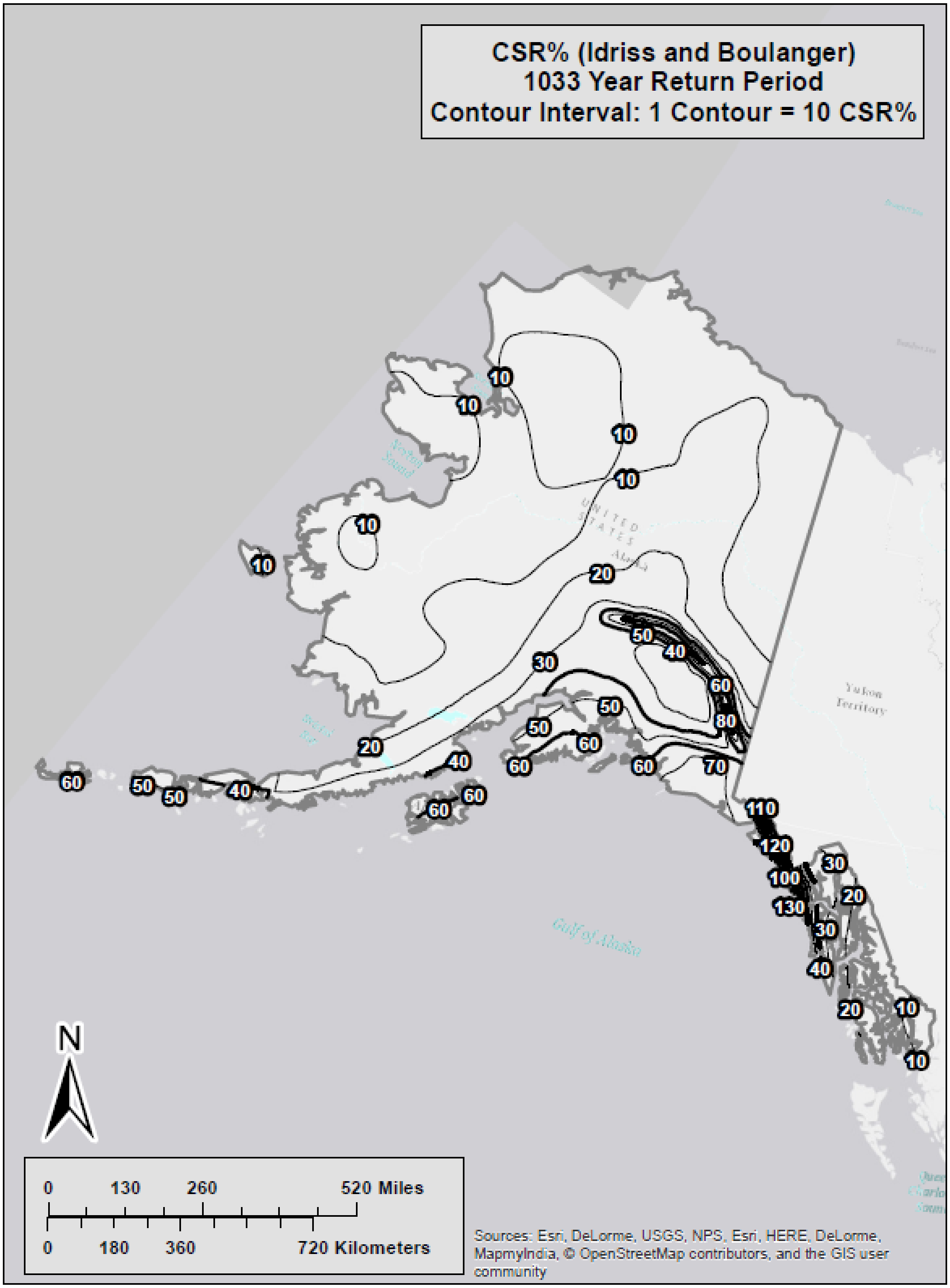

CSR% (Idriss and Boulanger)
1033 Year Return Period
Contour Interval: 1 Contour = 10 CSR%

Sources: Esri, DeLorme, USGS, NPS, Esri, HERE, DeLorme, MapmyIndia, © OpenStreetMap contributors, and the GIS user community

Figure B-3 Liquefaction Triggering ($CSR\%^{ref}$) Map for Alaska (T_r = 1,033)

Sources: Esri, DeLorme, USGS, NPS, Esri, HERE, DeLorme, MapmyIndia, © OpenStreetMap contributors, and the GIS user community

Figure B-4 Liquefaction Triggering (N_{req}^{ref}) Map for Alaska (T_r = 1,033)

Figure B-5 Liquefaction Triggering ($CSR\%^{ref}$) Map for Alaska ($T_r = 2{,}475$)

Figure B-6 Liquefaction Triggering (N_{req}^{ref}) Map for Alaska (T_r = 2,475)

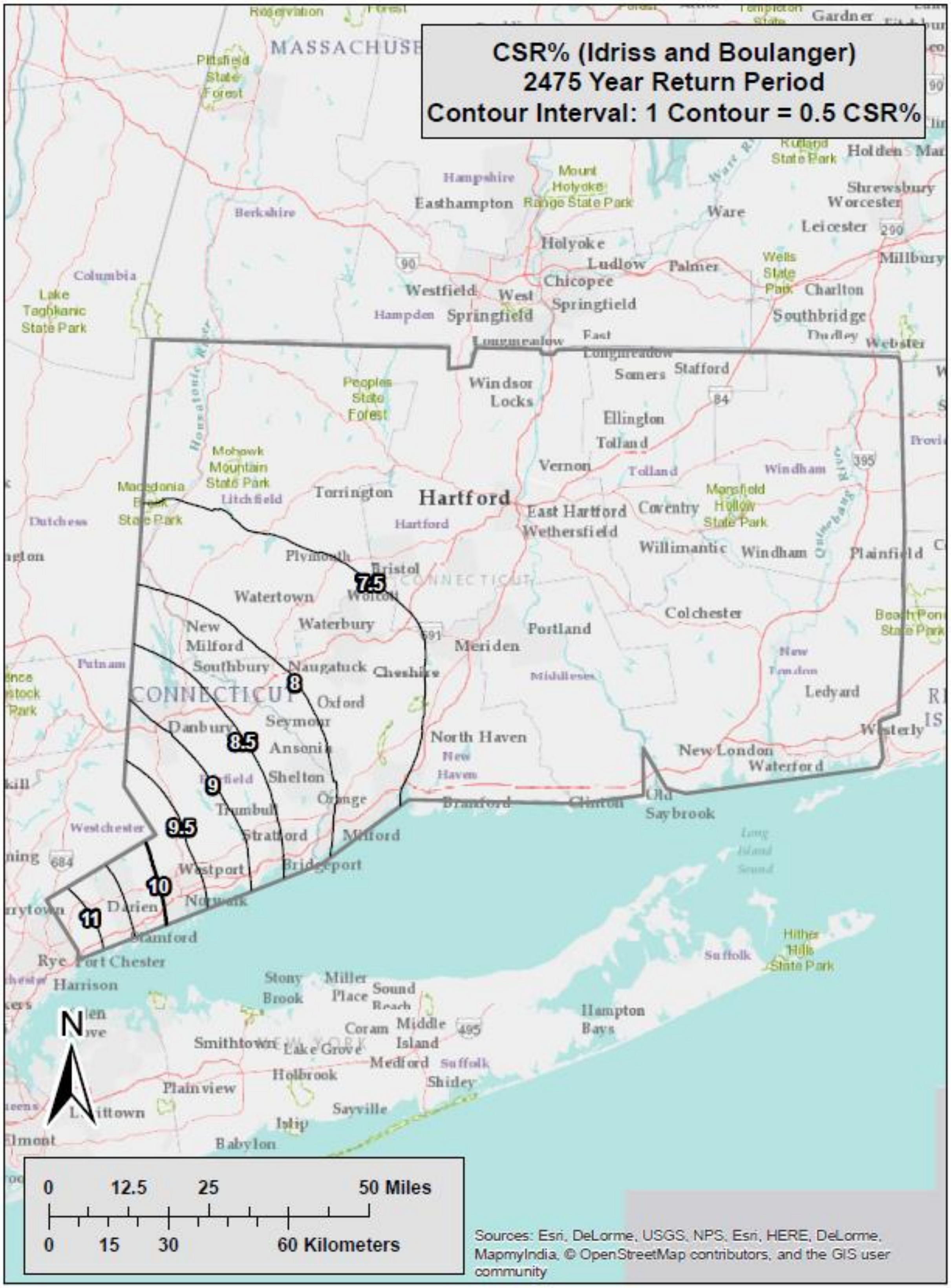

Figure B-7 Liquefaction Triggering ($CSR\%^{ref}$) Map for Connecticut ($T_r = 2,475$)

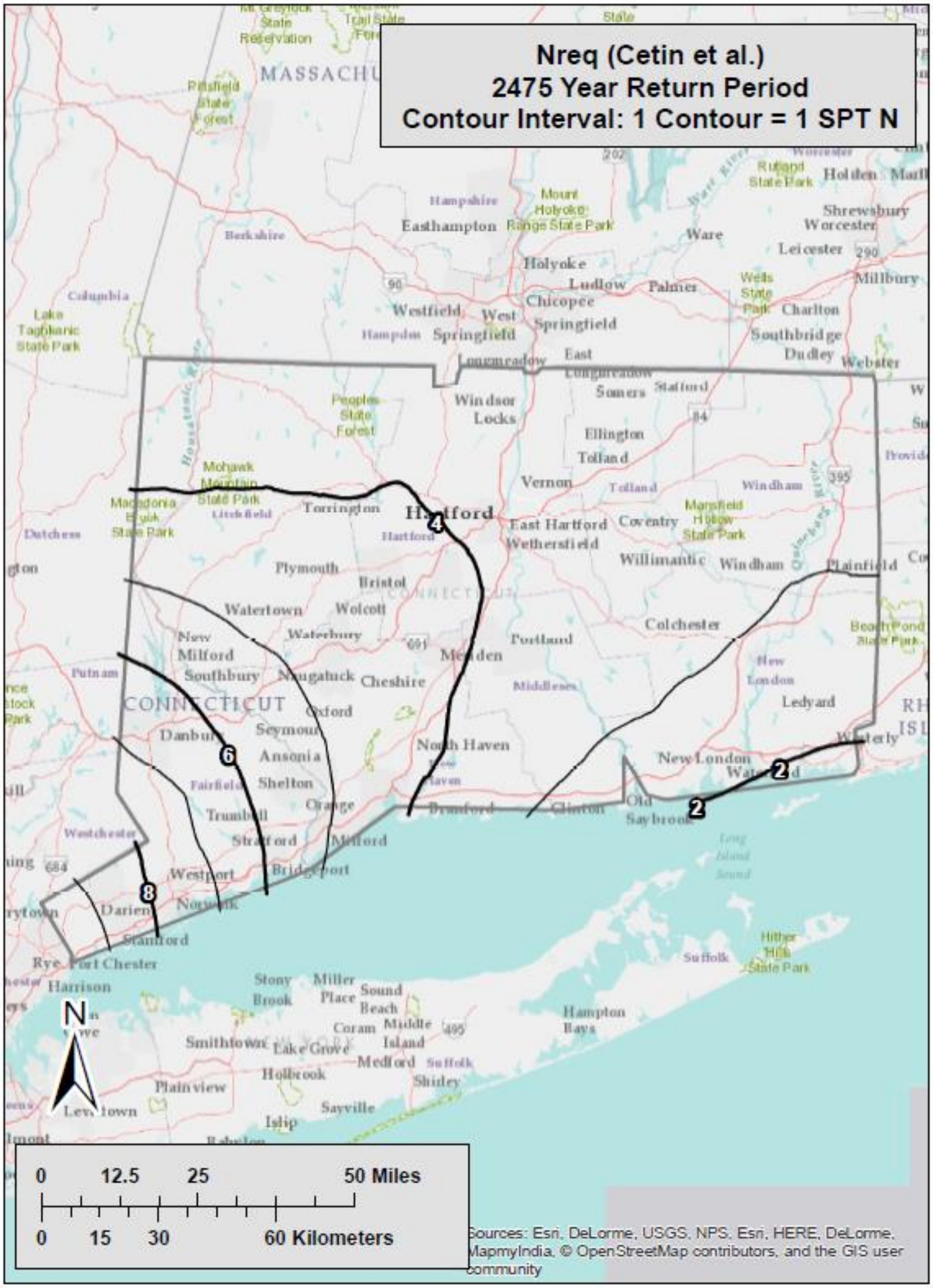

Sources: Esri, DeLorme, USGS, NPS, Esri, HERE, DeLorme, MapmyIndia, © OpenStreetMap contributors, and the GIS user community

Figure B-8 Liquefaction Triggering (N_{req}^{ref}) Map for Connecticut (T_r = 2,475)

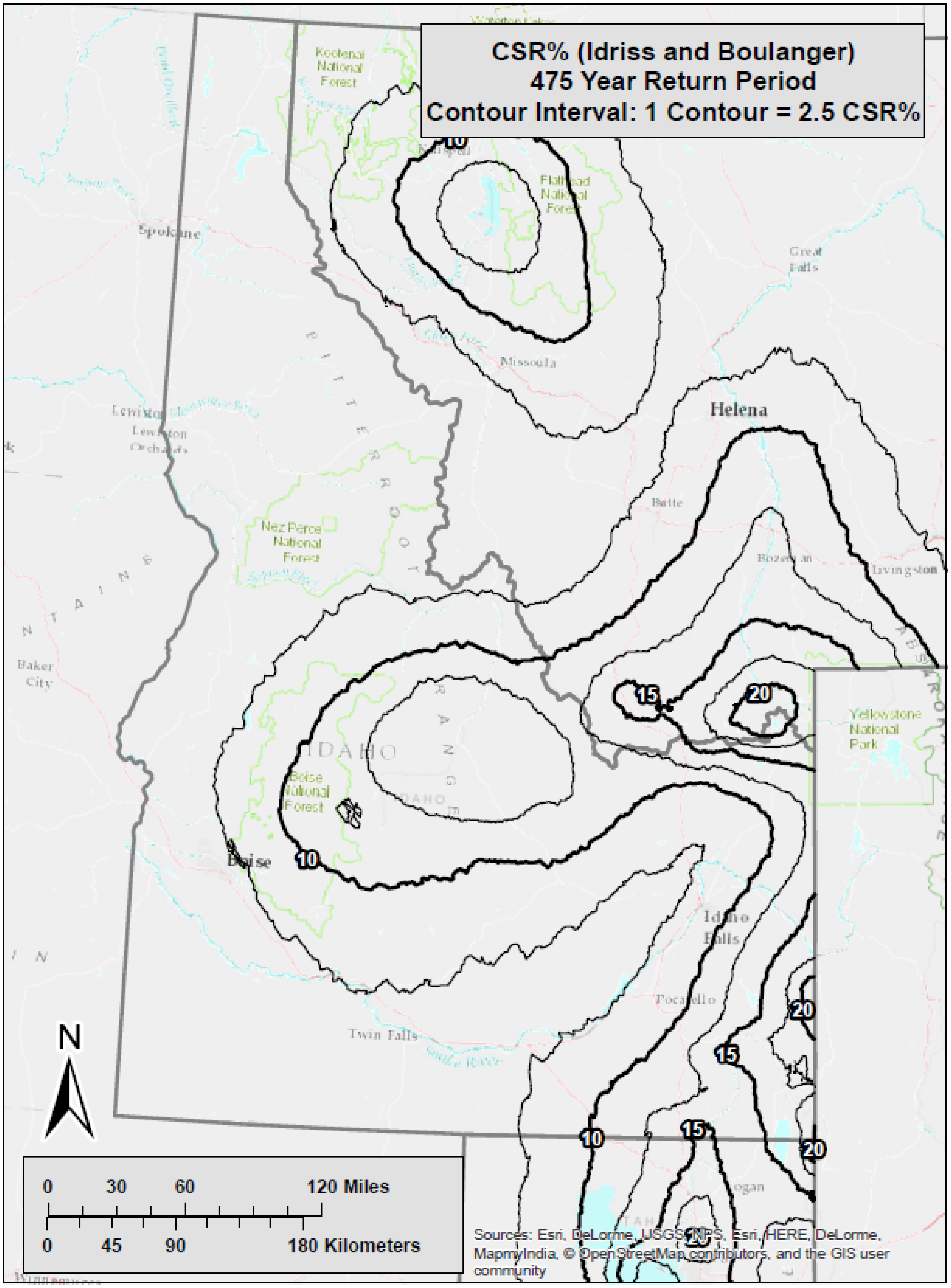

Figure B-9 Liquefaction Triggering ($CSR\%^{ref}$) Map for Idaho (T_r = 475)

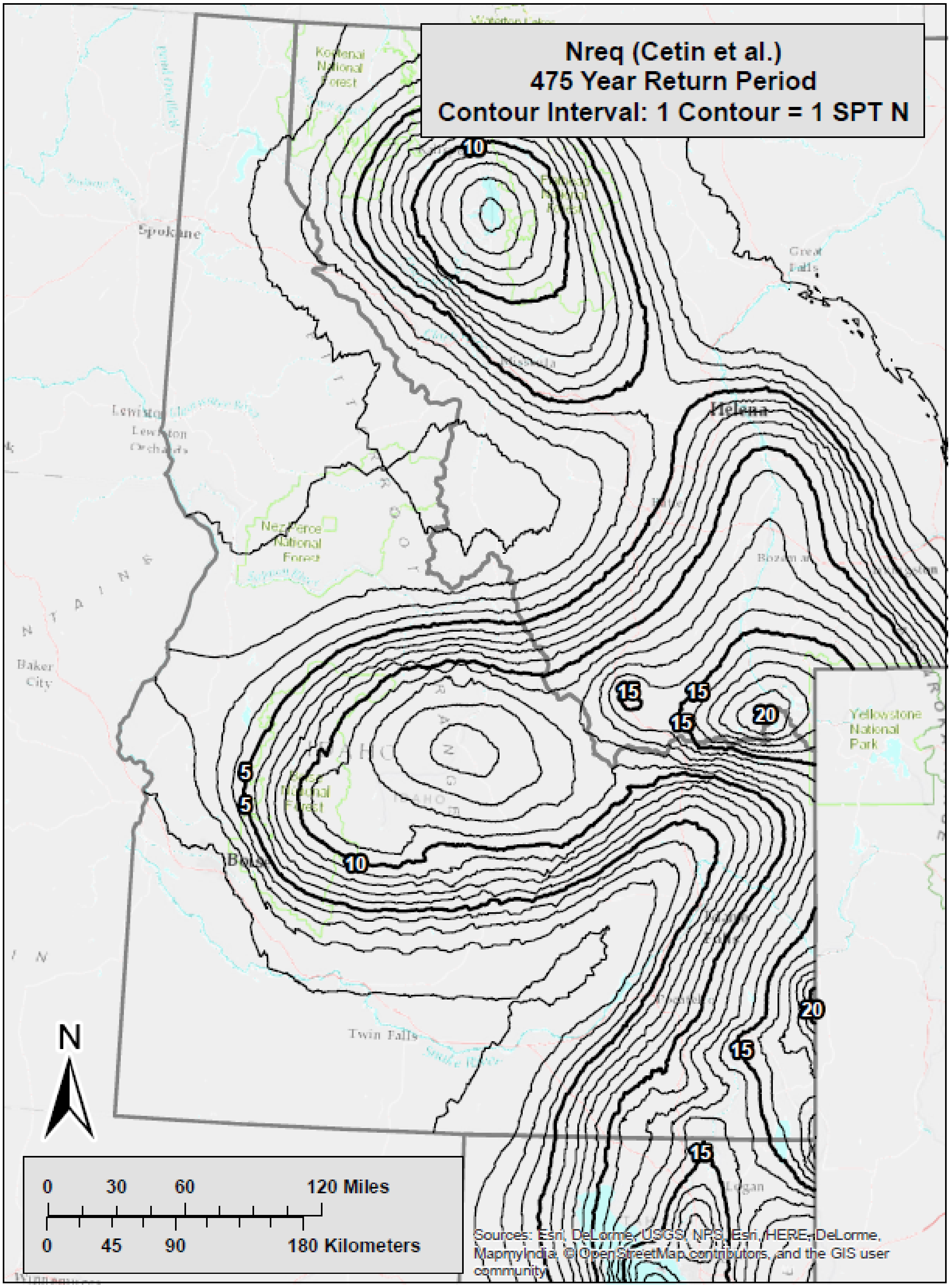

Figure B-10 Liquefaction Triggering (N_{req}^{ref}) Map for Idaho (T_r = 475)

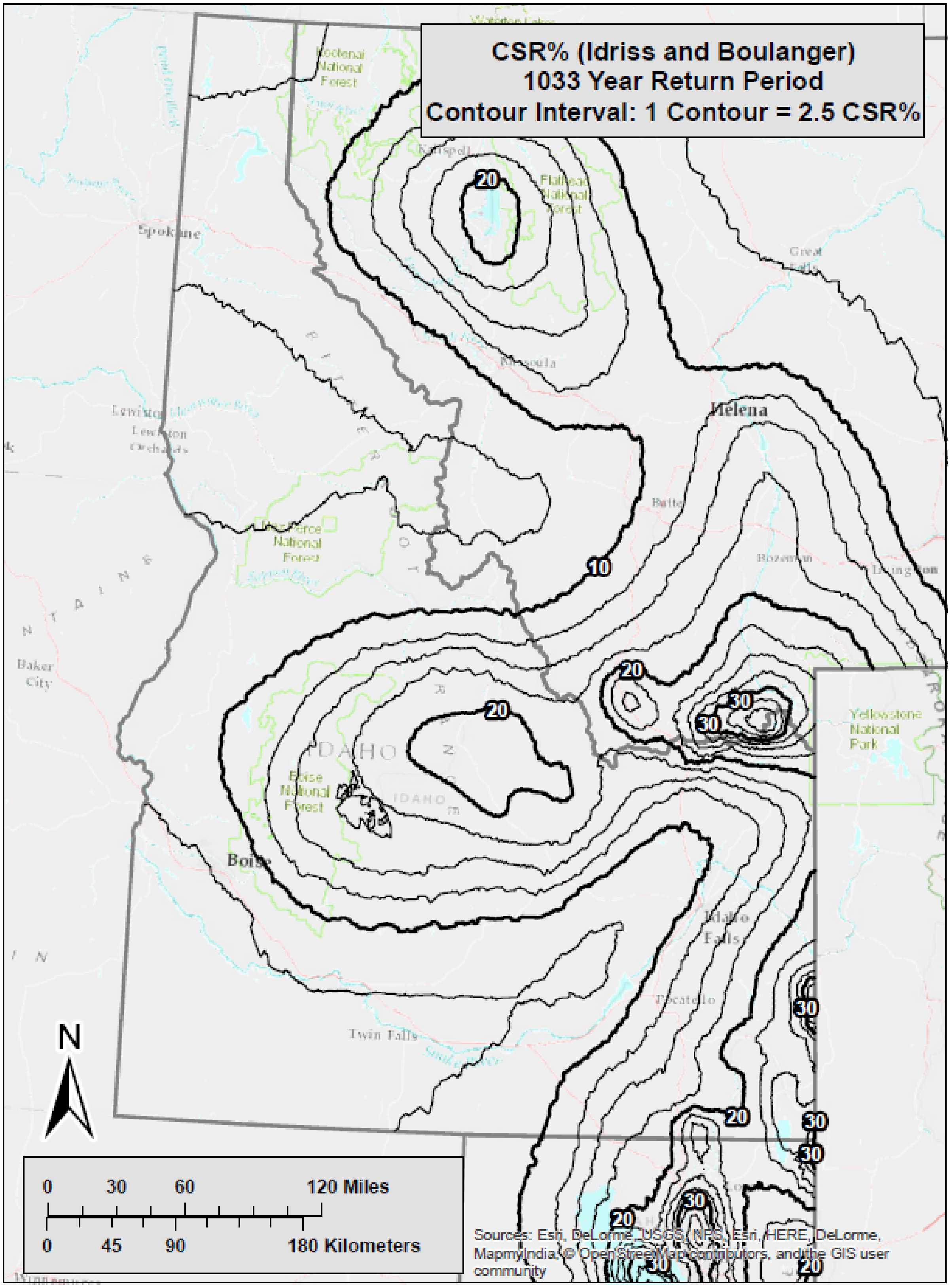

Sources: Esri, DeLorme, USGS, NPS, Esri, HERE, DeLorme, MapmyIndia, © OpenStreetMap contributors, and the GIS user community

Figure B-11 Liquefaction Triggering ($CSR\%^{ref}$) Map for Idaho ($T_r = 1{,}033$)

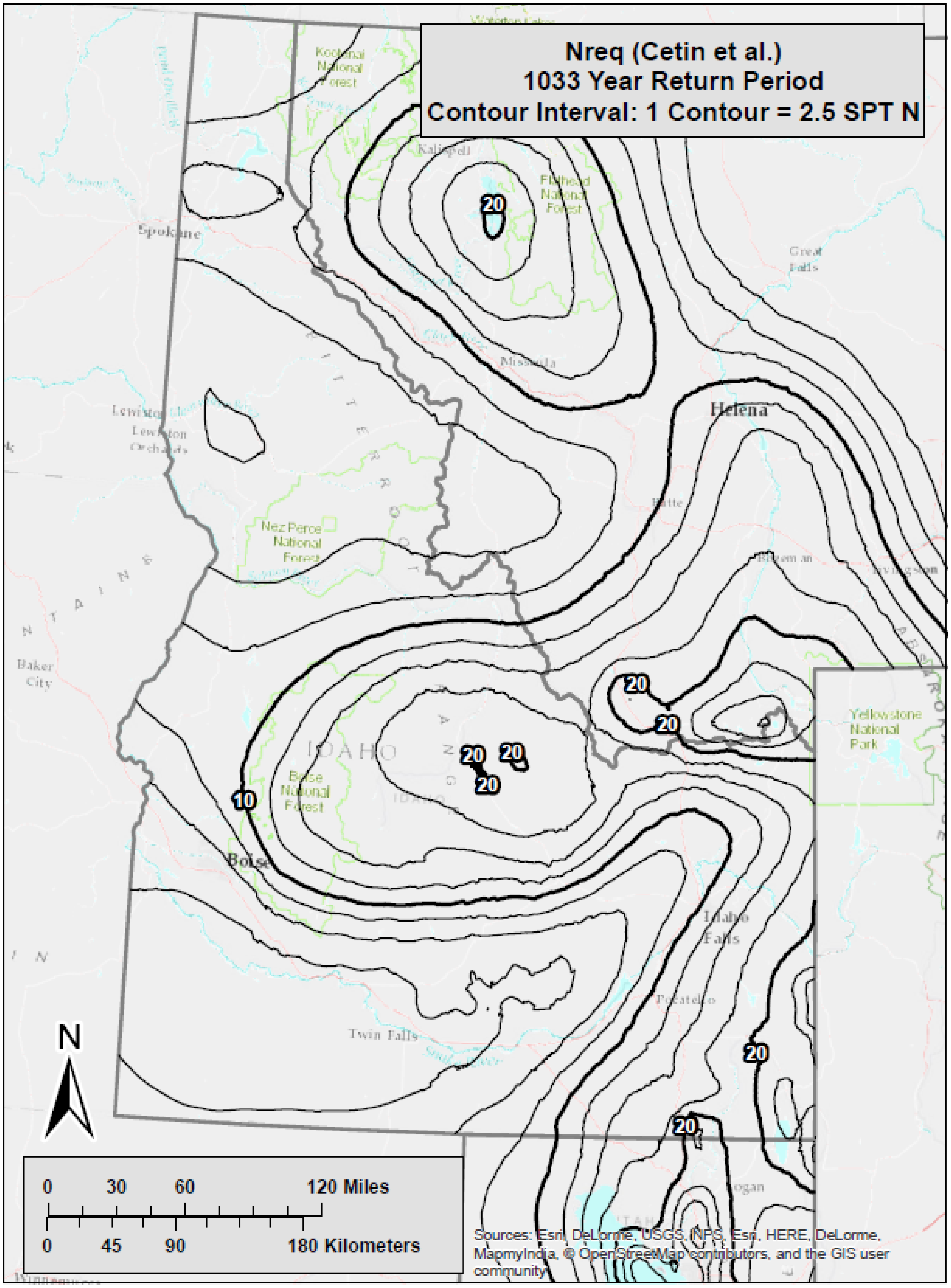

Nreq (Cetin et al.)
1033 Year Return Period
Contour Interval: 1 Contour = 2.5 SPT N

Sources: Esri, DeLorme, USGS, NPS, Esri, HERE, DeLorme, MapmyIndia, © OpenStreetMap contributors, and the GIS user community

Figure B-12 Liquefaction Triggering (N_{req}^{ref}) Map for Idaho (T_r = 1,033)

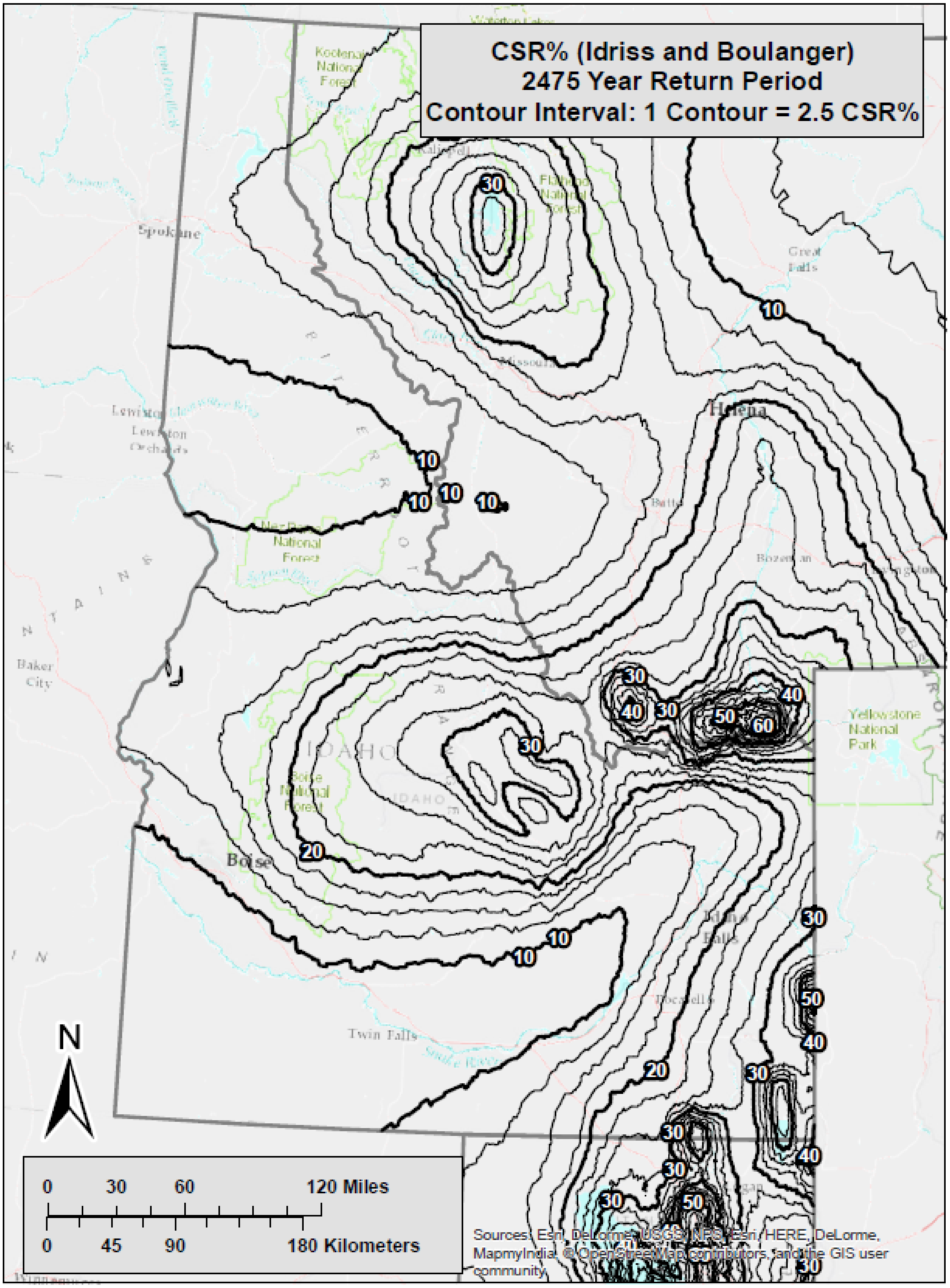

Sources: Esri, DeLorme, USGS, NPS, Esri, HERE, DeLorme, MapmyIndia, © OpenStreetMap contributors, and the GIS user community

Figure B-13 Liquefaction Triggering ($CSR\%^{ref}$) Map for Idaho (T_r = 2,475)

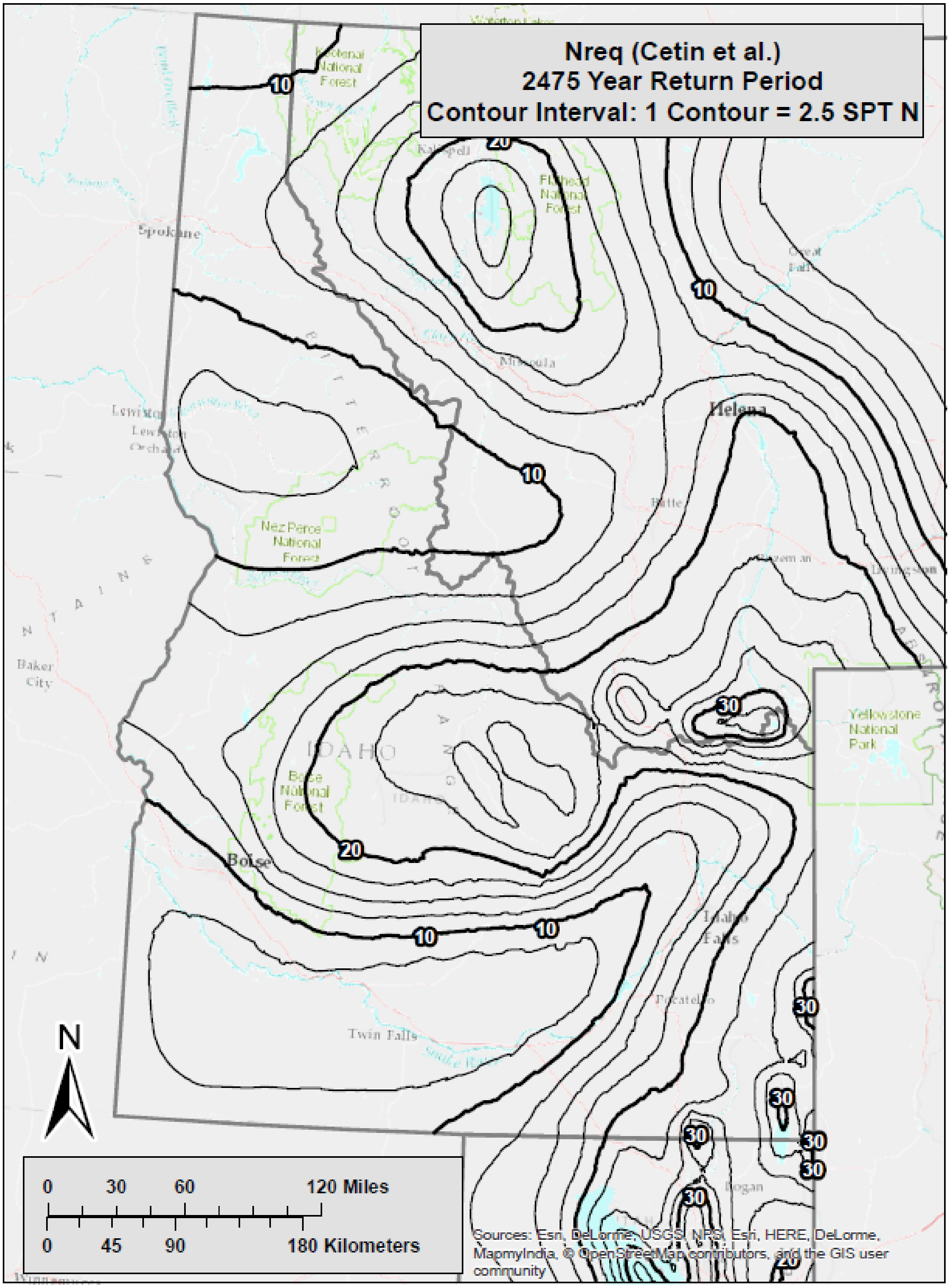

Sources: Esri, DeLorme, USGS, NPS, Esri, HERE, DeLorme, MapmyIndia, © OpenStreetMap contributors, and the GIS user community

Figure B-14 Liquefaction Triggering (N_{req}^{ref}) Map for Idaho (T_r = 2,475)

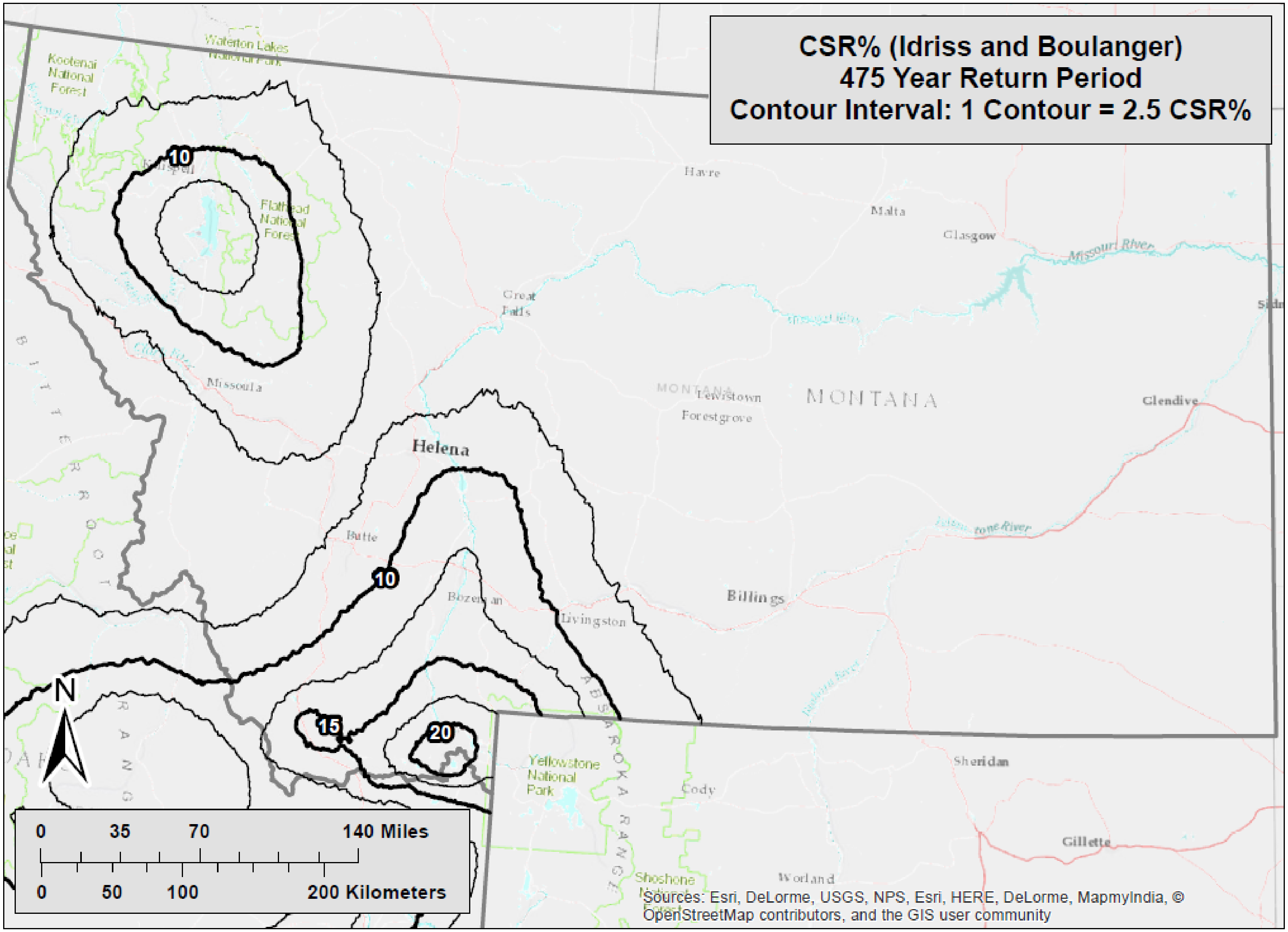

Sources: Esri, DeLorme, USGS, NPS, Esri, HERE, DeLorme, MapmyIndia, © OpenStreetMap contributors, and the GIS user community

Figure B-15 Liquefaction Triggering ($CSR\%^{ref}$) Map for Montana ($T_r = 475$)

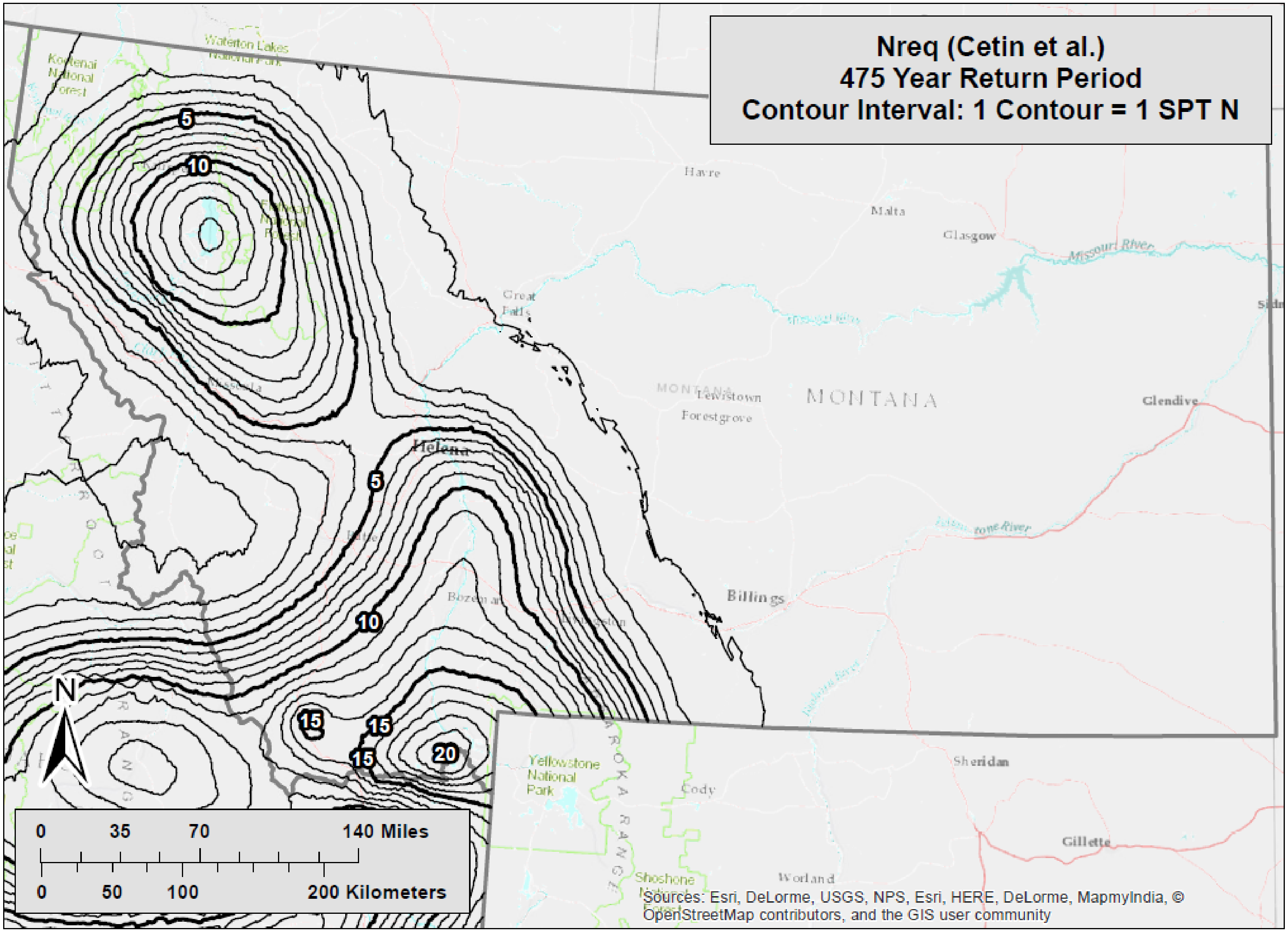

Sources: Esri, DeLorme, USGS, NPS, Esri, HERE, DeLorme, MapmyIndia, © OpenStreetMap contributors, and the GIS user community

Figure B-16 Liquefaction Triggering (N_{req}^{ref}) Map for Montana (T_r = 475)

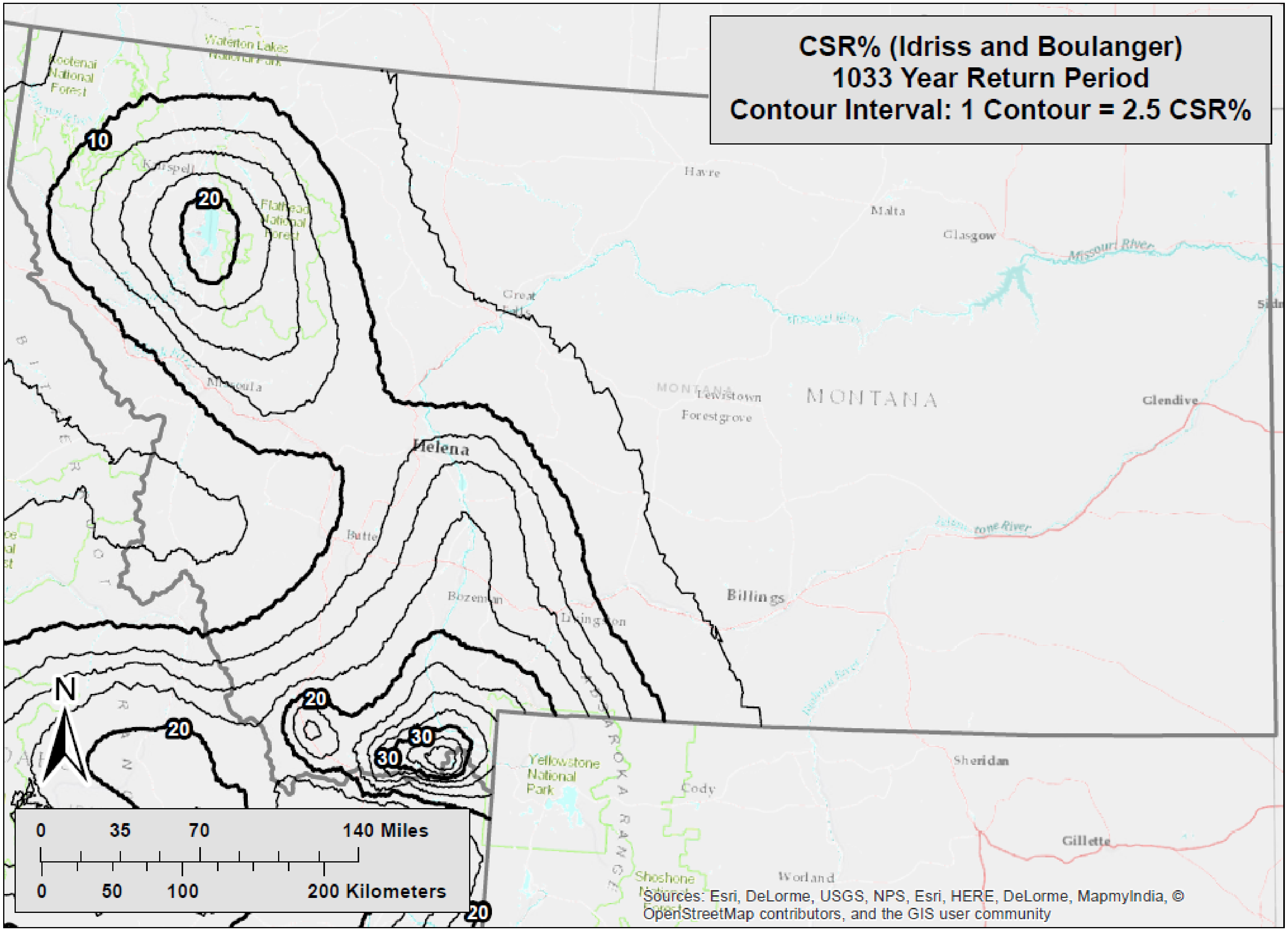

Figure B-17 Liquefaction Triggering ($CSR\%^{ref}$) Map for Montana (T_r = 1,033)

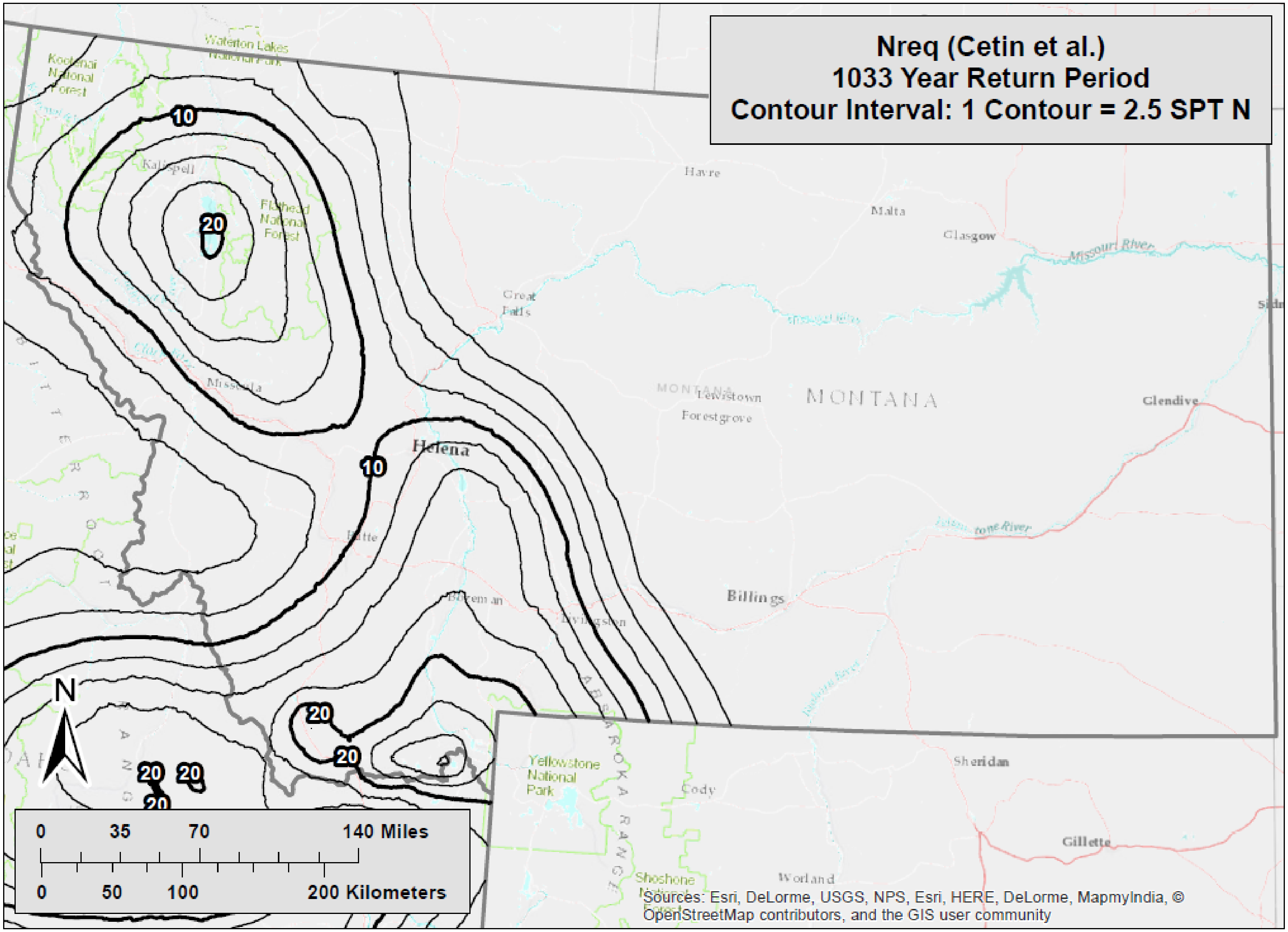

Sources: Esri, DeLorme, USGS, NPS, Esri, HERE, DeLorme, MapmyIndia, © OpenStreetMap contributors, and the GIS user community

Figure B-18 Liquefaction Triggering (N_{req}^{ref}) Map for Montana ($T_r = 1,033$)

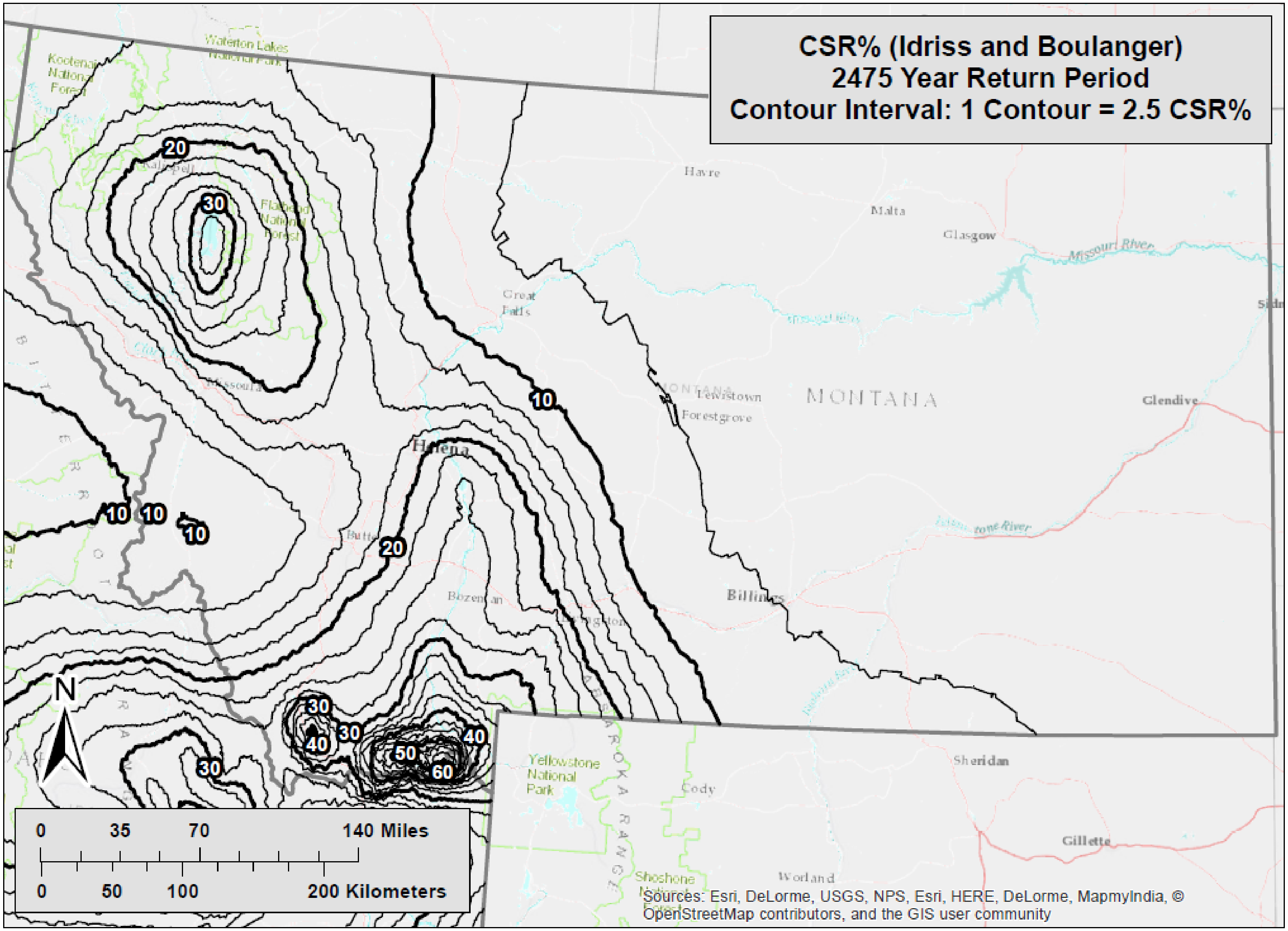

Figure B-19 Liquefaction Triggering ($CSR\%^{ref}$) Map for Montana ($T_r = 2{,}475$)

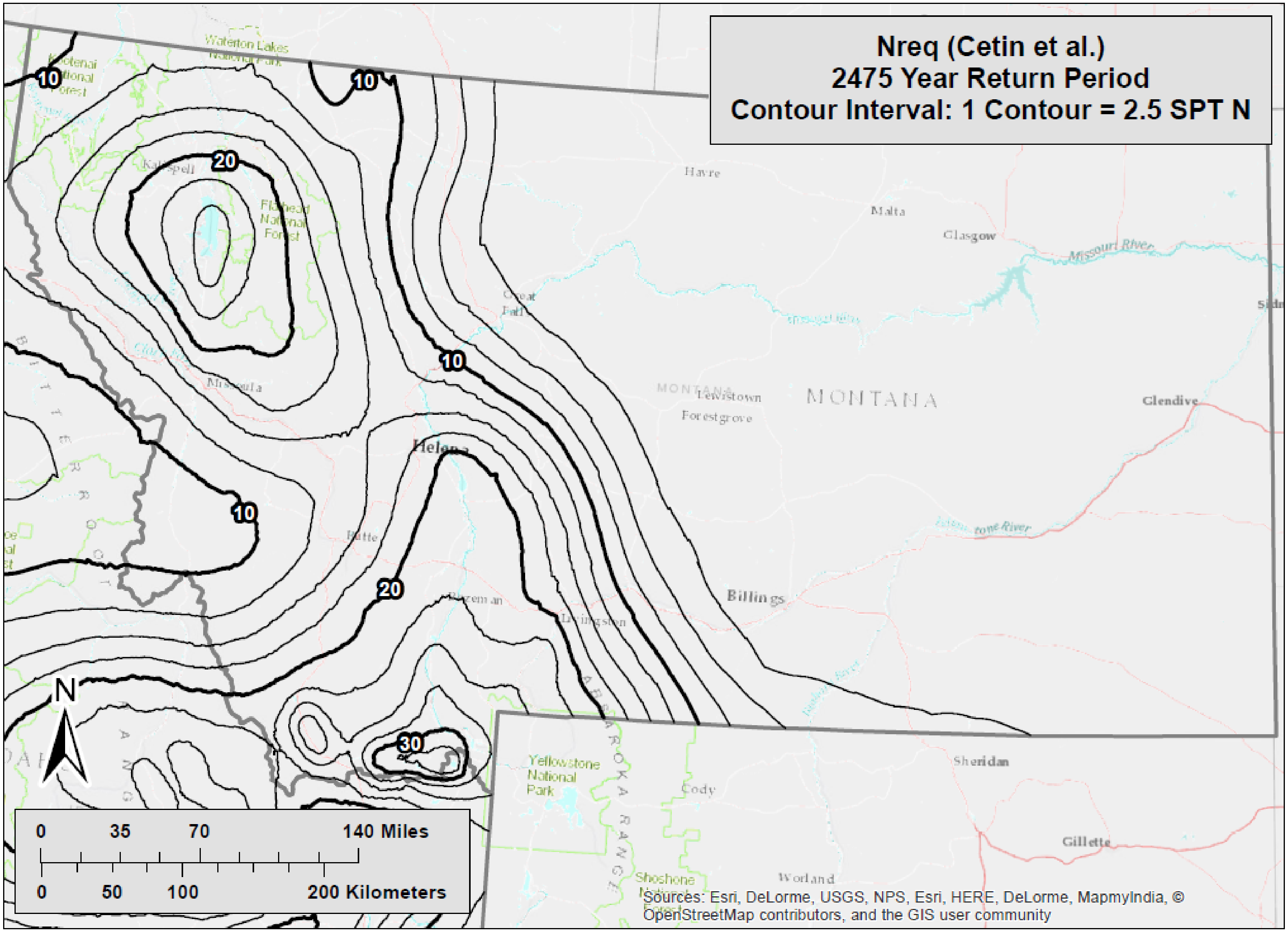

Figure B-20 Liquefaction Triggering (N_{req}^{ref}) Map for Montana ($T_r = 2,475$)

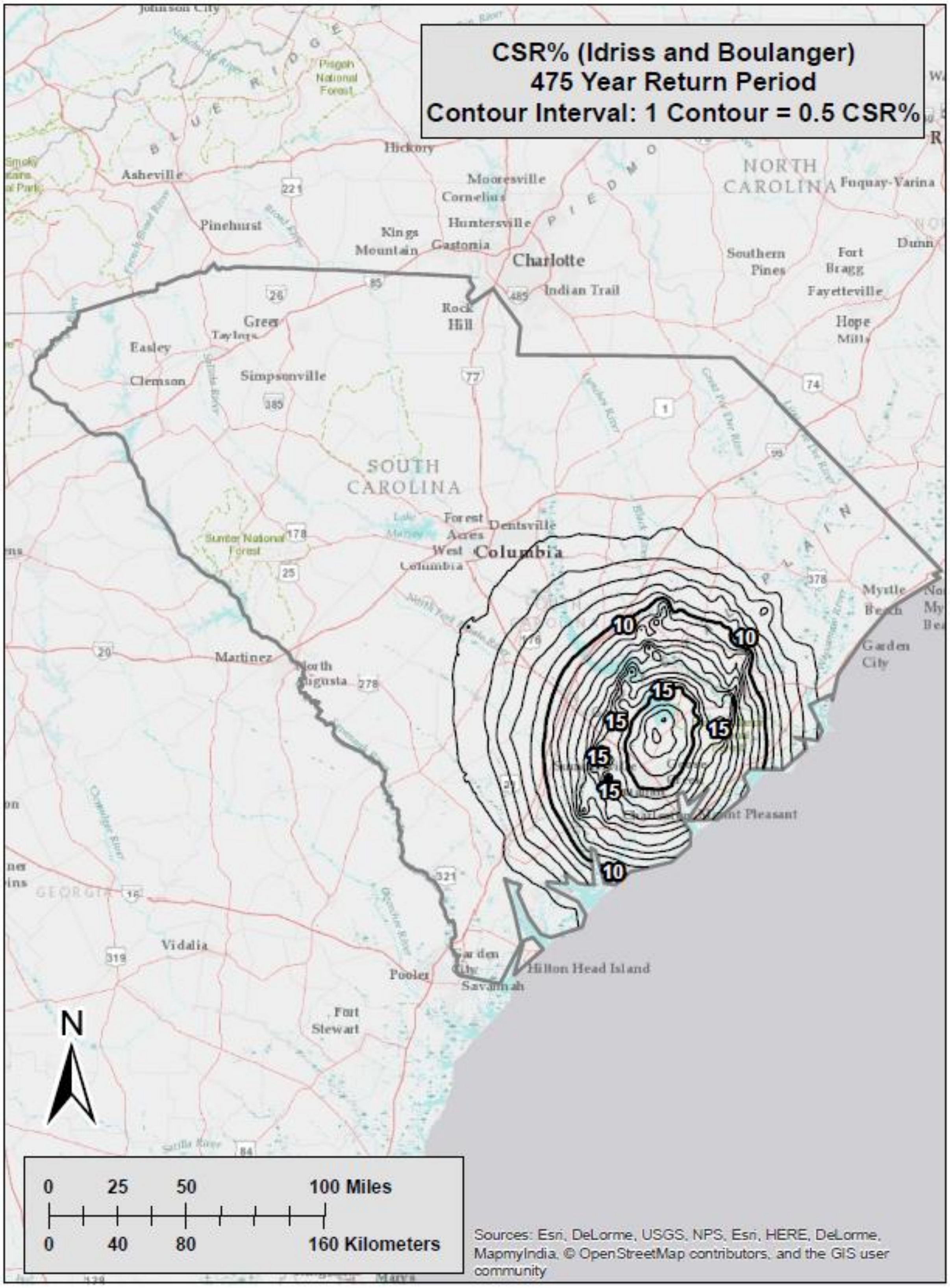

Figure B-21 Liquefaction Triggering ($CSR\%^{ref}$) Map for South Carolina ($T_r = 475$)

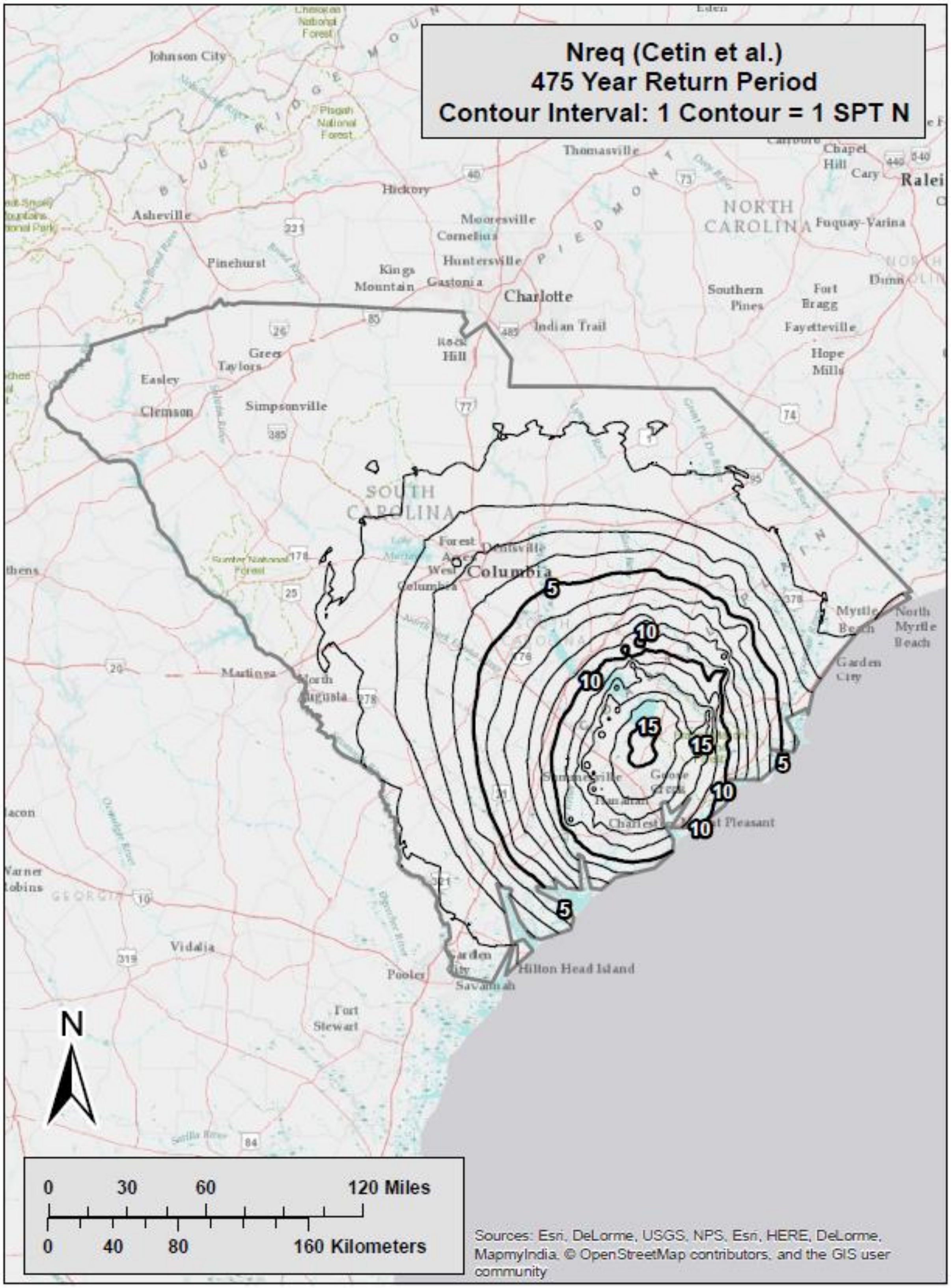

Figure B-22 Liquefaction Triggering ($N_{req}^{ref,\ Cetin}$) Map for South Carolina (T_r = 475)

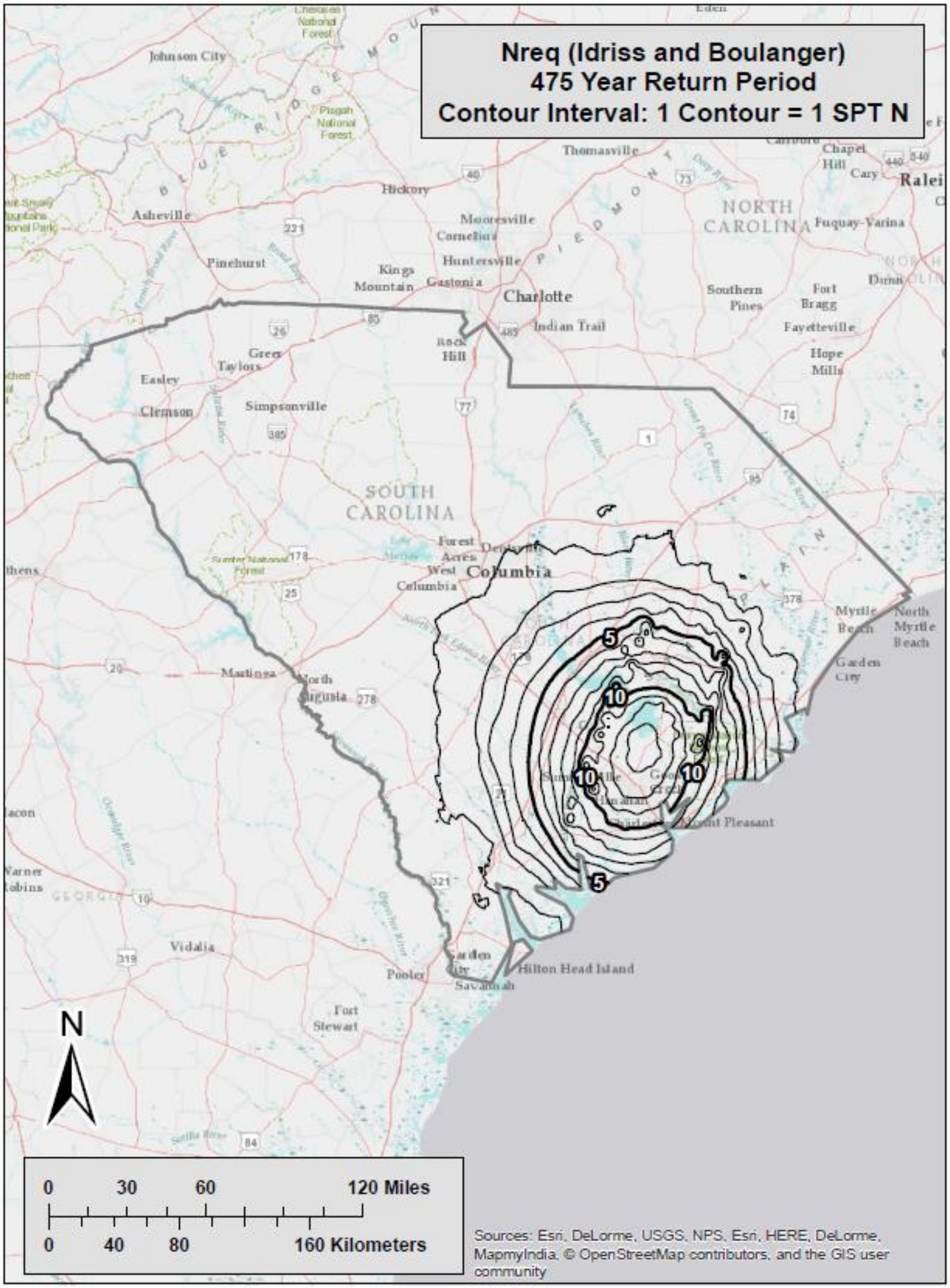

Sources: Esri, DeLorme, USGS, NPS, Esri, HERE, DeLorme, MapmyIndia, © OpenStreetMap contributors, and the GIS user community

Figure B-23 Liquefaction Triggering ($N_{req}^{ref, Idriss}$) Map for South Carolina (T_r = 475)

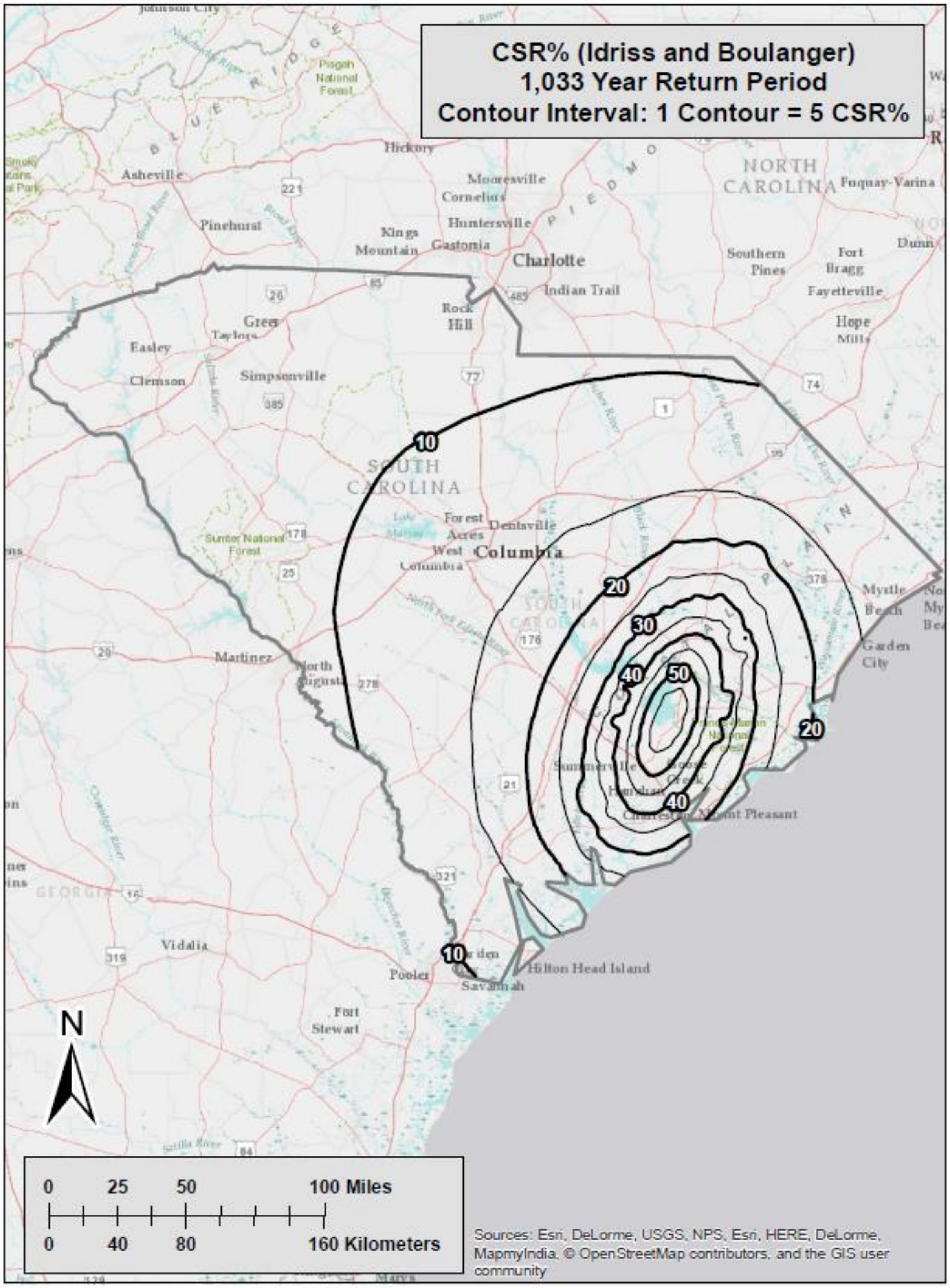

Figure B-24 Liquefaction Triggering (*CSR%^{ref}*) Map for South Carolina (T_r = 1,033)

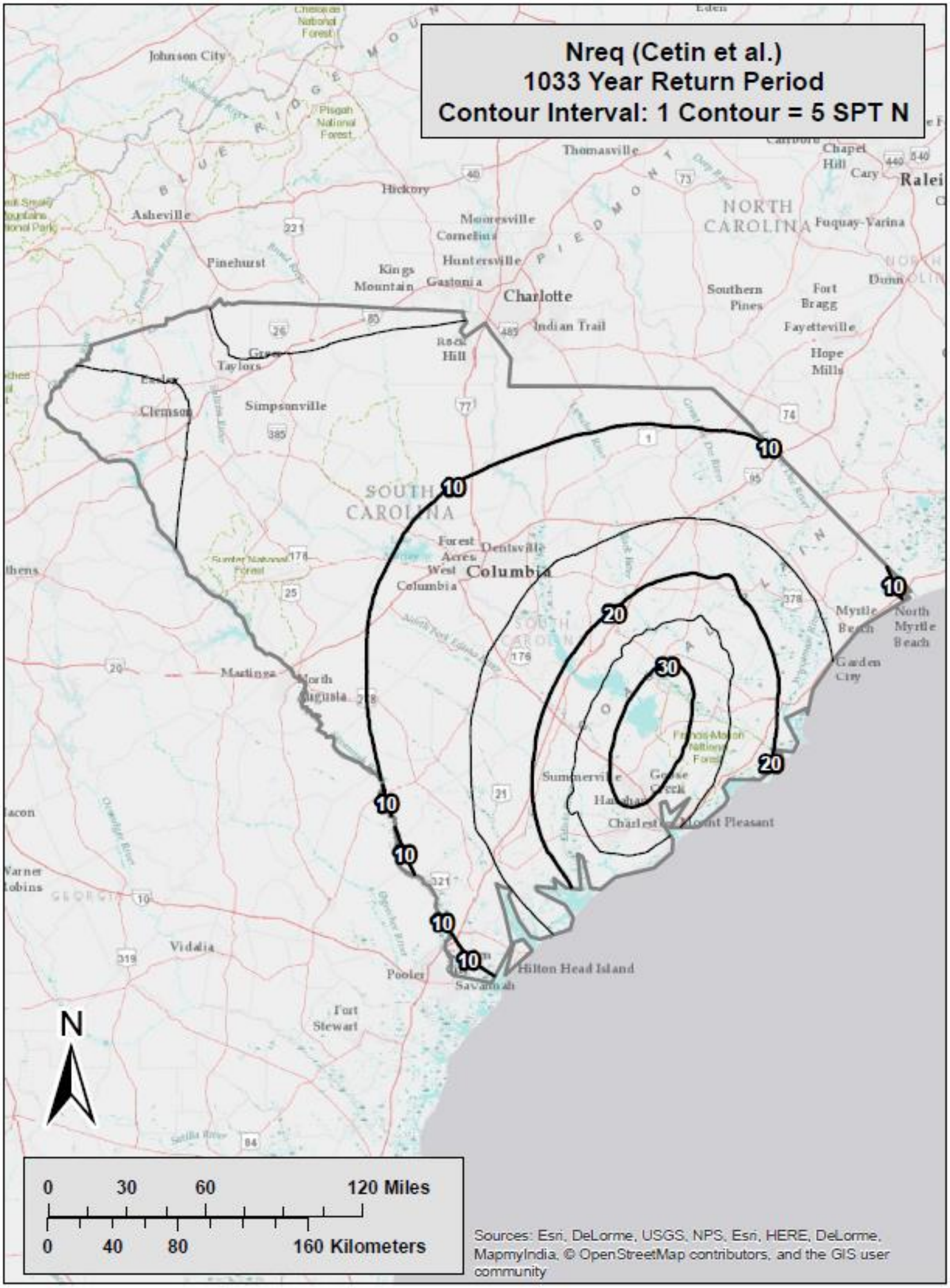

Figure B-25 Liquefaction Triggering ($N_{req}^{ref,Cetin}$) Map for South Carolina (T_r = 1,033)

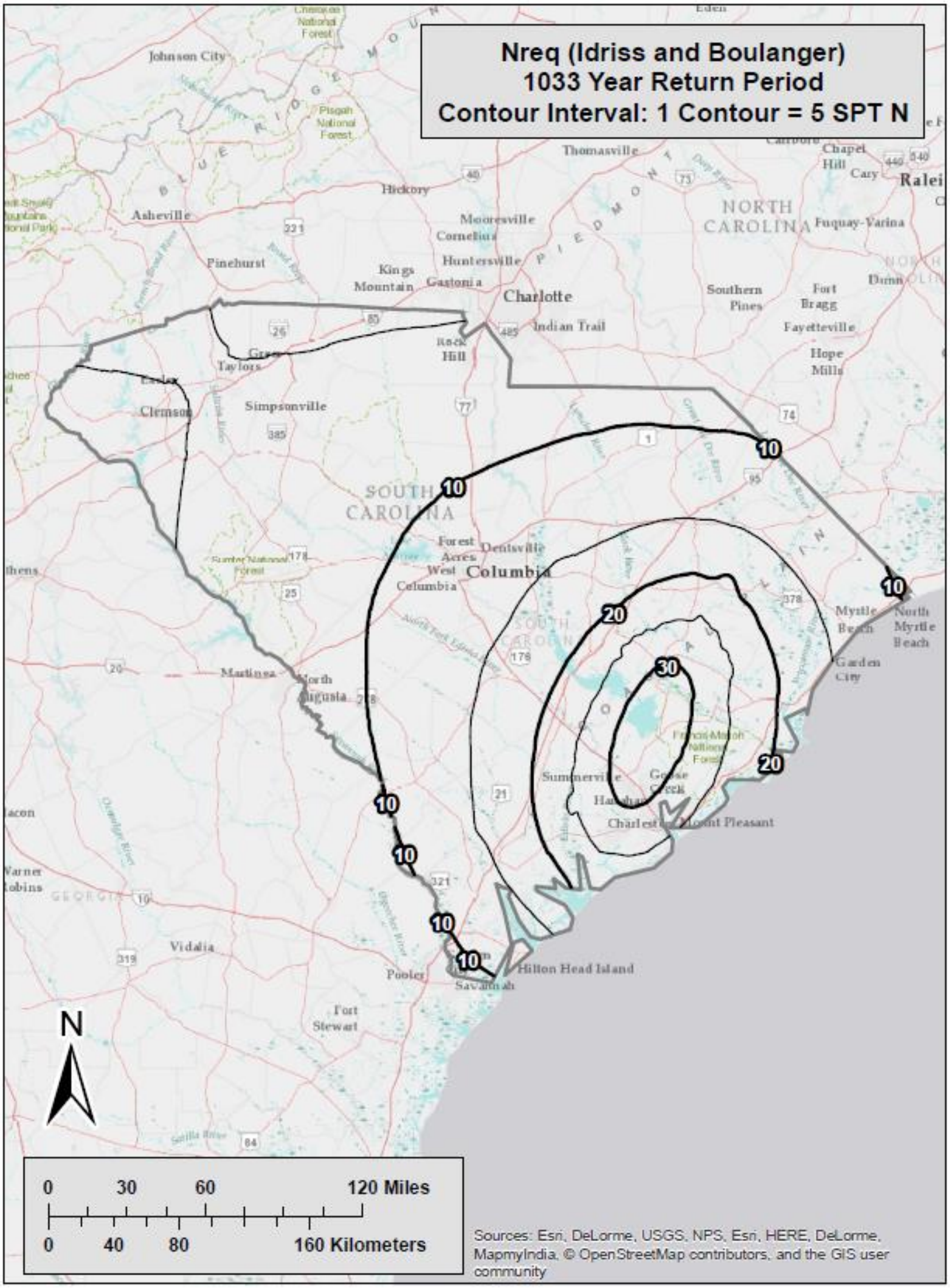

Figure B-26 Liquefaction Triggering ($N_{req}^{ref,Idriss}$) Map for South Carolina (T_r = 1,033)

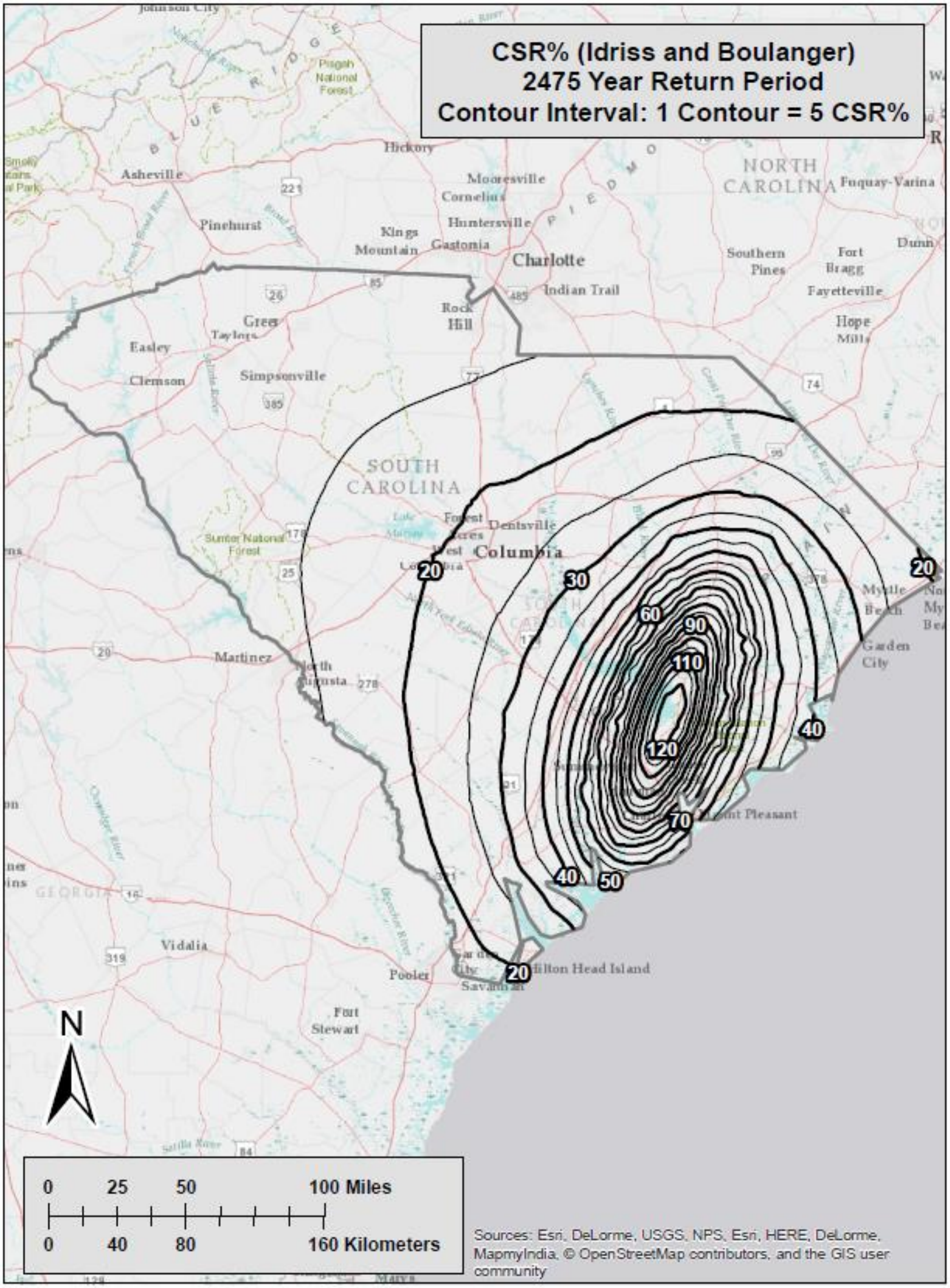

Figure B-27 Liquefaction Triggering ($CSR\%^{ref}$) Map for South Carolina (T_r = 2,475)

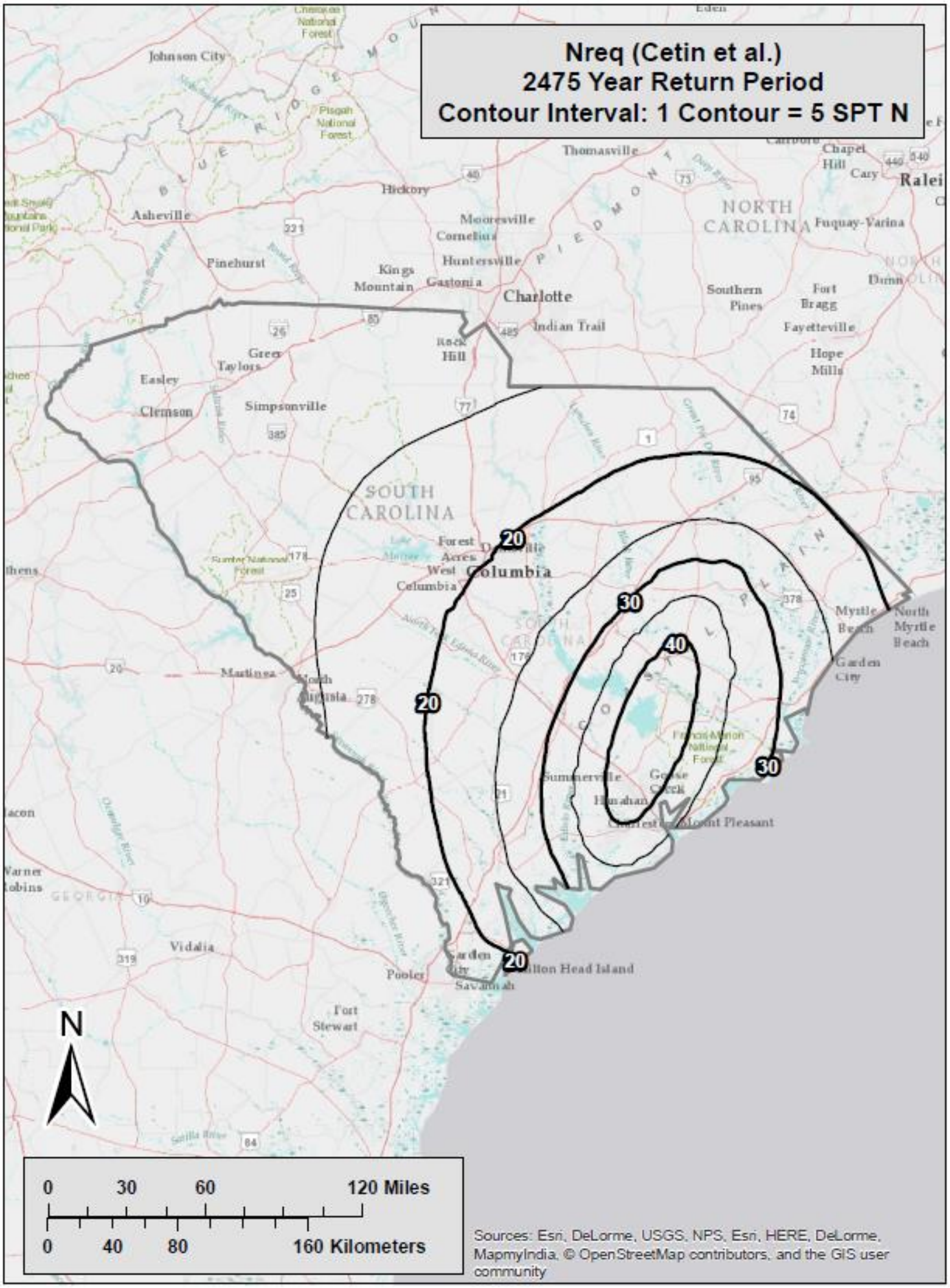

Figure B-28 Liquefaction Triggering ($N_{req}^{ref,Cetin}$) Map for South Carolina (T_r = 2,475)

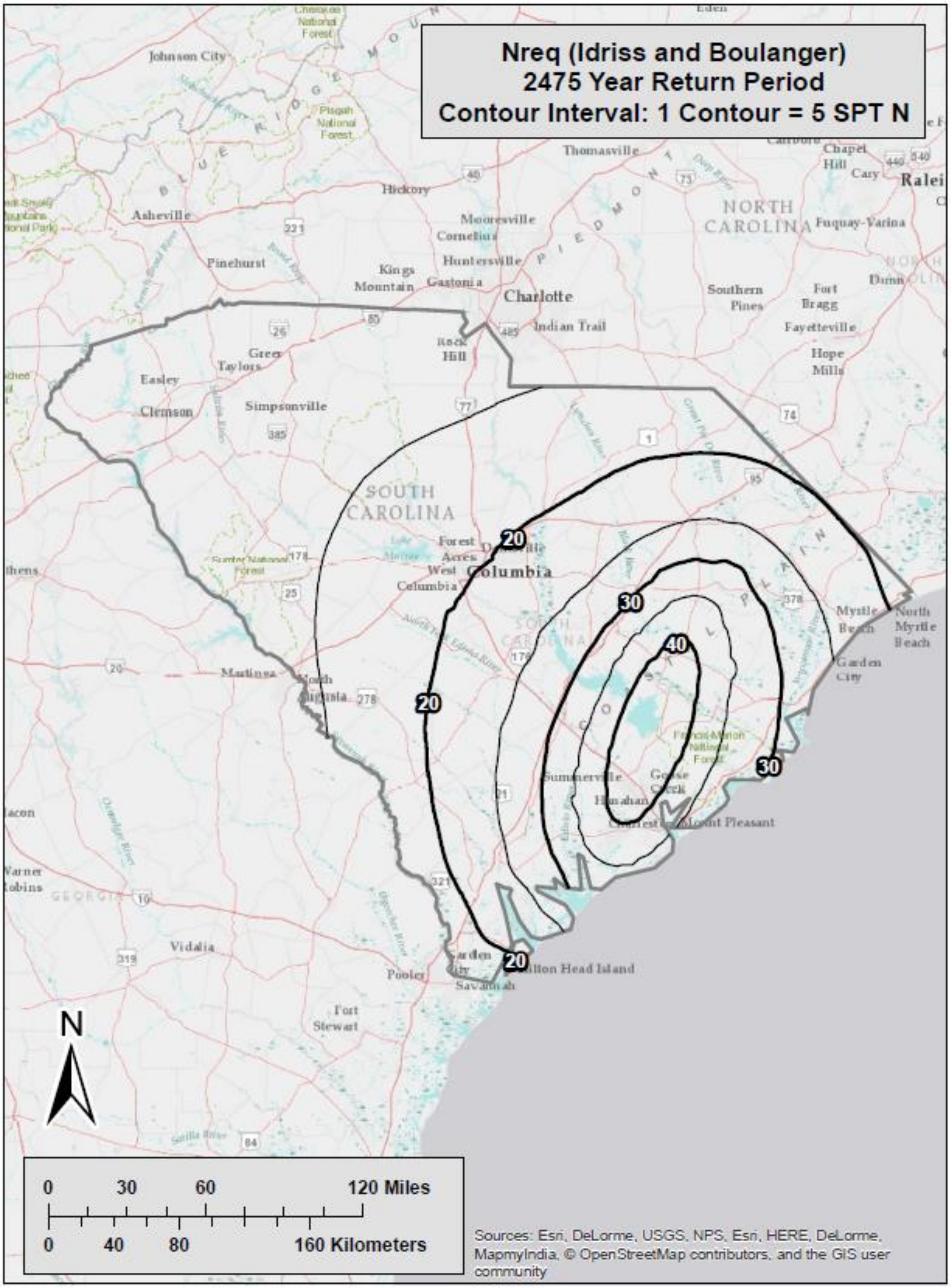

Sources: Esri, DeLorme, USGS, NPS, Esri, HERE, DeLorme, MapmyIndia, © OpenStreetMap contributors, and the GIS user community

Figure B-29 Liquefaction Triggering ($N_{req}^{ref,Idriss}$) Map for South Carolina (T_r = 2,475)

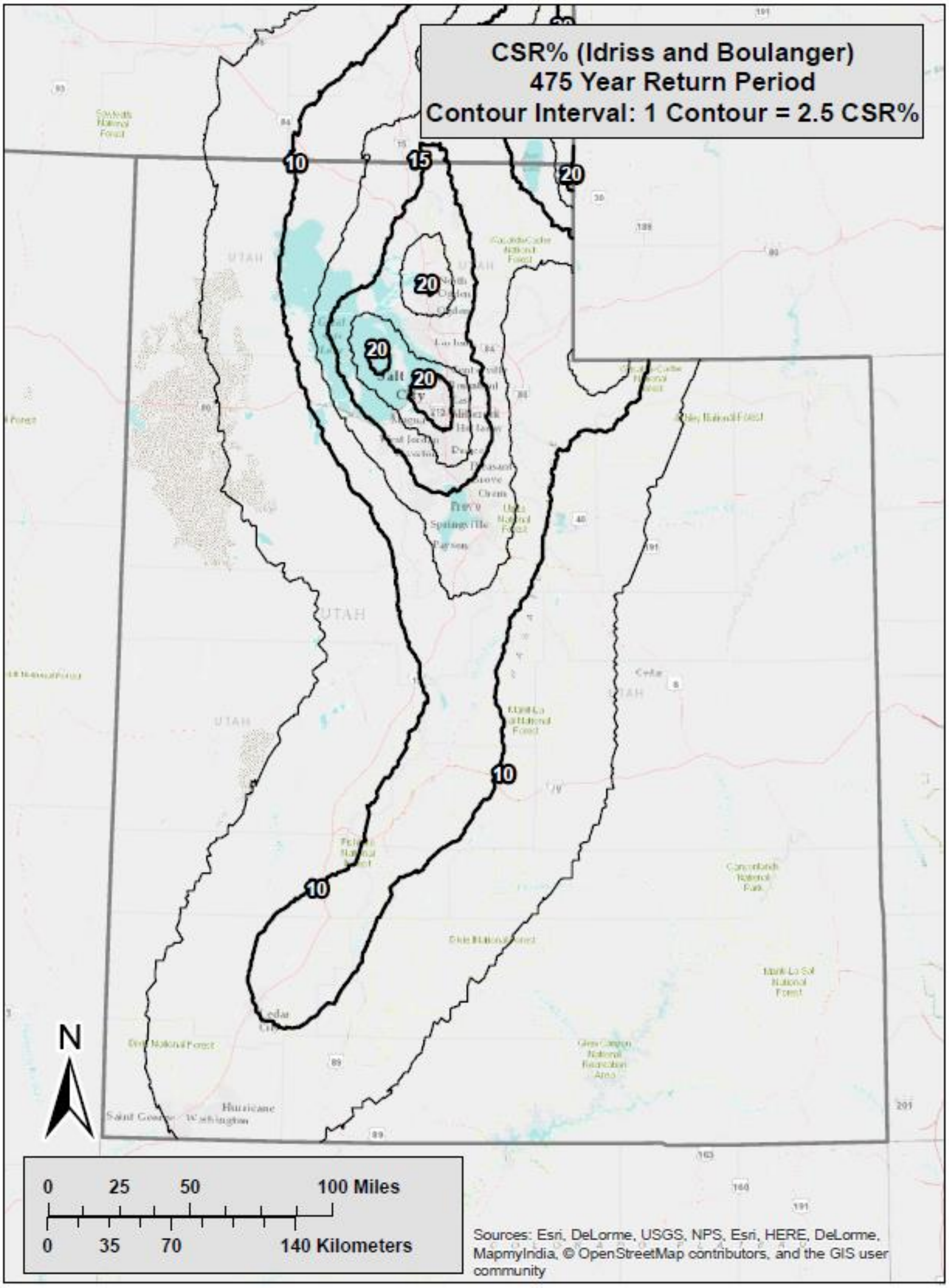

Sources: Esri, DeLorme, USGS, NPS, Esri, HERE, DeLorme, MapmyIndia, © OpenStreetMap contributors, and the GIS user community

Figure B-30 Liquefaction Triggering ($CSR\%^{ref}$) Map for Utah ($T_r = 475$)

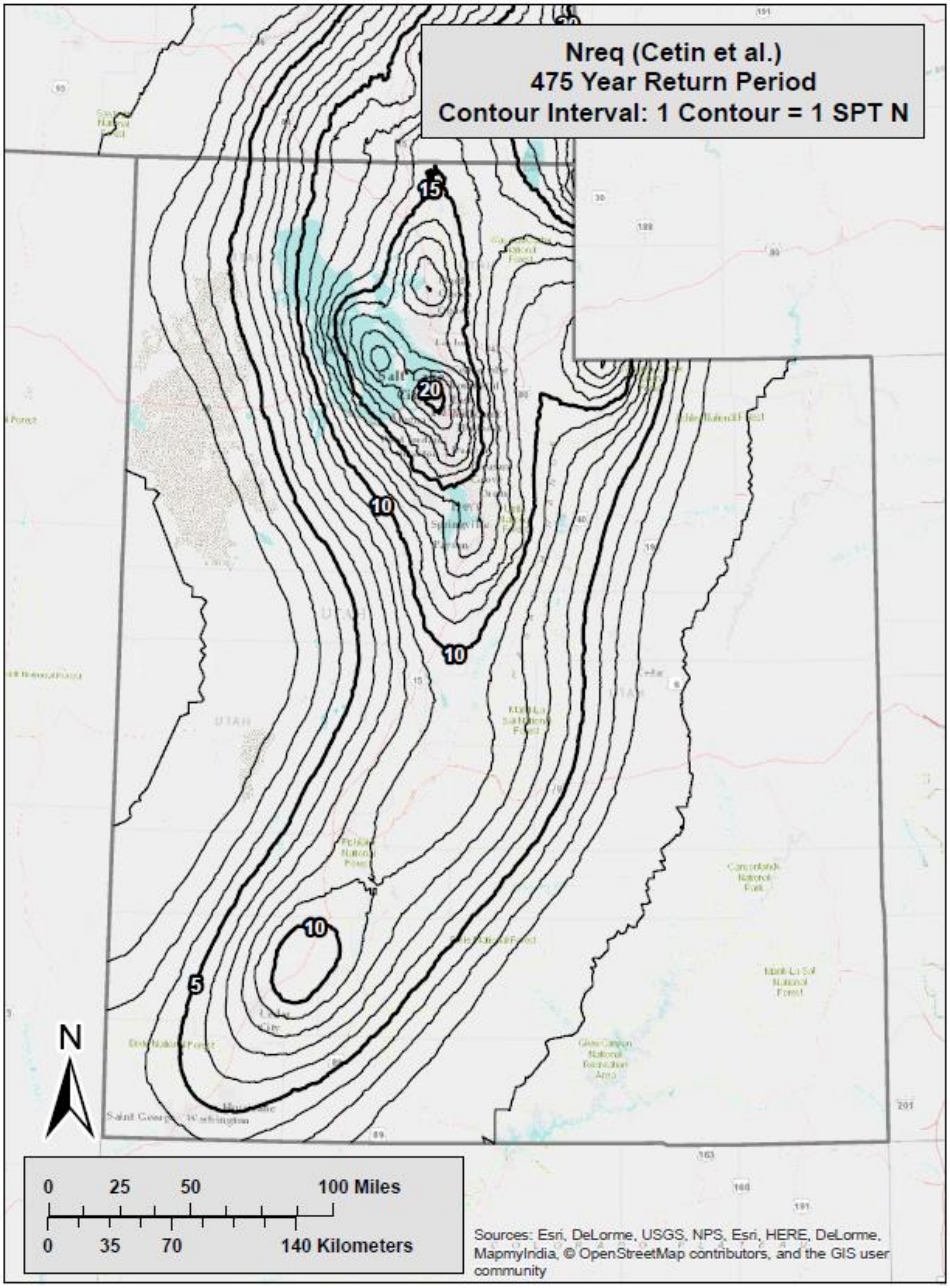

Sources: Esri, DeLorme, USGS, NPS, Esri, HERE, DeLorme, MapmyIndia, © OpenStreetMap contributors, and the GIS user community

Figure B-31 Liquefaction Triggering (N_{req}^{ref}) Map for Utah (T_r = 475)

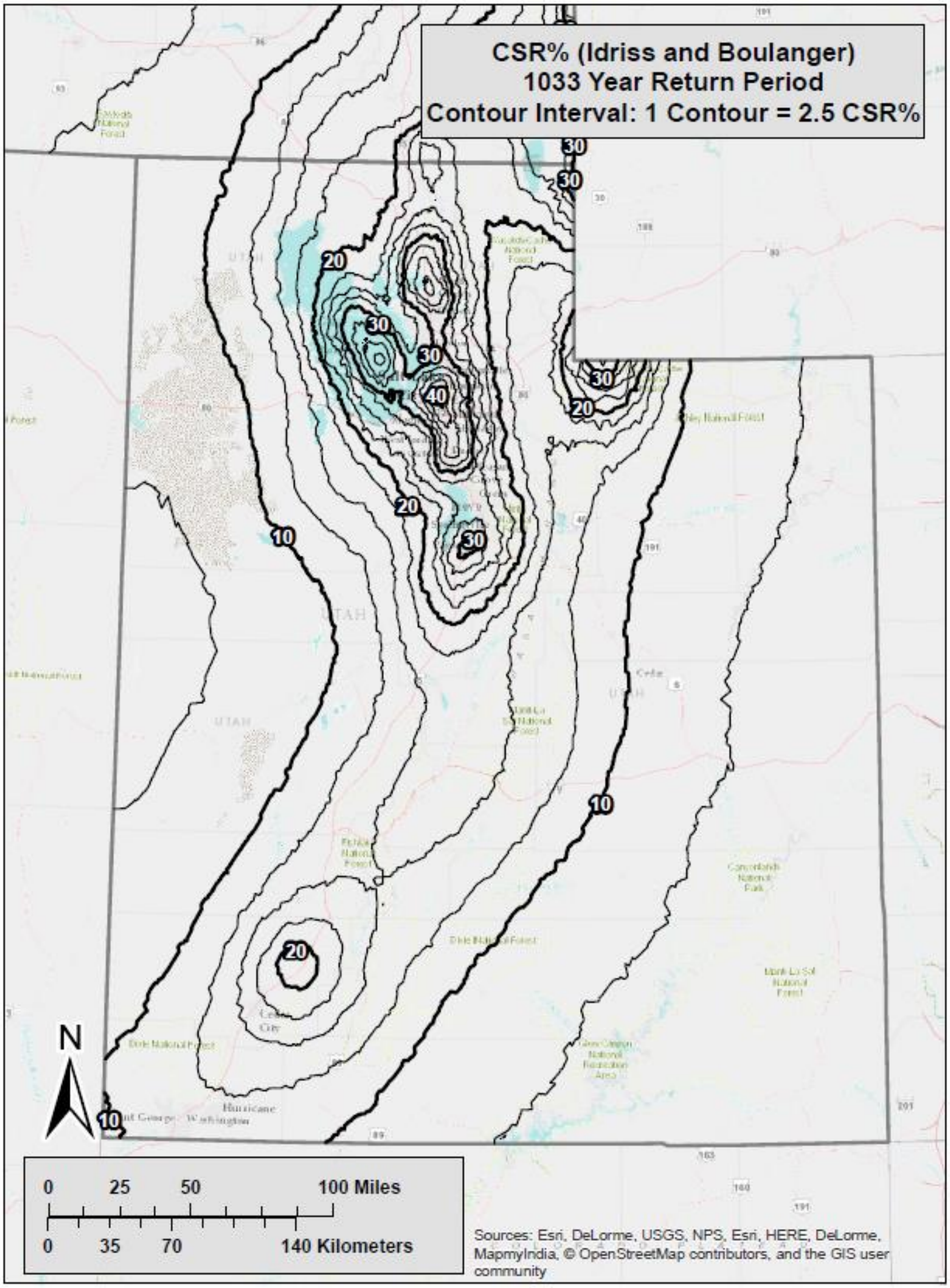

Figure B-32 Liquefaction Triggering ($CSR\%^{ref}$) Map for Utah (T_r = 1,033)

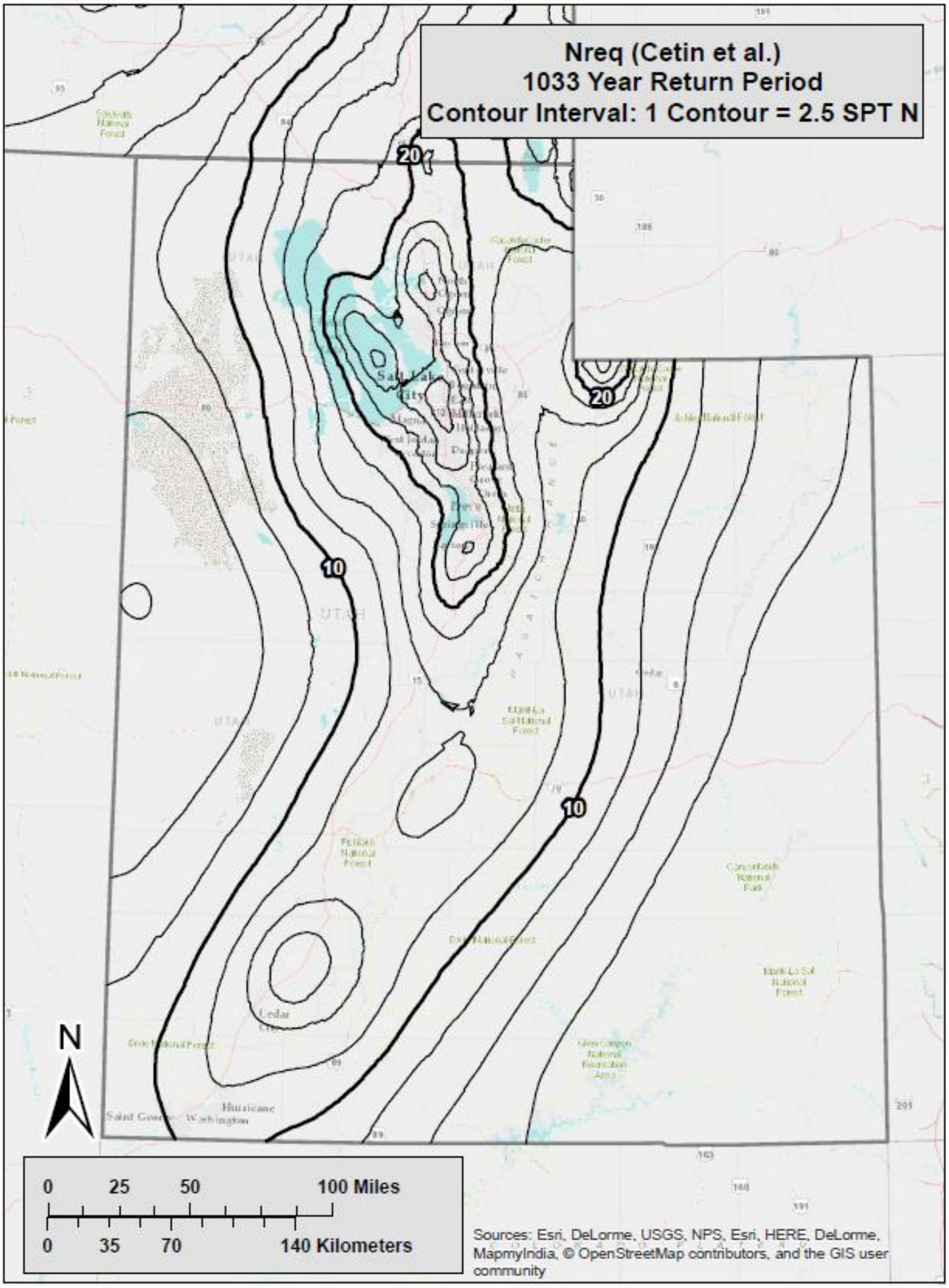

Figure B-33 Liquefaction Triggering (N_{req}^{ref}) Map for Utah (T_r = 1,033)

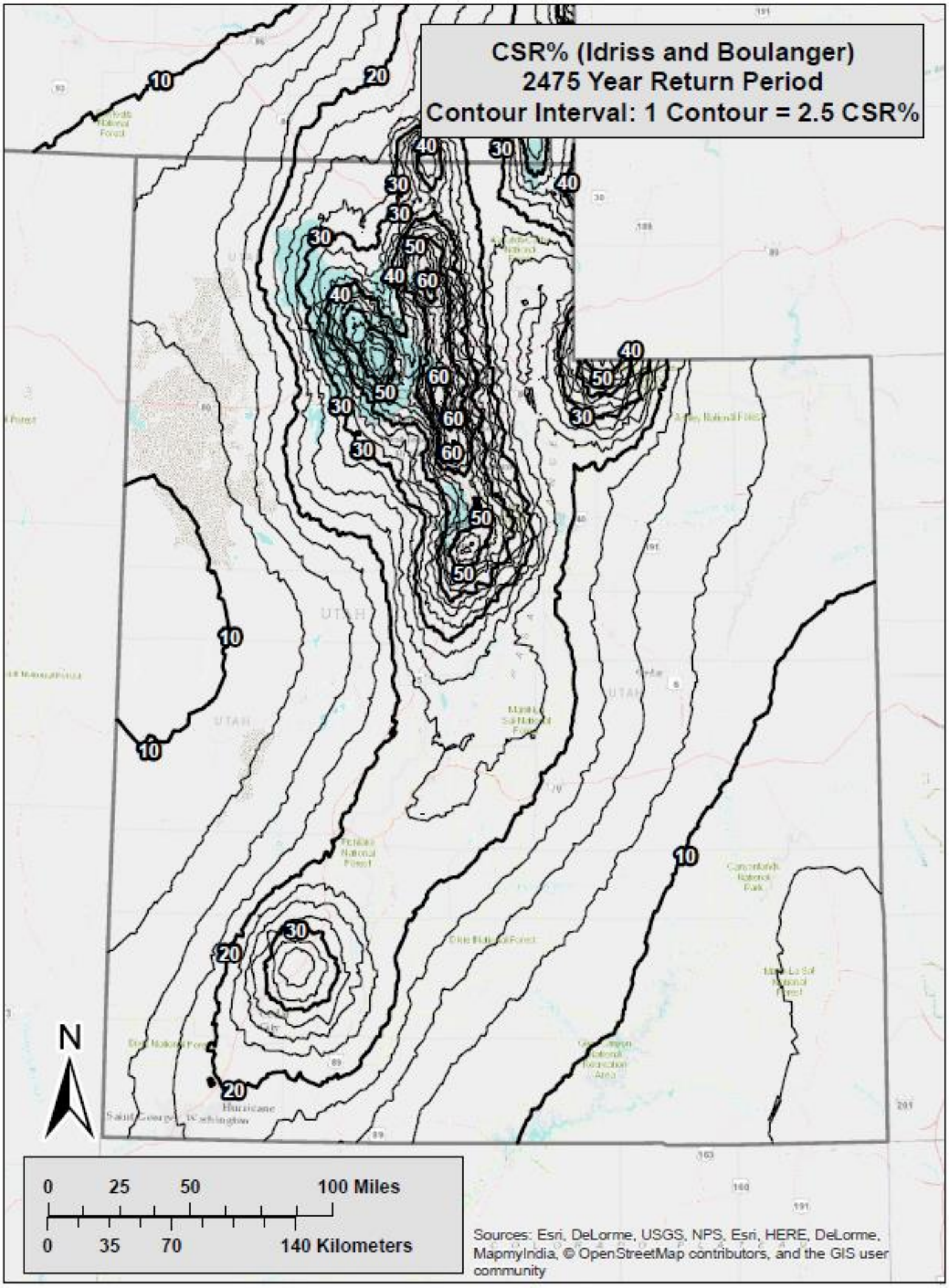

Sources: Esri, DeLorme, USGS, NPS, Esri, HERE, DeLorme, MapmyIndia, © OpenStreetMap contributors, and the GIS user community

Figure B-34 Liquefaction Triggering (*CSR%^{ref}*) Map for Utah (T_r = 2,475)

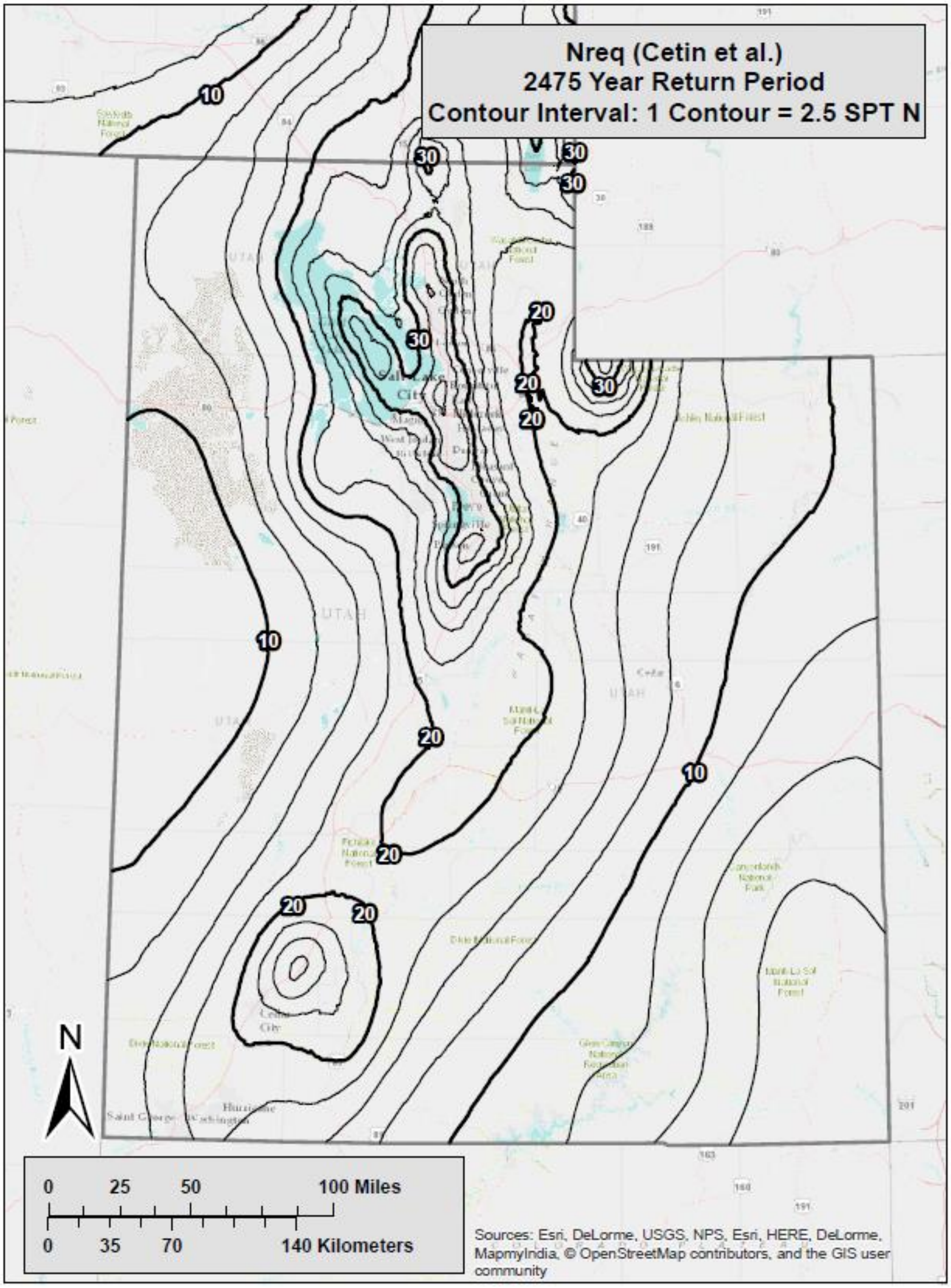

Figure B-35 Liquefaction Triggering (N_{req}^{ref}) Map for Utah (T_r = 2,475)

APPENDIX C: SUPPLEMENTARY DETERMINISTIC DATA

Table C-1: Faults Considered in Deterministic Analysis

					Median Acceleration			(Median + 1 St. Dev) Acceleration		
					T_R = 1033			T_R = 1033		
San Francisco		**Seismic Source**	**Dist (km)**	**Mag**	***PGA***	F_{pga}	a_{max}	***PGA***	F_{pga}	a_{max}
	1	Northern San Andreas	10.77	8.05	0.3175	1.183	0.3754	0.5426	1.0	0.5426
	2	San Gregorio Connected	16.64	7.5	0.2139	1.372	0.2935	0.3660	1.134	0.4150
	3	Hayward-Rodgers Creek	18.23	7.33	0.1918	1.416	0.2717	0.3282	1.172	0.3846
	4	Mount Diablo Thrust	36.08	6.7	0.1050	1.590	0.1670	0.1811	1.438	0.2604
	5	Calaveras	34.28	7.03	0.0981	1.6	0.1570	0.1682	1.464	0.2462
Salt Lake City										
	1	Wasatch Fault, SLC Section	1.02	7	0.5911	1.0	0.5911	1.0050	1.0	1.0050
	2	West Valley Fault Zone	2.19	6.48	0.5694	1.0	0.5694	0.9842	1.0	0.9842
	3	Morgan Fault	25.04	6.52	0.0989	1.6	0.1583	0.1713	1.457	0.2497
	4	Great Salt Lake Fault zone, Antelope Section	25.08	6.93	0.1016	1.597	0.1622	0.1742	1.452	0.2529
	5	Oquirrh-Southern, Oquirrh Mountain Fault	30.36	7.17	0.0958	1.6	0.1532	0.1641	1.472	0.2415
Butte										
	1	Rocker Fault	4.92	6.97	0.5390	1.0	0.5390	0.9202	1.0	0.9202
	2	Georgia Gulch Fault	45.91	6.42	0.0435	1.6	0.0696	0.0754	1.6	0.1206
	3	Helena Valley Fault	75.56	6.6	0.0294	1.6	0.0470	0.0507	1.6	0.0812
	4	Canyon Ferry Fault	81.32	6.92	0.0327	1.6	0.0523	0.0561	1.6	0.0898
	5	Blacktail Fault	84.27	6.94	0.0317	1.6	0.0508	0.0545	1.6	0.0872
	6	Madison Fault	86.51	7.45	0.0420	1.6	0.0671	0.0719	1.6	0.1150

Table C-2: Characteristics of Rocker Fault (near Butte) and Calculations to Determine *PGA* and M_w.

*M_w calculated based on Wells and Coppersmith (1994): Length = 43 km

(Use "all" slip type, because it's a normal fault and the # of normal events is small)

*PGA calculated based on NGA equations (Linda Al Atik, PEER 2009)

BA08, CB08, and CY08 used with equal weighting

M_w = 6.97

Dip = 70 degrees (Another fault near Butte, has a dip of 70-75 degrees)

Depth to bottom of rupture = 16 km (Assumed)

R_x = 4.92 km (measured using Google Earth)

Z_{TOR} = 0 km (Assumed)

Width = 17.03 km

R_{jb} = 0 km (Assuming the site is on the hanging wall side)

R_{rup} = 1.68 km

V_{s30} = 760 m/s

U= 0

F_{RV}= 0

F_{NM} = 1

F_{HW} = 1

$F_{measured}$ = 0

Z_1 = DEFAULT

$Z_{2.5}$= DEFAULT

F_{AS}= 0

HW Taper = 1

--> PGA (50%) = $\boxed{0.5390}$ g (From NGA spreadsheet)

--> PGA (84%) = $\boxed{0.9202}$ g (From NGA spreadsheet)